3D-PRINTED HEXAGONAL BORON NITRIDE
NANOSHEETS/POLYLACTIC ACID NANOCOMPOSITES

A THESIS SUBMITTED TO
THE GRADUATE SCHOOL OF NATURAL AND APPLIED SCIENCES
OF
MIDDLE EAST TECHNICAL UNIVERSITY

BY

MUSTAFA CANER GÖRÜR

IN PARTIAL FULFILLMENT OF THE REQUIREMENTS
FOR
THE DEGREE OF MASTER OF SCIENCE
IN
METALLURGICAL AND MATERIALS ENGINEERING

AUGUST 2022

Approval of the thesis:

**3D-PRINTED HEXAGONAL BORON NITRIDE
NANOSHEETS/POLYLACTIC ACID NANOCOMPOSITES**

submitted by **MUSTAFA CANER GÖRÜR** in partial fulfillment of the requirements for the degree of **Master of Science** in **Metallurgical and Materials Engineering, Middle East Technical University** by,

Prof. Dr. Halil Kalıpçılar
Dean, Graduate School of **Natural and Applied Sciences**

Prof. Dr. Ali Kalkanlı
Head of the Department, **Metallurgical and Materials Eng.**

Prof. Dr. Hüsnü Emrah Ünalan
Supervisor, **Metallurgical and Materials Eng., METU**

Assoc. Prof. Dr. Simge Çınar Aygün
Co-Supervisor, **Metallurgical and Materials Eng., METU**

Examining Committee Members:

Prof. Dr. Cevdet Kaynak
Metallurgical and Materials Eng., METU

Prof. Dr. Hüsnü Emrah Ünalan
Metallurgical and Materials Eng., METU

Assoc. Prof. Dr. Simge Çınar Aygün
Metallurgical and Materials Eng., METU

Assist. Prof. Dr. Yusuf Keleştemur
Metallurgical and Materials Eng., METU

Assist. Prof. Dr. Şahin Coşkun
Metallurgical and Materials Eng, Eskişehir Osmangazi
University

Date: 26.08.2022

I hereby declare that all information in this document has been obtained and presented in accordance with academic rules and ethical conduct. I also declare that, as required by these rules and conduct, I have fully cited and referenced all material and results that are not original to this work.

Name Last name : Mustafa Caner Görür

Signature :

ABSTRACT

3D-PRINTED HEXAGONAL BORON NITRIDE
NANOSHEETS/POLYLACTIC ACID NANOCOMPOSITES

Görür, Mustafa Caner
Master of Science, Metallurgical and Materials Engineering
Supervisor: Prof. Dr. Hüsnü Emrah Ünalan
Co-Supervisor: Assoc. Prof. Dr. Simge Çınar Aygün

August 2022, 89 pages

The use of electronic devices in all sectors is inevitable and any improvement in energy savings has great effects on a global basis. The thermal management of these devices is the most important factor in energy savings because as these devices get smaller, the amount of heat they emit increases, and this excess heat considerably shortens their lifespan. Therefore, current research has focused on the release of heat to the environment rather than trapping it in devices.

Hexagonal boron nitride (h-BN) nanosheets, on which many studies have been carried out in recent years, draw attention with their electrical resistivity and high thermal conductivity. h-BN is known as "white graphene" because of the similarity of its lattice structure and thermal properties with graphene. However, unlike graphene, h-BN nanosheets are electrically resistive that makes them promising candidates for the thermal management of electronic devices. In addition, reducing the number of layers of h-BN expands the surface area and prevents phonon scattering during heat conduction, thereby significantly increasing the thermal conductivity value.

Additive manufacturing (AM) is a fast and economically feasible prototype production method that allows fabrication of complex structures. In addition, AM

considers many parameters such as infill percentage of material use, the angle of printing, printing speed and pattern, and height of each layer that are used to optimize the production.

In this thesis, h-BN nanosheets are used as filler materials for the production of nanocomposites with polylactic acid (PLA) matrix. For this purpose, h-BN nanosheet/PLA nanocomposite filaments suitable for 3D printing were prepared, which were then used to 3D print heat dissipating devices for the thermal management of electronic devices. In this regard, h-BN was exfoliated with both ball-milling and shear exfoliation methods. Few-layered h-BN nanosheets stable in water for more than one month were obtained in both methods. Shear exfoliation was chosen as the main production method since it allowed production of large amounts of few layered (<10 layers) of h-BN nanosheets. Afterwards, h-BN/PLA filaments were used to print a heat sink and LED bulb holder for thermal management applications. In the first application, heat sinks were heated from their lower surfaces. The temperature of the upper surface of the 3D printed h-BN/PLA heat sink was found 6.3 °C higher than 3D printed bare PLA and just 1.4 °C lower than that of the commercial aluminum (Al) heat sink. The heat dissipation rate of PLA was found to increase by 320% by adding 40 vol. % h-BN. In the second application, printed LED bulb holders were assembled into a LED bulb and LED temperatures were monitored. The lowest temperature detected on the LED chips was 120.8 °C for the 3D printed h-BN/PLA sample. The temperature of the commercial LED bulb was detected as 122.1 °C and 3D printed bare PLA sample showed the highest temperature of 136.4 °C. This experiment proved that h-BN/PLA nanocomposites can be used to extend the lifetime of LED bulbs.

Keywords: 3D printing, hexagonal boron nitride nanosheets, exfoliation, PLA matrix nanocomposites, thermal management devices

ÖZ

3B BASKILI HEKZAGONAL BOR NİTRÜRÜ NANOLEVHALARI/POLİLAKTİK ASİT NANOKOMPOZİTLERİ

Görür, Mustafa Caner
Yüksek Lisans, Metalurji ve Malzeme Mühendisliği
Tez Yöneticisi: Prof. Dr. Hüsnü Emrah Ünalan
Ortak Tez Yöneticisi: Doç Dr. Simge Çınar Aygün

Elektronik cihazların tüm sektörlerde kullanılması kaçınılmazdır. Enerji tasarrufunda yapılacak herhangi bir iyileştirmenin küresel bazda büyük etkileri vardır. bu cihazlar küçüldükçe yaydıkları ısı miktarı artar ve bu fazla ısı kullanım ömürlerini önemli ölçüde kısalttığı için, bu cihazların ısı yönetimi enerji tasarrufunda en önemli faktördür. Bu nedenle, mevcut araştırmalar cihazlarda hapsolan ısının çevreye salınmasına odaklanmıştır.

Son yıllarda üzerinde birçok çalışma yapılan 2D hekzagonal bor nitrürü (h-BN) nanolevhaları, elektriksel direnci ve yüksek ısıl iletkenliği ile dikkat çekmektedir. Kafes yapısının ve termal özelliklerinin grafen ile benzerliği nedeniyle "beyaz grafen" olarak da bilinmektedir. Bununla birlikte, grafenden farklı olarak h-BN nanolevhaları, elektronik cihazların termal yönetiminin güvenliği için umut verici bir aday olmasını sağlayan bir elektriksel direnç özelliğine sahiptir. Ek olarak, h-BN katmanlarının sayısının azaltılması, yüzey alanını genişletir ve ısı iletimi sırasında fonon saçılımını önler, böylece termal iletkenlik değerini önemli ölçüde artırır.

Katmanlı imalat, karmaşık yapıların üretimine olanak sağlayan hızlı ve ekonomik olarak uygulanabilir bir prototip üretim yöntemidir. Ayrıca katmanlı imalat, malzeme kullanımının doluluk yüzdesi, baskı açısı, baskı hızı, deseni ve katman

yüksekliği gibi üretimin optimizasyonu için kullanılan birçok parametreyi hesaba katmaktadır.

Bu tezde, nanokompozit üretimi için, polilaktik asit (PLA) matriksinin içinde katkı malzemesi olarak h-BN nanolevhaları kullanılmıştır. Bu amaçla, 3B baskıya uygun h-BN nanolevhaları/PLA nanokompozit filamentler hazırlanmış ve daha sonra elektronik cihazların termal yönetimi için ısı dağıtan cihazların 3B baskısında kullanılmıştır. Bu bağlamda, hem bilyalı öğütme hem de kesme eksfoliasyonu yöntemleriyle h-BN eksfoliye edilmiştir. Her iki yöntemde de suda bir aydan fazla stabil olan birkaç katmanlı h-BN nanolevhalar elde edildi. Elde edilen h-BN'in miktarının daha fazla ve birkaç katmanlı olması (<10 katman) nedeniyle ana üretim yöntemi olarak kesme eksfoliasyonu seçilmiştir. Daha sonra ise, h-BN/PLA filamenti üretilmiş ve termal yönetim uygulamaları için ısı soğurucu ve LED ampul tutucu cihazları basılmıştır. İlk uygulamada, ısı soğurucular alt yüzeylerinden ısıtıldı. 3B baskılı h-BN/PLA ısı soğurucunun üst yüzeyinin sıcaklığı, 3B baskılı PLA'dan 6.3 °C daha yüksek ve ticari alüminyum (Al) ısı soğurucudan sadece 1.4 °C daha düşüktür. PLA'nın ısı yayma oranı, hacimce %40 h-BN eklemesi ile %320 artırılmıştır. İkinci uygulamada ise, 3B baskılı LED ampul tutucular, LED ampuller ile montajlanmış ve LED çiplerinin sıcaklıkları görüntülenmiştir. LED çiplerinde tespit edilen en düşük sıcaklık, 120.8 °C ile 3B baskılı h-BN/PLA örneğinde görülmüştür. Ticari LED ampulde sıcaklık 122.1 °C olarak görüldü ve 3B baskılı PLA örneği en yüksek sıcaklığı 136.4 °C gösterdi. Bu deney, h-BN/PLA nanokompozitlerinin LED ampulün ömrünü uzatabileceğini kanıtladı.

Anahtar Kelimeler: 3B baskı, hekzagonal bor nitrürü nanolevhaları, eksfoliasyon, PLA matriks nanokompozitler, termal yönetim cihazları

In memory of my grandfather Mustafa Nail Karacaer

ACKNOWLEDGMENTS

TABLE OF CONTENTS

LIST OF TABLES

LIST OF FIGURES

FIGURES

CHAPTER 1

INTRODUCTION

1.1 3D Printing

1.1.1 Introduction to 3D Printing

3D printing, (i.e. additive manufacturing (AM)) is a method of combining materials to produce objects layer by layer. It is first mentioned by Charles Hull in 1986[1,2]. The fundamental behind AM is based on the building up of layers that are stacked and formed in a two-dimensional (x-y) plane in a precise manner. The third dimension (z) is created by stacking single layers on top of each other[3]. However, the model has to be accumulated with very fine layers to produce a unique structure in all planes. It is one of the most important differences between the AM techniques and will be discussed later. AM technology is composed of five steps, which are also schematically summarized in Figure 1.1[3]. First, 3D computer models of the designs are drawn with computer-aided design (CAD) software (Autodesk Inventor, SolidWorks, Siemens NX, etc.). These designs are meshed to create a surface tessellation language (STL) format by slicing and they become 2D layers as a second step. In the third step, printing speed, the material used for this printing, layer height, and supporting conditions for better adhesion between the object and print bed, are arranged. The file is exported as a geometric code (gcode), language for computer numerical control (CNC) systems, to the 3D printing devices by slicing software (Prusa Slicer, Slic3r, Cura, etc.). These parameters' effects will be discussed later. The prototype is built with the layer-by-layer mechanism with the arranged parameters by a 3D printing device as a fourth step. The fifth and final step involves the post process, which could be removing the support parts, cleaning the surface, or post-curing[4–6].
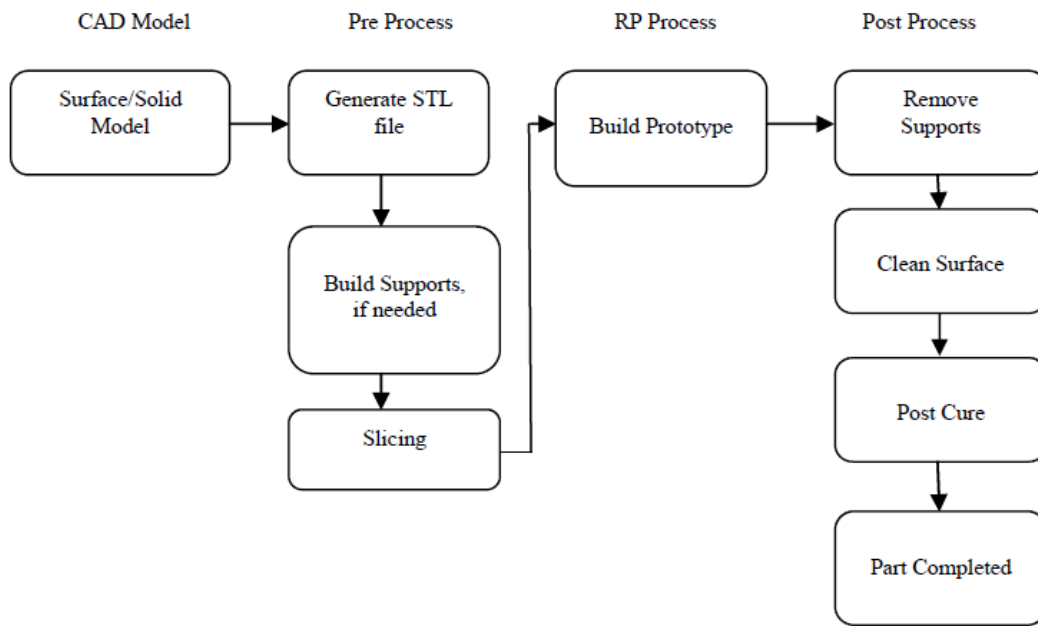
Figure 1.1. Schematic view of 3D printing steps from design to object[3].

AM has several advantages and drawbacks. The first advantage is the ability to produce objects with complex geometry. These objects cannot be produced with common manufacturing methods without further configuration or post-process[7]. In addition to this, small-sized objects can also be produced with AM methods owing to their high-resolution settings. Another profit is reducing the prototype production cost and time. Finally, since AM is based on layer by layer material addition, waste and scrap are reduced[8,9]. In contrast, subtractive manufacturing methods such as machining and drilling produce substantial waste and scrap.

Although there are a great number of advantages, some drawbacks also exist for the AM techniques. The material limitation is one of the biggest disadvantages that limit the application areas. All AM techniques have their own specific requirements like thickness limitation for the filaments or UV curability for resins. Objects produced with conventional methods are offering much wider application areas. This is because it allows the use of a wide variety of materials. Moreover, AM techniques are not feasible for mass production. Instead, AM methods are suitable for prototype production. Prototypes can be produced rapidly in a cost-effective manner compared

to commercial production methods like injection molding. In addition, the poor surface quality causes both the stress concentration problem under cyclic loads and discontinuity for the heat transfer pathways[10]. Surface quality can be tuned by layer thickness, printing temperature and speed, calibration of the device, material used, and many other properties for different AM methods.

1.1.2   3D Printing Methods

Each AM method has its own benefits and limitations in terms of material types and forms, calibration, resolution, working principle (extrusion, UV-assisted curing, laser scanning, etc.), and many other properties. These differences between the three AM methods will be discussed in the following part.

1.1.2.1   Fused Deposition Modelling (FDM)

FDM is one of the most common methods in AM techniques. This is because the device is simple and affordable. The devices of this technique use thermoplastic wire filaments that are melted to a semi-melted state by a print head and extruded with a thickness between 100-300 micrometers[11]. The material is deposited on top of the preexisting layer as the extrusion nozzle moves along a pattern determined by the component cross-sectional boundary. When a layer is complete, the print head lifts up to the layer thickness height and the nozzle keeps filling the model until the entire three-dimensional (3D) item is obtained[12]. Nylon (PA6), polyethylene (PE), polypropylene (PP), thermoplastic polyurethane (TPU), and especially PLA and acrylonitrile butadiene styrene (ABS) are the most commonly used filament materials for FDM[8]. Some FDM devices are composed of double extrusion heads. The second head is generally used for the support parts. Some objects need to be printed with support parts to protect their structure during printing. The removal of these parts without damaging the main object is a serious problem. Water-soluble materials are used as support materials to solve this problem. The printed object is

left in water after printing to completely remove the support material. Figure 1.2 shows the FDM process with a second extrusion head printing supporting layers[13].
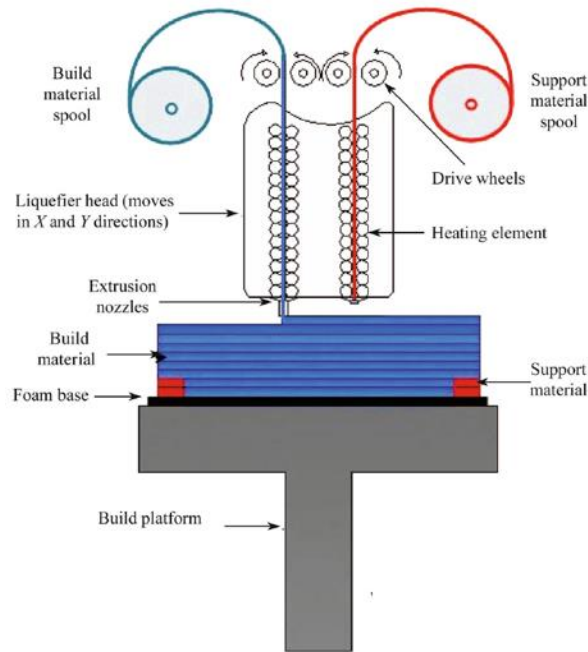
Figure 1.2. Schematic illustration of the FDM principles[13].

Process parameters of FDM method strongly affect the properties of the printed objects like surface quality, roughness, dimensional accuracy, elastic performance, porosity, yield strength, etc. Slicer software has a lot of printing parameters to optimize these properties. Printing speed, nozzle and bed temperature, layer height, first layer settings, and fan speed are examples of these parameters in light of optimizing the 3D printed object quality with FDM.

FDM method offers a number of benefits, including materials budget, and energy consumption[14]. Moreover, it is portable and open source so that hardware or software problems of the devices can be easily solved. Materials that are used for FDM are recyclable because thermoplastic polymers are the main material types of this technique[15]. Despite these advantages, the FDM method has several limitations such as the poor surface quality and poor strength of printed objects. Layer adhesion problem also requires extra treatments like sticking the surface with glue. In addition

to these, nozzle clogging and bed calibration are frequently needed [16]. The limitation of suitable printing material is the most important obstacle in front of the increase of academic research in different application areas.. For example, electrically resistive and thermally conductive filaments are needed for electronic packaging applications but there is no such filament in the market for this use[15].

1.1.2.2   Stereolithography (SLA)

Stereolithography (SLA) also known as vat polymerization, is one of the main techniques for additive manufacturing of polymers. A solid polymer is created by scanning and curing the liquid monomer's surface with an ultraviolet (UV) laser beam. Therefore photocurable polymers can be used for this method[17]. The curing process of the polymer in the tank occurs according to the CAD drawing. The uncured parts are left in liquid form. The build platform moves lower to cure the following layer to extend the printing process on the z-axis. Once printing is complete, post-processes like UV curing, annealing, vacuum drying, or washing is required for this method. Optimization of printed parts' properties such as durability and strength is made using the parameters like layer thickness, laser exposure time, and the position of the object in the building platform.[18]. For example, Kimura et al. claimed that stiffness of the printed part is strongly related to the post-exposure time and that two hours of exposure is necessary to achieve stability[19]. Post-process is necessary to improve the surface quality and thermo-mechanical properties of objects[20,21]. A schematic representation of the SLA 3D printing method is provided in Figure 1.3[22].
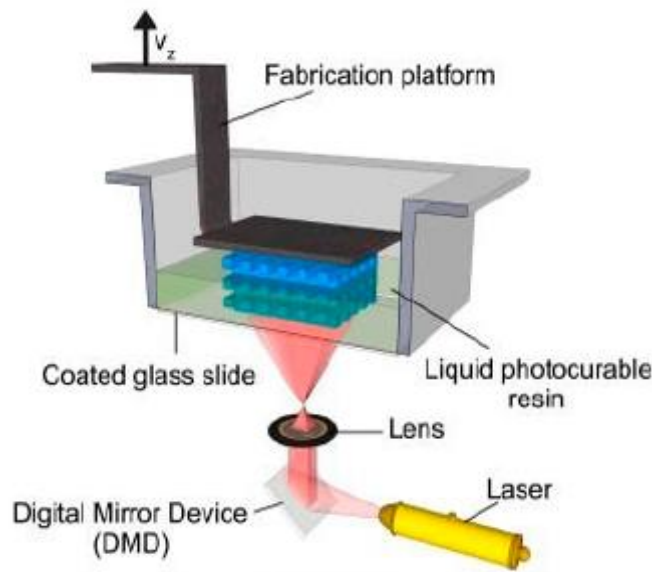
Figure 1.3. Schematic illustration of the SLA principle[22].

The resolution (30-140 micrometers) and dimensional accuracy are the most important advantages of SLA 3D printing therefore, highly durable products can be made with this method[23]. The anisotropic property of 3D printed objects is also a common problem for other AM techniques and this limits the application areas. However, SLA produces highly isotropic parts due to its high control of the material chemistry. There is no difference between the X, Y, or Z planes on the molecular level. The resin forms covalent bonds during layer printing. In addition to this, the energy consumption of this method is also low similar to the FDM method[16,24]. SLA method also have some disadvantages like the other AM techniques. It requires support material to protect the shape integrity like FDM. The removal of these parts is a serious problem[25]. In addition, printing materials are limited because they need to be photocurable for printing with SLA. Also large volume printing cannot be practiced with this method due to its small print bed[26,27].

1.1.2.3   Powder Bed Fusion (PBF)

In this method, the powder material particles are poured over the previous layer which is fused, irradiated, or melted powder by heat energy. This energy comes

mostly from a laser or an electron beam. Different kinds of lasers are frequently used as the heat sources in PBF. The roller and blade are used to add new powder onto the previous layer. The supply of raw material is provided by a hopper or reservoir just next to the bed[28]. Powder size, deposition speed with the roller or blade, and laser speed can be counted as important parameters that determine the quality of the printed part[29,30]. PBF method is schematically illustrated in Figure 1.4 [1].
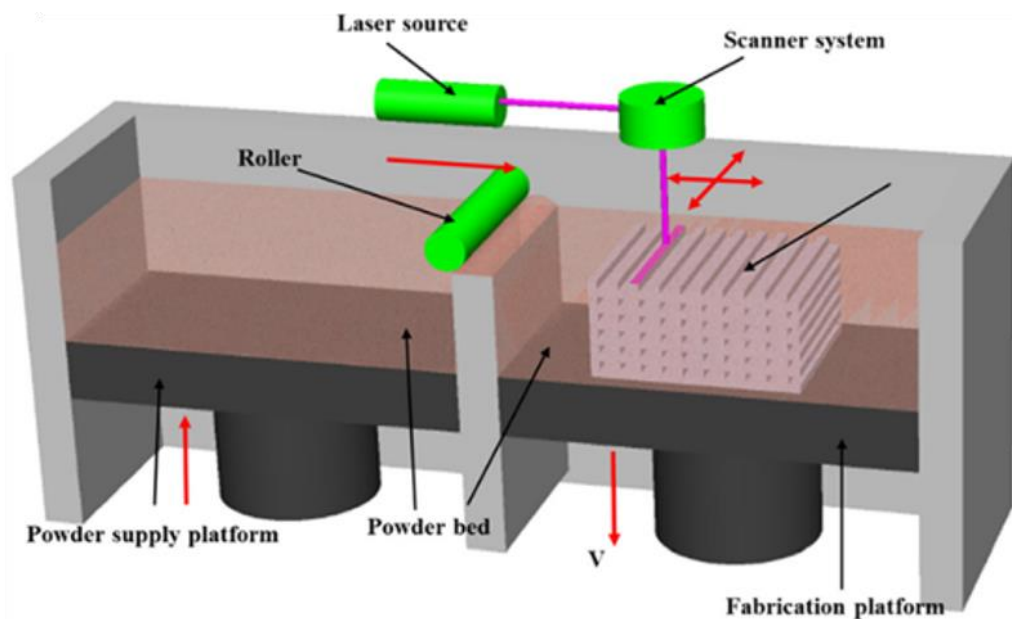
Figure 1.4. Schematic illustration of PBF principle[1].

There are five types of PBF methods. Electron beam melting (EBM) is one of these types that can be used for metals and alloys. But it requires a vacuum environment. Another type is selective laser sintering (SLS), which is used for the fusing of polymers by laser. Direct metal laser sintering (DMLS) also uses the same method but it is for metallic materials. The working principles of selective laser melting (SLM) is similar to the SLS method; but it melts the metals instead of sintering them. Parts that are produced with SLM have a finer microstructure and the process is faster than SLS. The final type is selective heat sintering (SHS), which has a different sintering method than the others. In this method, a heated thermal print head is used to fuse the powders[31,32].

PBF methods have also advantages and disadvantages like all other AM techniques. First of all, the resolution of this technique is between 80-150 micrometers. It can also be used for small-scale laboratory size machines as FDM devices. In addition to these advantages, a wider variety of material types can be used in this method compared to the others. However, it takes longer to complete a print with this technique. Size limitation is also a drawback similar to FDM and SLA. One of the major disadvantages is that the excessive amount of energy is consumed during operation[28].

1.2   3D Printed PLA Based Nanocomposites

1.2.1   Polylactic Acid (PLA)

1.2.1.1   Production of PLA

In 1845, Theophile-Jules Pelouze was the first to produce poly(lactic acid) (PLA) by polycondensing lactic acid[33]. Nowadays, microbial carbohydrate fermentation is used in industrial lactic acid production. It is more cost-effective than chemical methods since it uses less number of ingredients. It allows for the fabrication of optically pure lactic acid. It is crucial for high-quality PLA production[34]. The lactide can be made into three stereoisomers (L, D, and meso-lactide) since each molecule has two chiral carbon atoms as can be seen in Figure 1.5.
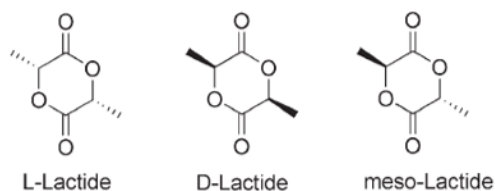
Figure 1.5 Stereoisomers of lactide[35].

Direct polymerization of lactic acid, ring-opening polymerization of lactide, and polycondensation can now be used to produce PLA polymers. Direct polymerization

8

is the first technique described as "A" in Figure 1.6 and produces a low molecular weight PLA polymer[36]. This is owing to the difficulty of removing contaminants from the fermentation liquor for direct PLA synthesis. It results in a brittle polymer[37,38]. The second method for PLA production is ring-opening polymerization (ROP) described as "B" in Figure 1.6. It is the most common technique in industrial production methods and is composed of two steps. In the first step, a low molecular weight oligomer is produced by polymerization of lactic acid and the lactide ring then opens, forming PLA with a high molecular weight as a second step. Heavy metals like tin are used for the ROP technique as catalysts[36]. Third and the last production method is polycondensation. It is described as "C" in Figure 1.6. In this method, tens of thousands of prepolymers with average molecular weights are produced. Side reactions and products can be seen for this method due to the carboxyl and hydroxyl groups and these reactions have an inevitable negative effect on the final product. As a result, when all of these factors are taken into account, low molecular weight PLA is formed with this method[39].
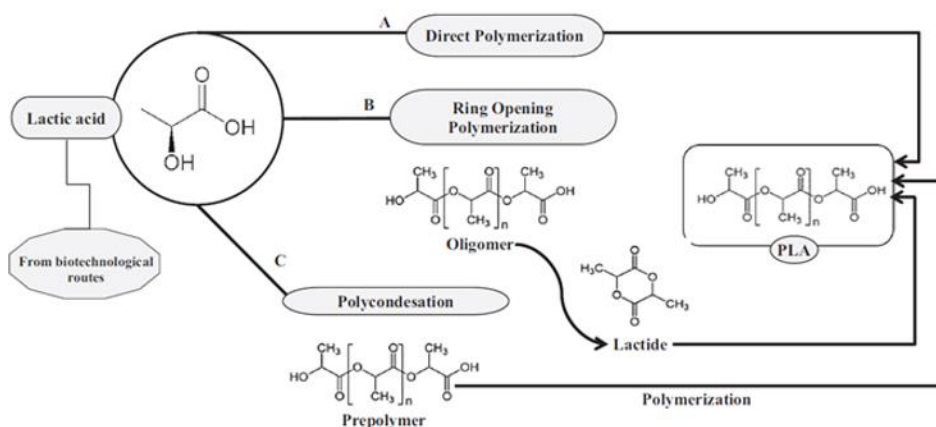
Figure 1.6. Schematic representation of PLA production methods[36].

1.2.1.2 Properties of PLA

1.2.1.2.1 Physical and Mechanical Properties of PLA

Like all other polymers, the degree of crystallinity and molar mass determine the mechanical properties of PLA[40]. Among other thermoplastic polymers, PLA has a strong potential for composites with its promising mechanical properties, such as flexural strength of up to 140 MPa. Other important mechanical properties like tensile strength and modulus are 53 MPa and 3.5 GPa, respectively[41,42]. In addition, the ability of processing is crucial for the matrix materials in composites and PLA is a promising candidate because of its low shrinkage.

Water absorption refers to a polymer's ability to absorb moisture from its surroundings. Absorbed moisture can function as a plasticizer, lowering the glass transition temperature and degrading the mechanical properties[43]. Lay et al. made a comparison test for the most common polymers for both FDM 3D printing and injection molding (IM) [44]. The comparison is made between the PLA, ABS, and PA6 as can be seen in Figure 1.7. All samples produced using the FDM process absorbed more water than those produced using injection molding. This was attributed to void formation between the printed layers. Nylon has the highest absorption percent because of its hygroscopic behavior which leads to volumetric swelling. PLA showed the best result according to this work. It protects its structure in long-term use in moist areas.
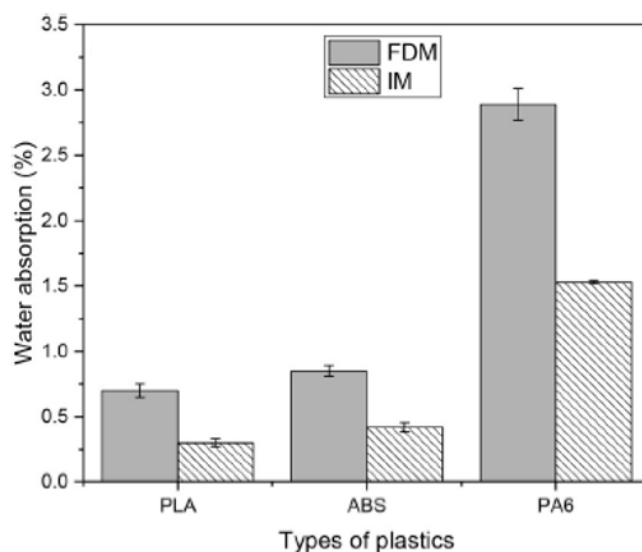
Figure 1.7. Change in water absorption for PLA, ABS, and PA6 polymers produced with FDM and IM method[44].

1.2.1.2.2 Thermal Properties of PLA

Semicrystalline PLA, like many thermoplastic polymers, has a glass transition temperature (T_g) around 60 °C and a melting temperature (T_m) around 175 °C. PLA has a soft and rubbery structure at temperatures higher than its T_g value. Moreover, it becomes a brittle polymer at nearly -45 °C, which is its β transition temperature (T_β)[45]. T_g is the transition temperature at which polymer chains begin to slide against one another. It depends on the purity and the molecular weight. For instance, T_g increases with the molecular weight. T_β is related to the local motions of the polymer chain backbone, which do not necessitate cooperative motion of neighboring chains[46]. Polymers need to protect their shape stability at room temperature and their melting temperatures need to be within a manageable range for easy reshaping. PLA has relatively reasonable thermal properties among other polymers with respect to T_g and T_m as can be seen in Figure 1.8.
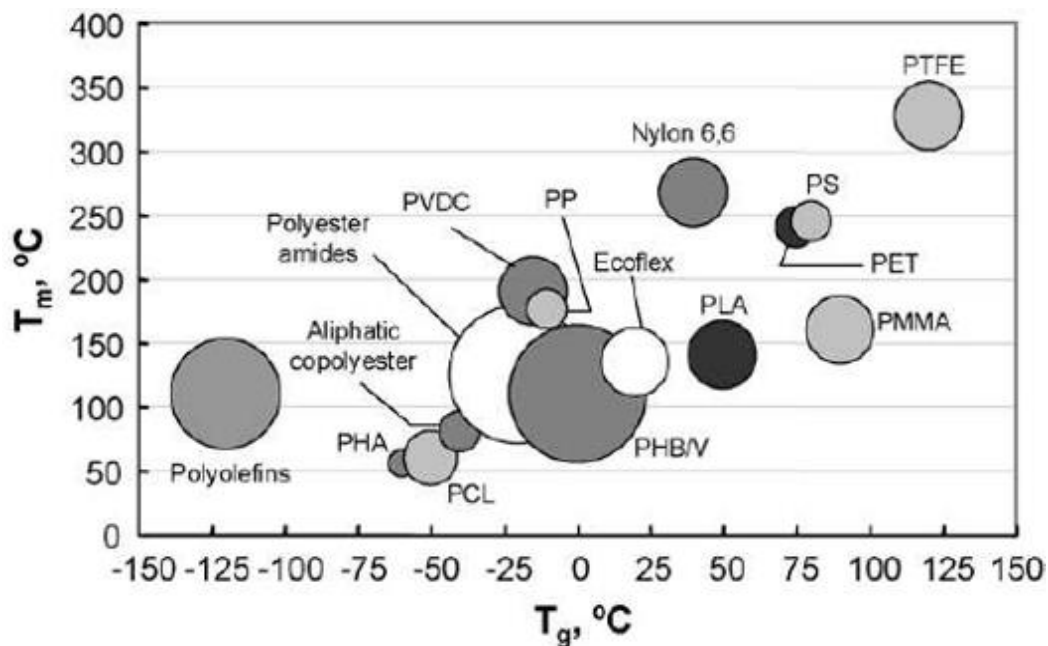
Figure 1.8. T_g and T_m values of different kinds of polymers [45].

Despite the fact that PLA has suitable thermal properties for both composite production and 3D printing, it has an ultralow thermal conductivity value between 0.16-0.20 W/m.K as reported in the literature[47,48,49]. The thermal conductivities of six polymers, which are polypropylene (PP), polyimide (PI) polystyrene (PS), PLA, polycarbonate (PC), and PA6 are shown in Figure 1.9 [50]. PLA is located almost in the middle but this value is still low. It needs to be increased to expand the application areas of this polymer.
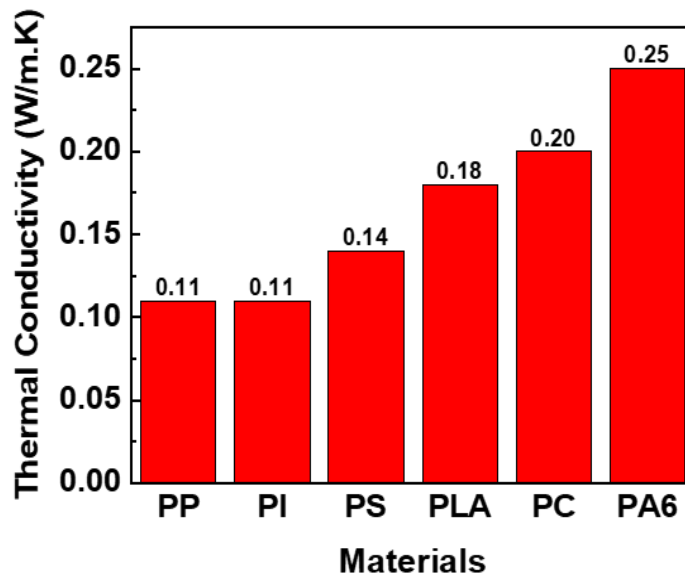
Figure 1.9. Thermal conductivity values of different kinds of polymers[47,50].

1.2.2   3D Printed PLA Based Nanocomposites

1.2.2.1   PLA/Graphene Nanocomposite

PLA is an electrically insulating and mechanically weak polymer. This situation limits its applications in 3D printing. Graphene is one of the most widely used filler material for nanocomposites due to its excellent conductivity and mechanical strength. It has a high elastic modulus of 1 TPa and excellent tensile strength of 130 GPa due to densely linked carbon atoms[51]. Kim et al. made a comparison of electrical and mechanical properties of FDM 3D printed graphene nanoplatelets (GNP) filled PLA matrix nanocomposite. Tensile strength and maximum strain at fracture are found to increase by 44% and 57%, respectively, by the addition of 2 wt.% GNP as can be seen in Figure 1.10 (a). However, these values are at a decreasing trend after addition of 2 wt.%. Elastic modulus also starts to decrease after a GNP amount of 4 wt.%. It can be related to the increment of the connection points between GNPs leading to crack propagation. Since the nanofiller-polymer interactions are stronger than nanofiller- nanofiller interactions. Another property increased by GNP addition

13

is the electrical conductivity. According to Figure 1.10 (b), there is no change in the conductivity value until a GNP concentration of 1.2 wt. % GNP. Resistivity is dramatically decreased from MΩ.cm level to below 100 kΩ.cm after the addition of 2.5 wt. % GNP. The results show that the percolation threshold is revealed after these amounts of GNP addition. This threshold corresponds to the minimum filler amount required to create the conduction paths [52].
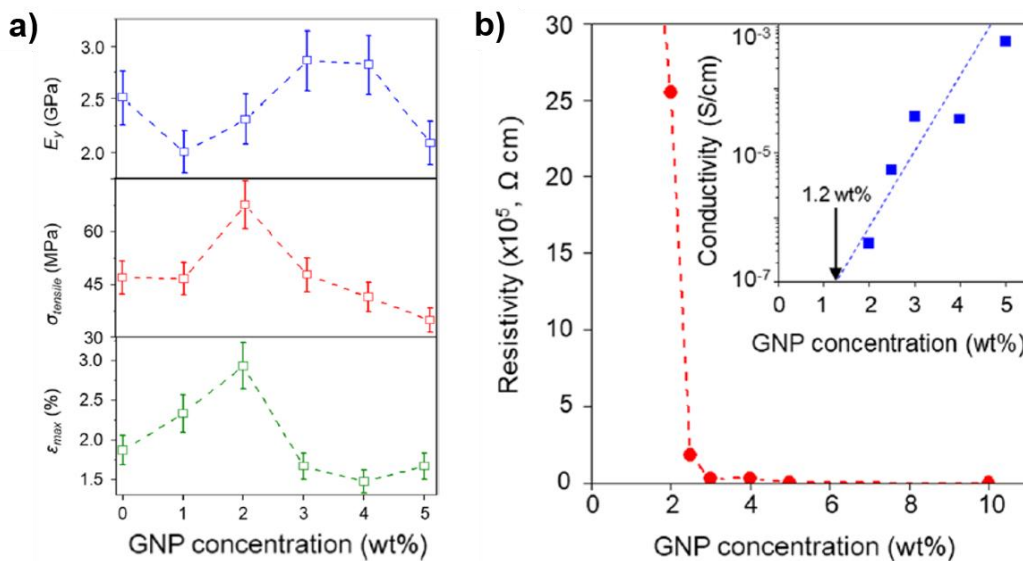
Figure 1.10 The changes with respect to GNP concentration of a) elastic modulus (E_y), tensile strength ($\sigma_{tensile}$), and maximum strain at fracture (ε_{max}), b) resistivity of PLA/GNP composite[52].

1.2.2.2   PLA/GNP/Multi-Walled   Carbon   Nanotube   (MWCNT) Nanocomposite

PLA has a low thermal conductivity value as it was mentioned before. Nanocomposites that consist of carbonaceous materials show enhanced thermal properties besides electrical conductivity. Ivanov et al. made a study to investigate the thermal effects of adding GNPs and MWCNTs both together and separately[53]. The matrix and fillers were mixed with the melt extrusion method. The mixtures were pelletized and then a filament with a diameter of 1.75 mm was obtained using an extruder. The composites with only 1 or 2 types of fillers with different

14

compositions were prepared. The electrical and thermal conductivity values of these composites are given in Table 1.1[53]. It can be said that GNP increased the thermal conductivity more than MWCNTs at the same filler content. The highest value of 0.577 W/m.K was obtained with 6 wt. % GNP addition. Moreover, a synergistic effect was reported upon the formation of bi-filler composites. This effect can be explained by the fact that the agglomeration of GNPs was inhibited by MWCNTs. In addition, it was also mentioned that dispersion of fillers in the matrix also has a significant effect on the conductivities.

Table 1.1. Electrical and thermal conductivities, and thermal diffusivity of different composites mixed in different proportions[53].

Composition Code (wt.%)	Electrical Conductivity (S/m)	Thermal Conductivity (W/mK)	Thermal Diffusivity (mm^2/s)
PLA	7.3×10^{-10} ($\pm 3.39 \times 10^{-10}$)	0.205 ($\pm$0.0045)	0.154 ($\pm$0.0002)
PLA/1.5% GNP	2.51×10^{-8} ($\pm 1.48 \times 10^{-9}$)	0.2695 ($\pm$0.014)	0.245 ($\pm$0.0001)
PLA/3% GNP	9.9×10^{-8} (2.97×10^{-8})	0.3748 ($\pm$0.0011)	0.3079 ($\pm$0.0002)
PLA/6% GNP	0.00835 ($\pm$0.00233)	0.577 ($\pm$0.0151)	0.485 ($\pm$0.0018)
PLA/1.5% MWCNT	1.4×10^{-8} ($\pm 2.83 \times 10^{-9}$)	0.2275 ($\pm$0.0026)	0.1887 ($\pm$0.0001)
PLA/3% MWCNT	7.86×10^{-4} ($\pm 4.86 \times 10^{-4}$)	0.2612 ($\pm$0.0026)	0.1859 ($\pm$0.0001)
PLA/6% MWCNT	0.021 (0.00707)	0.303 ($\pm$9.9.10-4)	0.221 ($\pm 8.7 \times 10^{-4}$)
PLA/1.5% GNP/1.5% MWCNT	5.4×10^{-7} ($\pm 7.07 \times 10^{-8}$)	0.3013 ($\pm$0.0071)	0.2339 ($\pm$0.0002)
PLA/1.5% GNP/4.5% MWCNT	0.0585 ($\pm$0.0318)	0.3779 ($\pm$0.0031)	0.2551 ($\pm$0.0001)
PLA/3% GNP/3% MWCNT	0.036 ($\pm$0.0112)	0.4253 ($\pm$0.0213)	0.3138 ($\pm$0.002)
PLA/4.5% GNP/1.5% MWCNT	0.00244 ($\pm 8.56 \times 10^{-4}$)	0.4692 ($\pm$0.0228)	0.3971 ($\pm$0.005)

1.3 Hexagonal Boron Nitride (h-BN)

Boron nitride (BN) has always been a versatile yet demanding material. W.H. Balmain obtained BN for the first time by combining potassium cyanide and boric oxide in the 1840s. In terms of compounds, BN is considered to be the closest approximation of all types of carbon. Since carbon (C) is next to both boron and nitrogen in the periodic table, BN phases are isoelectric with C phases. It means that they have the same electron configuration as the equivalent phases. Examples include graphite and hexagonal boron nitride (h-BN), diamond and cubic boron nitride (c-BN), and graphene and hexagonal boron nitride nanosheets[54]. Representation of the atomic arrangement of h-BN and graphite, and c-BN and diamond can be seen in Figure 1.11[55].
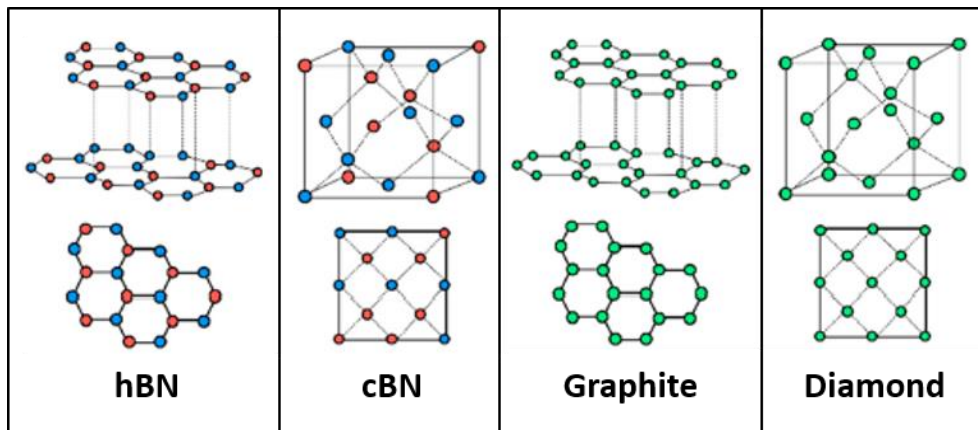
Figure 1.11. The atomic structures of h-BN, c-BN, graphite, and diamond[55].

The majority of the interest in h-BN which is the most prevalent and stable form of BN began with the isolation of graphene sheets in 2004. As can be seen in Figure 1.11, h-BN has a layered structure similar to graphite. There is strong covalent bonding between the boron and nitrogen atoms in-plane part of the structure. The weaker van der Waals forces hold together these layers in the through-plane direction[56]. h-BN has drawn more attention than graphite for some electronic applications because it has a wide intrinsic band gap (E_g) around 5.9 eV. In addition, thermal conductivity of h-BN is 400 W/m.K in-plane and 30 W/m.K through-plane direction[57]. Other properties like oxidation resistance, interlayer spacing, etc. are listed in Table 1.2 to show the similarities between h-BN and graphite [58]. Besides the thermal conductivity, h-BN is stable up to 840 °C. Therefore, it was used for oxidation-resistant coatings [59]. In addition, Kimura et al. proved that h-BN has the effect of reducing wear[60]. This property can also be seen for graphite and molybdenum disulfide (MoS_2). It was mentioned that the common features of these three materials are that they have hexagonal structures. The easy sliding of this structure along the base planes enables it to be used as a lubricant.

Table 1.2. Properties of h-BN and graphite (Adapted from Jiang et al.)[58].

Properties	hBN	Graphite
Bond Length (nm)	0.144	0.142
Bond Energy (eV)	4	3.7
Interlayer Spacing (nm)	0.333	0.335
Young's Modulus (TPa)	0.81-1.3	1.1
In-plane Thermal Conductivity (W/m.K)	400	2600
Band Gap (eV)	5.5-6	~ 0
Breakdown Voltage (MV/cm)	~ 7	Conductor
Oxidation Resistance (^{o}C)	~ 840	~ 600
Appearance Color	White/semi-transparent	Black

1.3.1 Thermal Conductivity Mechanism

The heat can be transferred through convection, radiation or conduction and conduction is the main mechanism for solid materials. Thermal conduction can be described differently for electrically conductive and insulative materials[61,62]. Electrons contribute dominantly to the heat transfer for conductive materials; however, particle vibration movement is managing the transfer for the insulative ones. Heat energy is transferred from one particle to the adjacent one through phonon transfer. The transfer can be explained to be happening from atoms of high vibrational frequency to atoms of low frequency in a particle. Heat is then partially transmitted to the environment by conduction or radiation once it has reached the sample's opposing surface[63]. A phonon can be described as the number of vibrations of atoms in a crystal lattice and it can be called as a quasi-particle because it is not a physical particle. Point defects, dislocations, grain boundaries, interfaces and discontinuities, phonon-phonon scattering, etc. cause a decrease in phonon transfer pace so they decrease the heat transfer efficiency of the material [64,65]. Figure 1.12 (a) schematically shows how a defect acts as an obstacle for heat transfer. The heat cannot flow from one end to the other since the vacancy divides the energy and

17

changes the direction of flow. Another example is the boundary gap as shown in Figure 1.12 (b), where heat flow is cut off due to the boundary gap[66].

a) Defect
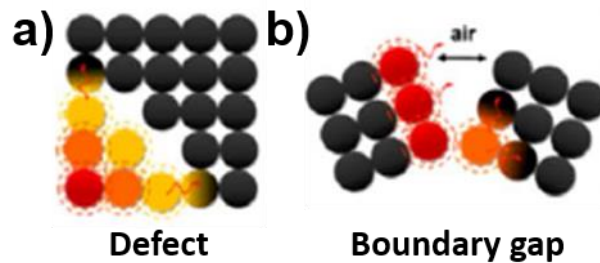
b) Boundary gap

Figure 1.12. Schematics showing how heat transfer mechanism is affected by a) a defect and b) a boundary gap[66].

Lindsay et al. made a comparison between the effect of the boundary and impurity scattering, phonon-phonon scattering, and isotopically impurity with respect to the lateral size change of the material to the heat transfer ability as can be seen in Figure 1.13 (a)[67]. The dashed blue line (κ_L^{iso}), has isotopic impurity and boundary scattering, the red line (κ_L^{pure}), has a boundary and phonon-phonon scattering and is isotopically pure, and the third black line (κ_L^{nat}) has all isotopic, boundary impurity and the phonon-phonon scattering. These three lines represent the single-layer h-BN and the lowest dashed black line (κ_{hBN}) represents the multi-layer h-BN. This comparison clearly states that phonon-phonon scattering is more dominant compared to isotopic scattering. In pristine h-BN, phonon scattering occurs due to the through-plane vibrations. These vibrations are caused by a stacked multi-layered structure so the path of the vibrations is divided into these interlayers[68]. Lindsay et al. made another comparison to show the effect of both the layer number and lattice mismatch in the meaning of isotopic purity. Graph in Figure 1.13 (b) shows the changes in thermal conductivity with temperature. The green solid and dashed lines represent single-layered h-BN and the red ones represent the pristine h-BN. The dashed lines are isotopically pure, meaning all boron atoms are ^{11}B and the solid lines are the natural form of h-BN. It is clear to see that isotopically pure h-BN shows way better thermal conductivity than its natural form. In addition, single-layered h-BN shows higher values than the pristine one due to the prevention of the interlayer scattering of the

phonons. After the peak point for all curves, phonon scattering becomes the dominant mechanism, thus, the thermal conductivity values are found to decrease[67].
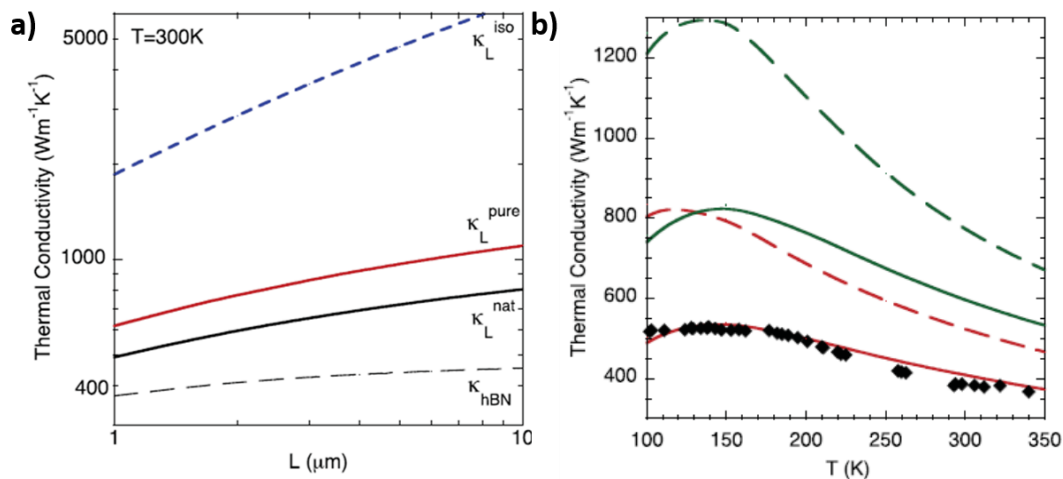
Figure 1.13. The changes in thermal conductivity (W/m.K) with respect to a) the lateral size (μm) change at 300K and (b) temperature (K) change. In (a) the blue dashed (κ_L^{iso}), the red solid (κ_L^{pure}), and the black solid (κ_L^{nat}) lines are single-layer hBN including isotopic impurity and boundary scattering (highest curve), boundary and phonon-phonon scattering and isotopic purity (upper curve), and boundary impurity, phonon-phonon scattering and isotopic purity (lower curve) respectively. The lowest dashed gray line (κ_{hBN}) shows the multi-layer hBN[67]. In (b) the solid lines represent the calculated theoretical values of natural multi-layer (red) and single-layer (green) h-BN. The dashed lines show the isotopically pure multi-layer (red) and single-layer (green) h-BN. The black diamonds show the measured values for natural multi-layer h-BN[67].

In addition to those parameters affecting the thermal conductivity mentioned above, composite structures have additional parameters like filler percentage and distribution uniformity of the fillers. A representation of a sample case where heat transfer is affected by the interface between the matrix and the filler can be seen in Figure 1.14 (a)[66]. Heat is applied to the crystal filler material and conducted from one end to the other. After being transferred to the polymer matrix, it began to disperse in all directions instead of an aligned conduction path. This is due to the disordered structure of the polymers, due to the vibration of the whole chain and increased phonon scattering. Moreover, filler content is also a crucial parameter in obtaining a continuous and favorable heat transfer path. For example, if the fillers

are not continuously connected to each other, the heat will spread over the polymer matrix instead of being transmitted in the desired direction. This case is schematically represented in Figure 1.14 (b). Provided that a continuous path is not obtained, it can be said that the amount of heat transferred will be low and the transfer will be slow [69,70].
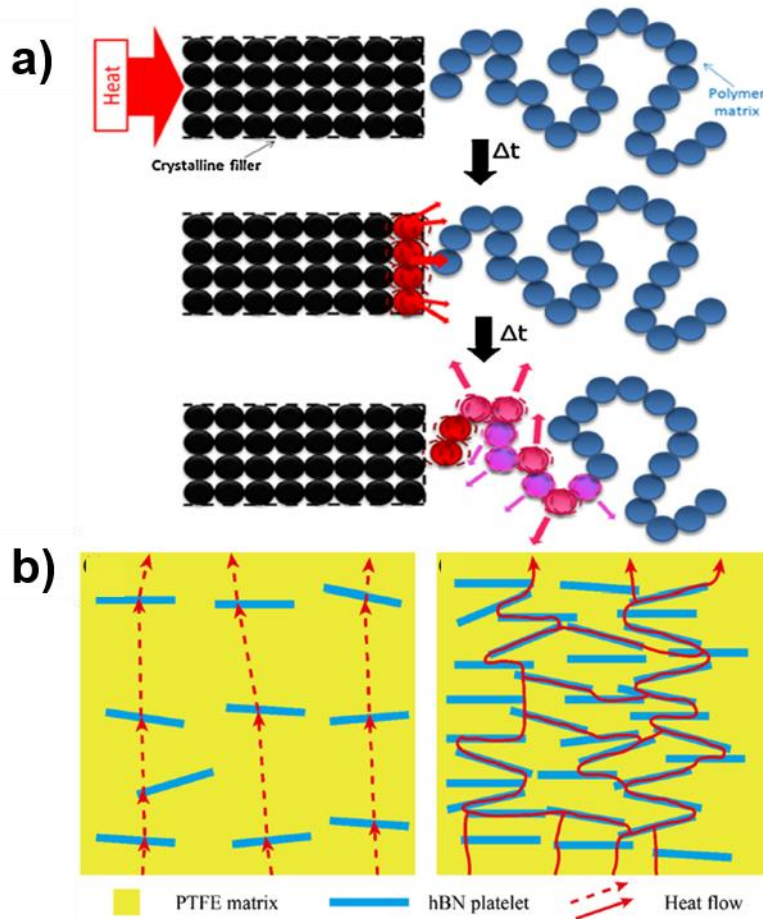
Figure 1.14. Schematic representation of heat transfer a) from fillers to the matrix[66], b) with respect to the amount of fillers in the matrix[70].

1.3.2   3D Printed h-BN Filled Composites

1.3.2.1   FDM 3D Printed Liquid Crystal Polymer (LCP) /h-BN Composite

Luo et al. produced a h-BN filled polymer matrix composite via additive manufacturing to investigate the changes in the thermal conductivity of the composite [71]. LCP has a more ordered structure than amorphous liquids. In addition, all chains of LCP tend to orient along the extrusion direction. In this study, the effect of lateral sizes of h-BN flakes (sizes of 0.5 μm, 5 μm, and 50 μm) on 3D printed sample's thermal conductivity were investigated. LCP and h-BN were pre-mixed and formed into a filament using a twin-screw extruder. Figure 1.15 shows that higher lateral flake size affected the thermal conductivity value, especially in the in-plane direction. The percentage of the filler was 20 wt.% in these composites and the in-plane thermal conductivity value of bare LCP was 0.74 W/m.K. Following the addition of h-BN flakes with a lateral size of 50 μm, the in-plane and through-plane conductivity values increased to 1.77 W/m.K and 0.4 W/m.K, respectively.
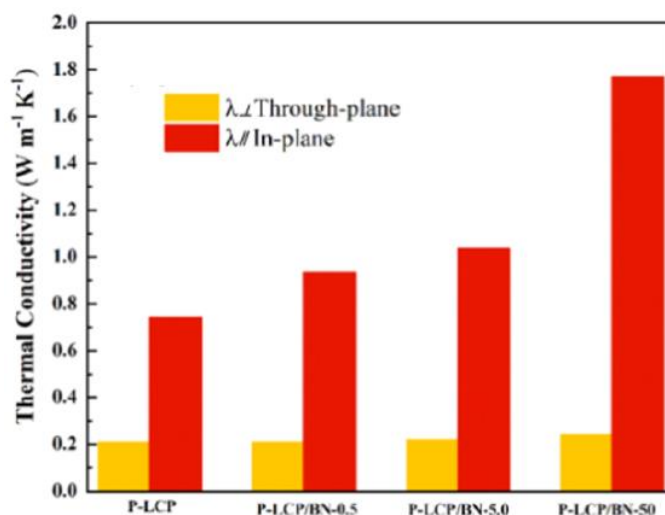
Figure 1.15. Thermal conductivity comparison of different lateral sized h-BN filled LCP matrix 3D printed composites[71].

Moreover, the heat dissipation performance of the 3D printed samples was also compared with a thermal camera, results of which are provided in Figure 1.16.

Although the composites reached the same value at the end, composite with the largest lateral sized h-BN flakes was the first to reach these values. Therefore, the performance of the samples was consistent with the thermal conductivity values.
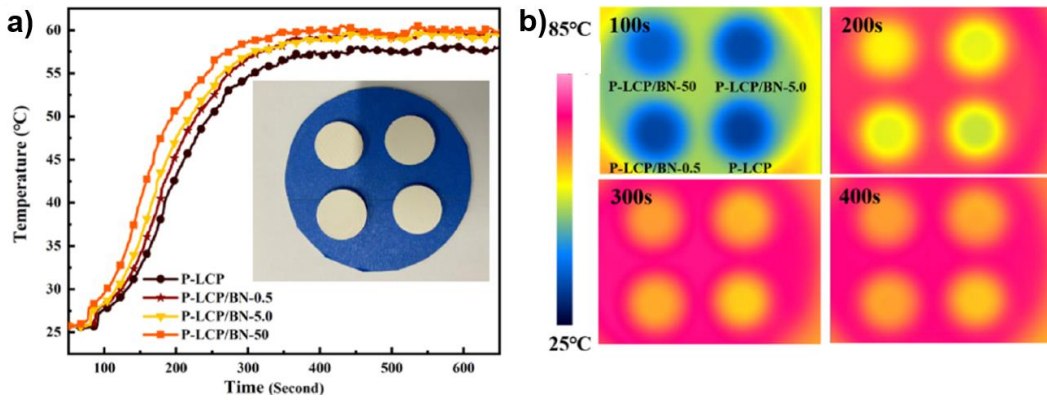
Figure 1.16. Heat dissipation performance comparison of 3D printed composites[71].

1.3.2.2   FDM 3D Printed TPU/h-BN Composite

Guo et al. compared the effect of size, orientation, and the amount of the h-BN for 3D printed objects[72]. h-BN with two different particle sizes (2.6 μm and 19.2 μm) were used for this work and they were not exfoliated. The matrix and filler materials were mixed through the solution mixing method and formed into a filament using a twin-screw extruder. The directions of printed objects were labeled as k_1, k_2, and k_3 as clarified in Figure 1.17 (a), and the thermal conductivity results of the samples are compared in Figure 1.17 (b). It can be said that the sample showed higher thermal conductivity value in the printing direction (k_1) than the through printing direction (k_3). It is valid for all h-BN contents and for both small (S) and large (L) lateral-sized h-BN particles. In addition, small-sized h-BN/TPU composites showed a higher conductivity value for h-BN content lower than 40 wt.%. In samples with low h-BN content, the number of voids was lower when smaller h-BN particles were used compared to larger h-BN particles. Another point is that the conductivity value was found to increase with the h-BN content. Therefore, creation of a thermal pathway

22

with large sized h-BN particles at high loading fractions (>40 wt. %) was preferable for composites with high thermal conductivity.
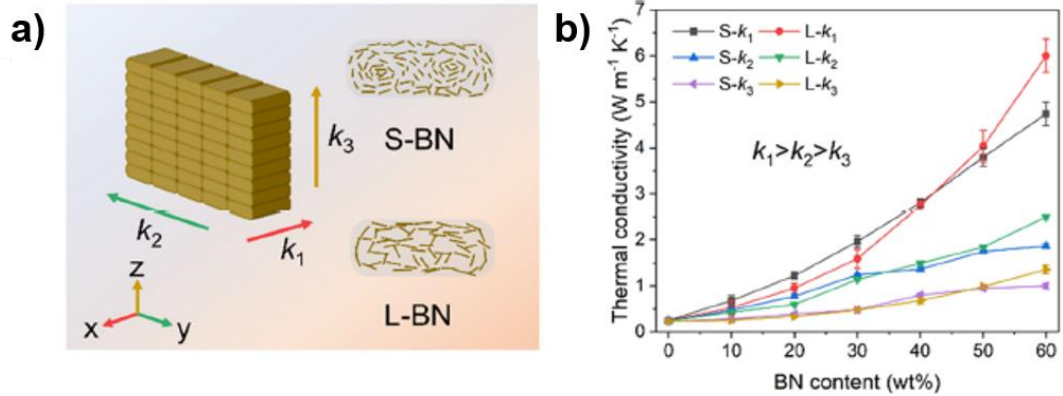
Figure 1.17. a) Schematic representation of directions of the 3D printed object and the different sizes of h-BN. b) Thermal conductivity comparison of 3D printed objects with respect to the content and the size of h-BN[72]. In (b) the black and red (the upper), the blue and green (the middle), and the purple and yellow (the lower) lines represent the small and large-sized h-BN in k_1, k_2 and k_3 direction respectively.

Heat sink models were 3D printed with bare TPU and 50 wt. % loaded large size h-BN/TPU to show the heat dissipation performance. The comparison was made between 3D printed objects and an aluminum heat sink. Samples were placed on the heater and the temperature change was monitored by thermocouples. The heat sinks were placed on the heater without any thermal interface material (TIM) in the first experiment and h-BN/TPU and aluminum heat sinks showed exactly the same performance, as shown in Figure 1.18 (a). Obtained results were not reasonable. In the second experiment, TIM was used between the heat sinks and the heater, and a difference was observed between h-BN/TPU and aluminum. This was because the effect of the air gap between the heater and the heat sink was minimized as can be seen in Figure 1.18 (b).
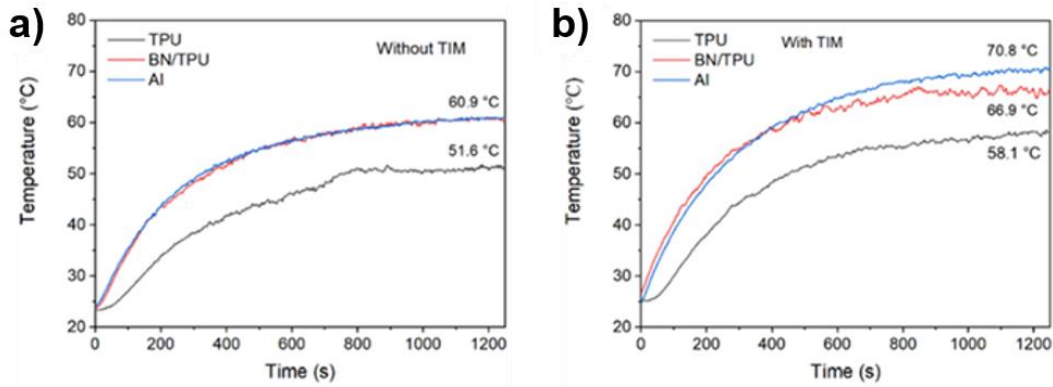
Figure 1.18. Heat dissipation performance comparison of Al, bare TPU and h-BN/TPU heat sinks a) without and b) with a TIM[72].

1.4   Motivation of This Thesis

Thermally conducting yet electrically insulating composites are required for the thermal management of electronic devices as mentioned earlier. The prototypes of complex structures can be produced and optimized by 3D printing for these composites. Moreover, decreasing the number of layers of h-BN can significantly increase its heat dissipation performance. The mentioned exfoliation yields of h-BN were high but exfoliated materials had generally more than 10 layers. There are some works including 3D printing of h-BN for thermal management but at the time of writing this thesis there is only one publication on the use of exfoliated h-BN. In addition, h-BN filled PLA matrix composites were not investigated for these applications. Furthermore, 3D printing of a LED bulb holder to extend its lifetime using a h-BN/PLA filament was investigated for the first time.

In Chapter 2, the experimental details were provided in detail. The exfoliation mechanism, the methods both used in the literature and in this thesis were discussed in Chapter 3. In Chapter 4, the effect of exfoliation on uniformity of h-BN dispersion in the matrix and filament production were analyzed. This chapter also includes the investigation of heat dissipation performances of 3D printed heat sink and LED bulb holder in detail. In Chapter 5, the results were summarized and recommendations for future work were discussed.

CHAPTER 2

EXPERIMENTAL DETAILS

2.1   Materials Used

Polylactic acid (PLA) used for the experiments was labeled as Luminy L175 produced by Total Corbion. The density of PLA was 1.25 g/cm^3. Melting temperature and glass transition temperature of PLA were 175°C and 60 °C, respectively. Hexagonal boron nitride (h-BN) powders with lateral sizes of 900 nm - 1 μm were used for the experiments supplied from BORTEK, Boron Technologies, and Mechatronics Inc., Turkey. The density of h-BN was 2.3 g/cm^3, and electrical resistance was about 3100 Ω.cm at 1000 °C. Isopropyl alcohol (IPA) with a purity of 99.5% was used for the exfoliation process supplied by Sigma-Aldrich. The urea used for ball-milling was supplied by ISOLAB Chemicals in powder form. It had a density and purity of 1.34 g/cm^3 and 99.0 %, respectively. The chloroform used for mixing PLA and h-BN had a purity of 99.5% and purchased from Sigma-Aldrich. The LED bulb used for the experiments was Ecolite 5 Watt (W) and 470 lumens (lm) LED bulb and the thermal conductivity of the paste used for assembling bulb parts was 8.3 W/m.K and produced by Zalman Cool Innovations.

2.2   h-BN Exfoliation

2.2.1   Shear Exfoliation

The shear exfoliation method was used for decreasing the number of layers of h-BN. Pristine micron-sized h-BN powder was mixed with 260 ml IPA and 940 ml DI water. The solution was ultrasonicated in an EVEREST ULTRASONIC device for an hour and poured into the jacketed beaker that was stabilized at 8 °C using a water

circulatior (CLRC-08C refrigerated circulator by CLS Scientific Co. LTD). The solution was shear exfoliated at 8000 rpm for 4 hours using L5M-A SILVERSON laboratory shear mixer as can be seen in Figure 2.1. After exfoliation, the solution was vacuum filtrated and placed in a vacuum furnace overnight. The powder form of h-BN was then mixed with the same amount of IPA and DI water again. The solution was sonicated for 1 hour and then it was re-exfoliated with the same parameters. The solution was left in the beaker for 3 days and the supernatant was collected. Both supernatant and precipitated h-BN were vacuum filtrated and placed in a vacuum furnace overnight separately. The same sonication and shear exfoliation steps were applied one last time to the precipitated h-BN. This time the solution was left in the beaker for 3 days and the supernatant and precipitate were vacuum filtrated and dried in the vacuum oven overnight. Recycled supernatant parts that were collected in steps two and three were used for further processes.

Figure 2.1. Photograph of shear exfoliation device.

2.2.2 Ball-Milling Exfoliation

The ball-milling method was also used for the exfoliation of h-BN. Micron-sized h-BN powders and urea were mixed at a ratio of 1:60 and transferred to a custom-made PTFE coated steel jar with 10 zirconia balls with diameter of 10 mm. The jar placed in the Planetary Ball Mill PM 100 device (Retsch) as can be seen in Figure 2.2, was set at a rotational speed of 300 rpm and at room temperature for 20 hours. A break time of 5 minutes was set for each hour. After 20 hours, the powder obtained was dispersed in water and kept in an ultrasonic bath (EVEREST ULTRASONIC) for 1 hour with the addition of 100 ml of IPA. Then, the solution was centrifuged at 3000 rpm for 15 minutes using the HERMLE Z 326 device, the supernatant was taken, and exfoliated and non-exfoliated h-BNs were separated. Then, it was centrifuged again at 6000 rpm, so that all of the h-BN nanosheets adhered to the inner surface of the centrifuge tube, and the urea was removed by pouring the supernatant. The h-BN nanosheets collected from the inner surface of the tubes with DI water was filtrated on a PTFE filter with a 0.22 μm pore size using vacuum filtration, and the remaining urea was removed by long-term washing.

Figure 2.2 Photograph of ball-milling device.

2.3 Preparation of h-BN/PLA Nanocomposite Films, Filaments and 3D Printing

2.3.1 Solution Mixing of h-BN/PLA

PLA granules were mixed with chloroform at 60 °C, and when they were completely dissolved, they were mixed with exfoliated h-BN solution. This nanocomposite solution was mixed on the hotplate with a magnetic stirrer until it became viscous. The viscous solution was poured into a glass petri dish and left overnight in the vacuum oven at 60 °C to remove the remaining solvents and moisture. Finally, the solid h-BN/PLA composite separated from the petri dish was obtained in powder form with homogeneous size distribution using a blade grinder (IKA A11 basic).

2.3.2 Production and Heat Dissipation Capability Test of h-BN/PLA Films

Some of the mixed composites were separated to be produced in film form. As can be seen in Figure 2.3, films that have the same length, width, and thickness were produced using a Dr. Blade. They were placed onto an indium tin oxide (ITO) coated glass heater. The films were placed in the following order from left to right: exfoliated h-BN/PLA, pristine h-BN/PLA, and bare PLA. The heat transfer rates were monitored using the APPLENT AT4508 device with eight thermocouples. The films were covered with a box cut according to the glass to reduce the effect of the ambient temperature as much as possible.
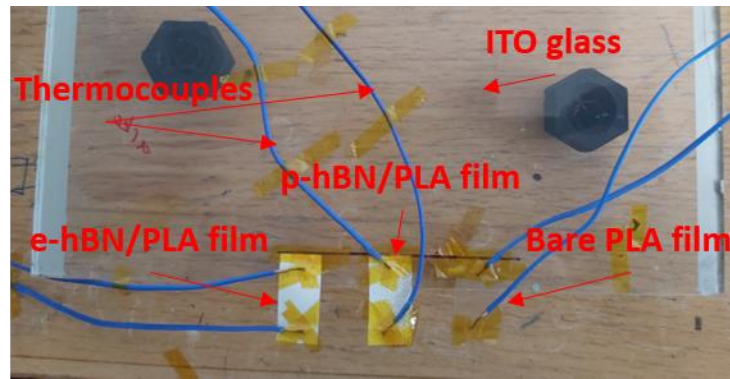
Figure 2.3. Photograph of heat dissipation capability test setup.

2.3.3   Filament Drawing

Twin-screw extruder (MicroLab 400 Twin Screw Extruder) was used to create filament shape from the powder material, but it was not enough to provide continuity in terms of shape and diameter. Keeping the filament coming out of the end of the extruder on the surface with straight oscillation prevents the production of homogeneous thickness with the effect of the weight of the accumulated filament. As soon as the filament leaves the device, it must be cooled in a controlled manner and drawn in the same direction at a controlled speed. The filament winding device (seen in Figure 2.4) was constructed to solve this problem. This device pulls the filament from the end of the extruder, passes it over the fan, lowers its temperature at a certain rate, and passes it through the sensor case. The sensor constantly measures the thickness value and sends the data to the Arduino. According to this data, Arduino controls the speed of the stepper motors. It adjusts the pulling speed of the filament by using the Proportional Integral Derivative (PID) mechanism. PID mechanism finds the difference between the values of the output that is demanded and the output that the system gives called an error. The feedback system is the working principle of the PID controller. This error is sent to PID, and PID multiplies the value with a coefficient calculated, then it takes the derivation and integral of it, and sends it to the output again. This process renews itself until the error is minimized[73,74]. For example, if the thickness data is higher than the target value of

1.75 mm, the stepper motor starts to run faster to decrease this value. Otherwise, it decreases its speed according to the feedback mechanism as mentioned above. As seen in Figure 2.4, 1.75 mm diameter filament was obtained by cooperative working of twin-screw extruder with the filament winder device. The zone temperatures of the twin-screw extruder were set as 150, 180, 185, 185, and 150 °C, from the material feeding hole of the extruder to the extrusion point. The PLA and h-BN/PLA filaments were produced with these parameters and methods.
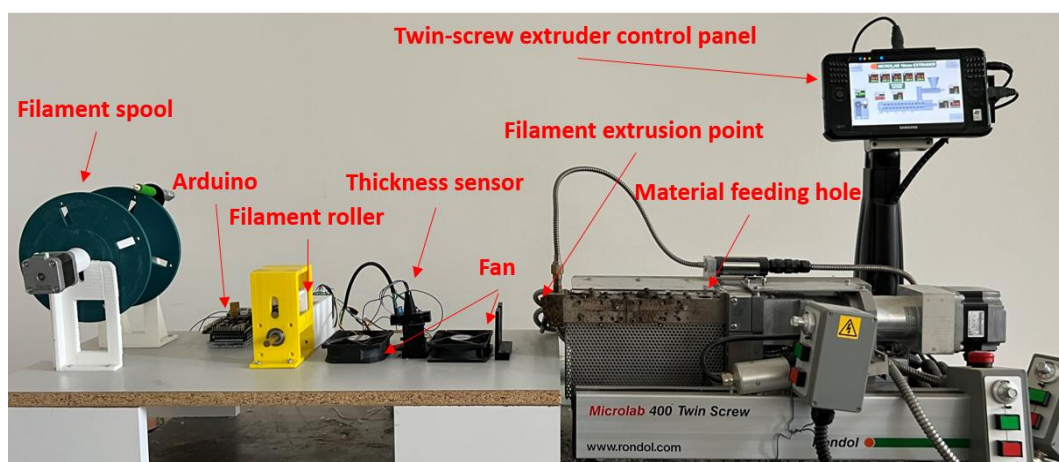
Figure 2.4. Photograph of the filament production setup with the filament winder and the twin-screw extruder.

2.3.4 3D Printing of Bare PLA and h-BN/PLA Nanocomposite Filaments

Autodesk Inventor Professional 2018 software was used for the design of samples and Prusa Slicer 2.3.0 was used to set the printing parameters of these designs as can be seen in Figure 2.5 (a) and (b), respectively. Prusa i3 MKS3 3D Printer is open source and has a print volume of $250 \times 210 \times 210$ mm for 3D printing of filaments. 3D printing of LED bulb holder design from PLA and h-BN/PLA filament by this 3D printer was shown in Figure 2.5 (c) and (d), respectively. Printing parameters set for PLA filament were 215 °C for the nozzle temperature and 70 °C for the bed temperature and same nozzle temperature but 60 °C as a bed temperature set for h-BN/PLA filament. The other parameters were set as 0.1 mm for layer height, 100 % infill, ± 45° for printing orientation. Moreover, the rectilinear pattern was chosen for

filling and a 1 mm brim was used for each printing. The cooling settings for PLA were 35% minimum and 100% maximum fan speed and the fan was always on. However, the fan was not left on all the time for h-BN/PLA filament printing and fan speed limitations were the same for 3D printing of the heat sink. Meanwhile, the fan speed was configured for the LED bulb holder printing to be 20% for minimum and 50% for maximum. In addition to the fan speed change, support was also used for the LED bulb holder printing.
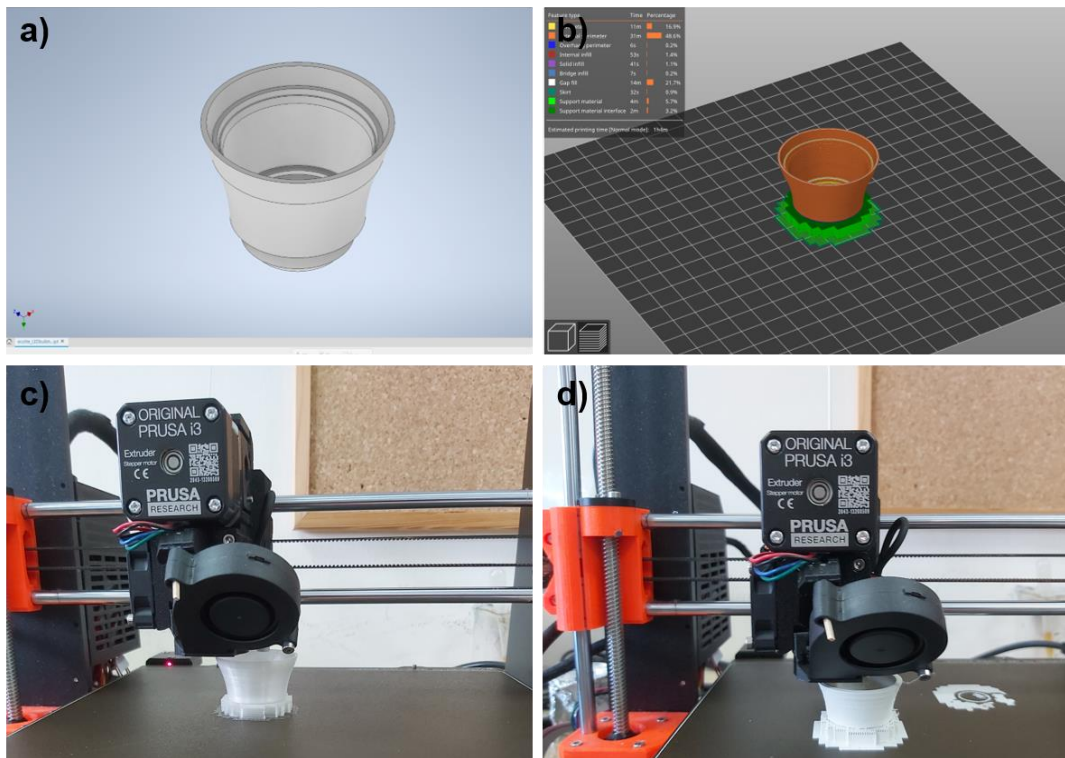
Figure 2.5. LED bulb holder design's a) drawing view from Autodesk Inventor Professional 2018, b) sliced view from Prusa Slicer 2.3.0. Photos during 3D printing by Prusa i3 MKS3 of c) PLA and d) h-BN/PLA filament.

2.3.5 Heat dissipation performance comparison of aluminum, 3D printed PLA, and 3D printed h-BN/PLA heat sink

The heat sink comparison between these three models was monitored by a thermal camera (Optris PI 400029T900). The experiment setup is shown in Figure 2.6. A

semi-conductor plate was placed on the commercial metal heat sink and double-sided thermal conducting tape (3M 8708 type, 0.6 W/m.K) was stuck on this plate. As can be seen in Figure 2.6, a thermal camera was placed on top of this system. In the experiment, 4V was applied on a semi-conductor plate after the heat sink was placed for 120 seconds. Thermal camera software was used to measure the average temperature in the area indicated on the heat sink. In addition to this measurement, a line was defined and passed throughout the heat sink to measure the temperature of all points on this line. The temperature distributions of both this area and line will be discussed in the results and discussion part.
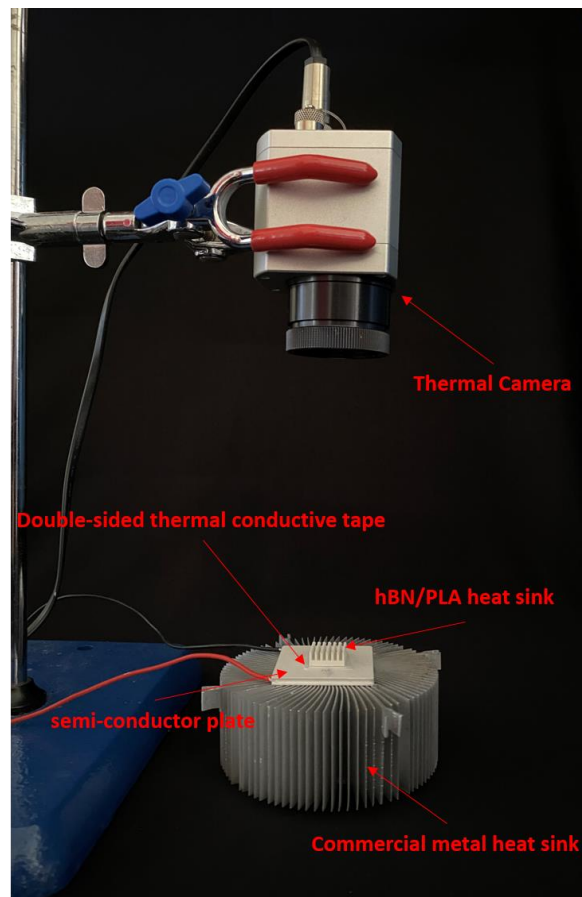
Figure 2.6. Photo of heat dissipation performance setup on the heat sink.

2.3.6 Heat dissipation performance comparison of commercial, 3D printed PLA, and 3D printed h-BN/PLA LED bulb holder

The commercially available Ecolite LED bulb was disassembled without damaging the bulb, photos of which are provided in Figure 2.7 (a). Following the separation of the LED chips, lamp housing, and socket, the bulb holder was placed in 0.1 M potassium hydroxide (KOH) solution to separate it from the metal heat dissipator. After complete dissolution of the heat dissipator, the bulb holder was removed from the solution without getting harmed and placed in a vacuum furnace for drying. 3D printed PLA, h-BN/PLA, and commercial bulb holders were assembled with LED chips and sockets. As the last step, thermal conducting paste (8.3 W/m.K) was applied to the junction points of led chips and bulb holders as can be seen in Figure 2.7 (b).
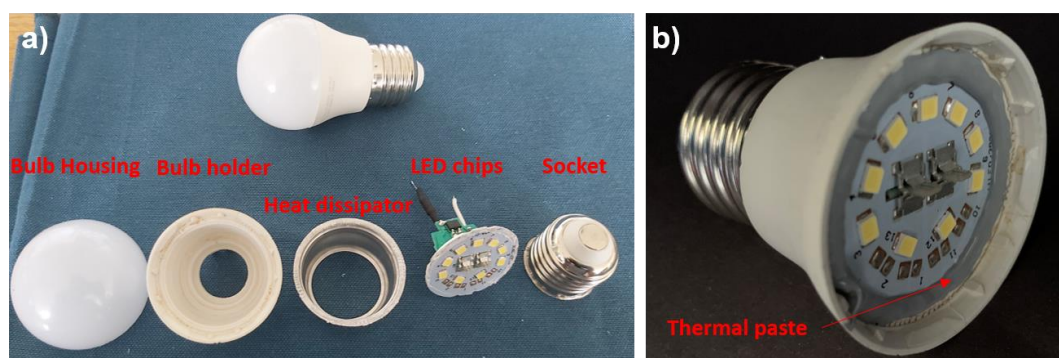
Figure 2.7. Photos of a) disassembled parts of the LED bulb and b) reassembled LED bulb.

LED bulbs were placed into the bulb socket and it was inserted into the plug socket. A thermal camera was placed on top of the experiment setup. The temperature changes on the LED chips were recorded when 220 V was applied to them as can be seen in Figure 2.8. The voltage was applied for ten minutes and then power was cut off and the thermal camera recorded both heating and cooling instances. The box was also placed around the setup to both minimize the effect of surroundings and avoid the bright light during the experiment.
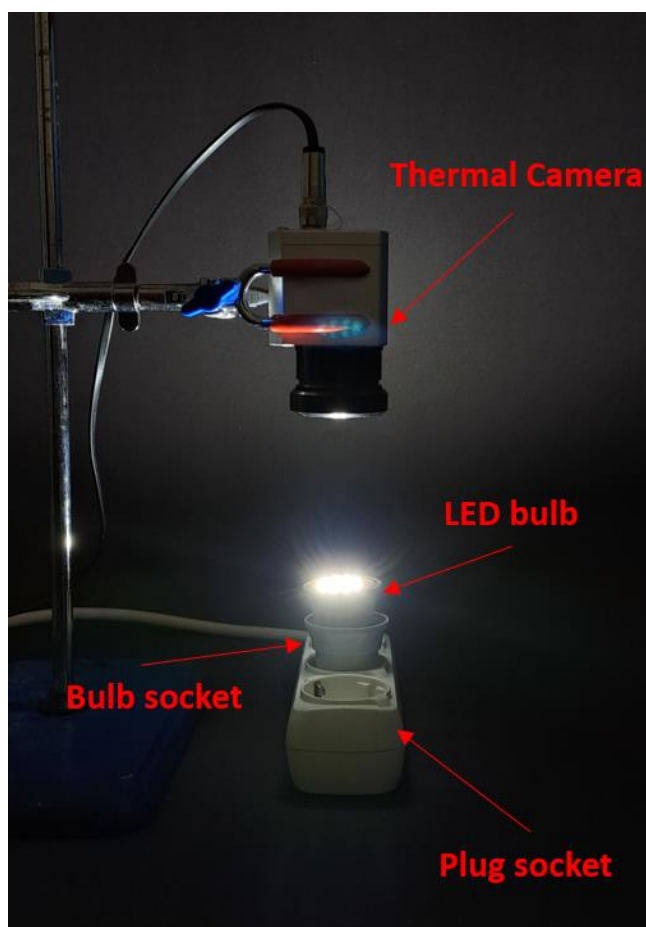
Figure 2.8. Photo of heat dissipation performance of LED bulb holder experiment setup.

2.4 Characterization of h-BN, h-BN/PLA Nanocomposite Films, Filaments, and 3D Printed Parts

2.4.1 Scanning Electron Microscopy (SEM)

Morphology differences between the pristine and exfoliated h-BN, ball-milled and shear exfoliated h-BN, uniformity comparison between the pristine h-BN/PLA and exfoliated h-BN/PLA films, h-BN distribution and shape uniformity comparison between the pristine h-BN/PLA and exfoliated h-BN/PLA filaments and structural integrity of the printed parts were investigated by SEM (FEI Nova Nano SEM 430).

Samples were exposed to an accelerated voltage of 5 kV and coated with 5 or 10 nm thick gold layer.

2.4.2 Transmission Electron Microscopy (TEM)

Reduction in the number of layers after exfoliation and the conservation of the (002) plane in the h-BN structure was analyzed by TEM (Jeol 2100F 200kV RTEM). Plane detection was done by calculating the d-spacing value using the GATAN software. TEM sample was prepared by drop casting of aqueous diluted h-BN solution over a holey carbon supported TEM grid.

2.4.3 Atomic Force Microscopy (AFM)

AFM characterization was conducted using non-tapping mode and scanning an area of 10 μm × 10 μm via Veeco Multimode V AS-12 device. It was used to calculate the number of layers in exfoliated h-BN. The diluted h-BN was mixed with the IPA-DI water solution and dropped onto the silicon wafer then it is spin-coated (Spincoat G3-8) at 3000 rpm with an acceleration of 1000 rpm/s for 30 seconds to prepare the AFM sample.

2.4.4 X-Ray Diffraction (XRD)

The crystal structure analysis from the surface was carried out through X-ray diffraction (XRD) using RIGAKU D/MAX 2200 ULTIMA/PC. This device uses Cu Kα radiation, operates at a wavelength of 1.5406 Å to collect the data from the sample. It was used to monitor the changes in thickness.

2.4.5 Raman Spectroscopy

Raman spectroscopy characterization was performed by EMCCD camera (Andor Newton). A laser with a wavelength of 532 nm was used. This method was used to observe the changes in the E_{2g} phonon mode caused by the stretching mode between boron and nitrogen atoms. Raman signals were analyzed with an ANDOR SR750 device.

2.4.6 Tyndall Effect

Another method used to compare the efficiency of exfoliation is the Tyndall effect[75]. The path of the red laser beam appears to be along the path, as supernatant and suspended few/mono-layered h-BN cause light scattering[76].

2.4.7 Thermogravimetric Analysis (TGA)

TGA characterization was made via Exstar SII TG/DTA 7300 to calculate the weight percent of h-BN following the filament production. It was also used to make a comparison of loss amount between the pristine h-BN/PLA and the exfoliated h-BN/PLA. This analysis was performed between 30 °C and 550 °C with a heating rate of 10 °C/min under nitrogen atmosphere.

2.4.8 Laser Flash Apparatus (LFA) Method

LFA analysis was performed via Netzsch LFA 457 Microflash to calculate the thermal diffusivity (k) values of 3D printed bare PLA and h-BN/PLA samples. The experiments were conducted at room temperature. In addition, the specific heat capacity (C_p) values of these samples were also calculated with this method. Finally, densities were calculated by the Archimedes method. The obtained values were used for measuring the thermal conductivity.

CHAPTER 3

Exfoliation of Hexagonal Boron Nitride

3.1   Exfoliation Mechanism

Exfoliation is necessary to increase the thermal conductivity and uniformity in the composite structure as mentioned in the previous chapter. A large contact area is established between h-BN nanosheets to minimize the thermal contact resistance when heat transfers over the layers. Exfoliation makes it possible to distribute h-BN layers uniformly because 2D layers have a tendency to align[77]. This alignment enhances the overlapping area and also reduces the percolation threshold. Percolation threshold can be described as the minimum h-BN amount for the long-range conductivity in random systems[78]. There are numerous ways to exfoliate h-BN in the literature and several of them will be discussed in the following pages.

3.1.1   Ion Intercalation Exfoliation

Ion intercalation for exfoliation of 2D materials is one of the most preferred methods. Besides h-BN, it was applied for molybdenum disulfide (MoS_2)[79], tungsten disulfide (WS_2)[80], graphite, carbon nanotubes (CNNT)[81], and titanium disulfide (TiS_2)[82]. The mechanism and steps of the ion intercalation method are described schematically in Figure 3.1. First, the layered bulk material is placed as a cathode material and Li foil is placed as an anode material. Layered material is intercalated with Li-ions upon the application of a negative electric field. This intercalation weakened the van der Waals bonds between the layers increasing the interlayer spacing. After this step, expanded layered material was ultrasonicated with water or alcohol (ethanol or IPA) medium, Li-ions were separated as LiOH, and layers were peeled off from each other[83].
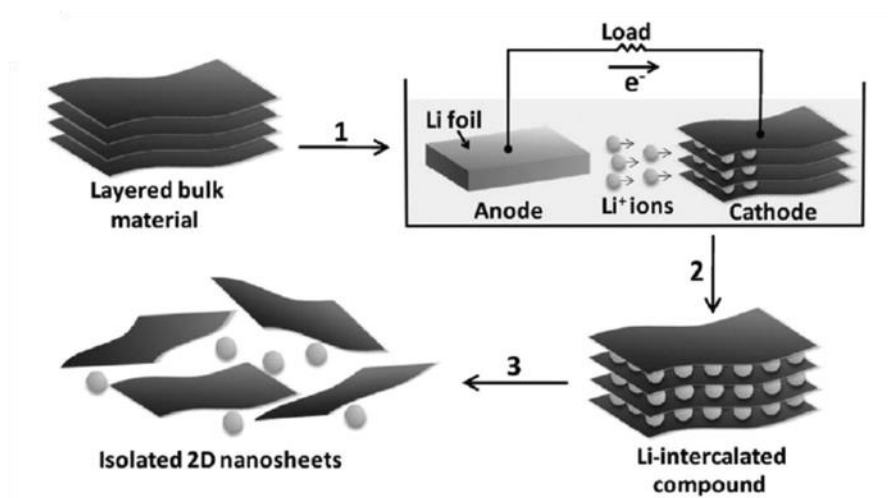
Figure 3.1. Schematic illustration of the Li-intercalated exfoliation process[83].

Ortiz et al. tried to exfoliate the pristine h-BN with ion intercalation. They used potassium (K^+) and zinc (Zn^{+2}) ions as an exfoliation agent and 1 g h-BN was sonicated in water and gelatine medium. According to their results, the lateral size of exfoliated h-BN was between 10-80 nm with a flake thickness between 1-3 nm[84].

3.1.2   Bipolar Electrochemistry (BE) Exfoliation

This method was applied to graphite[85] and WS_2[86] before as well as to the h-BN. The mechanism of this method leans on oxidation and reduction reactions due to the potential differences between the material in the solution and electrodes[87]. Wang et al. applied this method for h-BN and the schematic illustration and photos of this process are provided in Figure 3.2 (a) and (b), respectively[88]. The bulk h-BN particles dispersed in solution were exposed to an external electric field using two platinum electrodes; the particles became polarized and stayed that way even when there was no direct electric contact. The two endpoints of the h-BN particles encountered opposite redox reactions and this caused a peeling off the layers of the bulk structure. The process took place by supplying a steady 10 V DC voltage throughout the two Pt operating electrodes within a 0.5 M sodium sulfate solution with well-dispersed bulk h-BN particles. Sodium sulfate was added to obtain a continuous current path

38

through the solution. Photos of the pristine and exfoliated h-BN solution are provided in Figure 3.2 (c) and (d), respectively. The flake thickness of this exfoliation process was around 8.4 nm, which roughly corresponds to 25 layers[88].
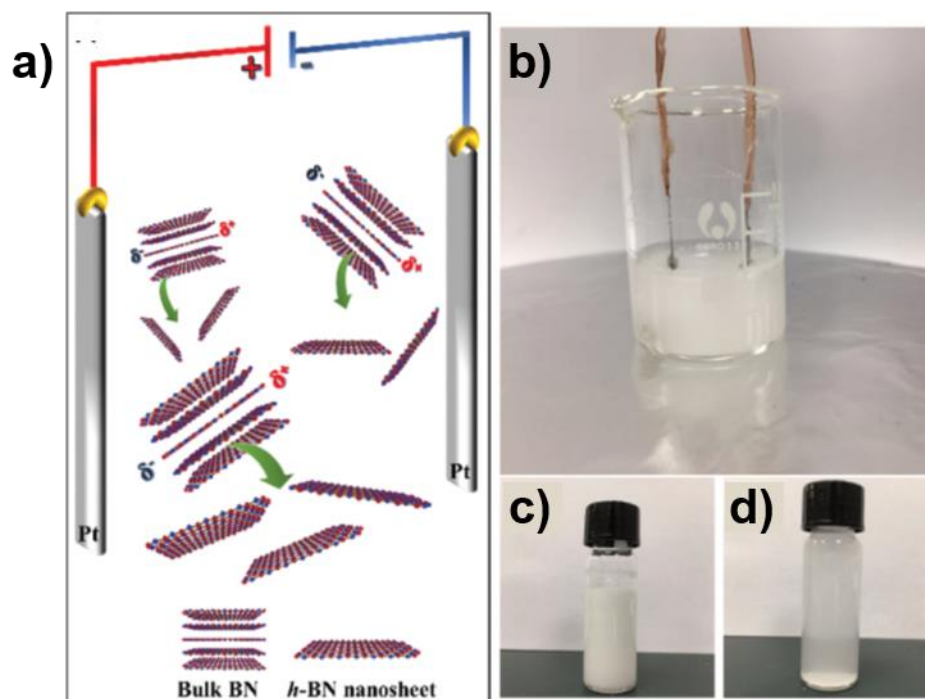
Figure 3.2. a) Schematic and b) photos of BE experiment. c) pristine, and d) exfoliated solution[88].

3.1.3 Molten Hydroxides Exfoliation

Molten hydroxide-assisted exfoliation is a chemical exfoliation method that is used for graphite beside h-BN[89,90]. This method justifies that mechanical exfoliation methods cannot exfoliate h-BN layers effectively due to stronger lip-lip interactions than graphite[91]. The steps of this method can be sorted as; self-curling at the edges of the h-BN layers, then hydroxides are inserted between the layers, and layers are cut with the reaction of hydroxides and h-BN or the layers can be directly peeled off from the parent materials. A schematic for this process is provided in Figure 3.3[92]. Li et al. used this method by adding h-BN powder to the totally crushed NaOH/KOH (molar ratio= 51.5/48.5) hydroxides as a first step. Secondly, they homogenized the

mixture through grinding. As a final step, the mixture was heated at 180 °C for 2 h in a PTFE-lined stainless-steel autoclave. A flake thickness of 4 nm was reported for this technique, which roughly corresponds to 12 layers[92].
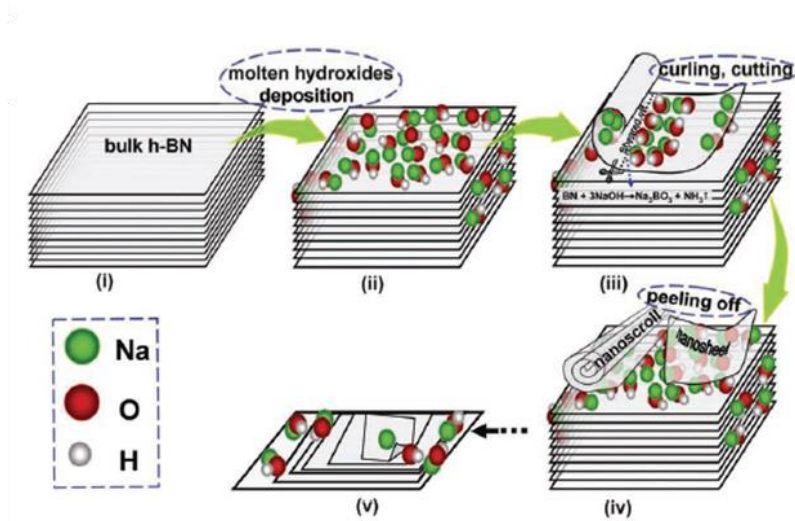
Figure 3.3. Schematic representation of step by step molten-hydroxides exfoliation[92].

3.2 Exfoliation Results

The exfoliation methods mentioned above cannot ensure that the lateral dimensions were maintained, a large amount of h-BN was produced, and the number of layers was found to be less than 10 at the same time. The ball-milling and the shear exfoliation methods were tried to achieve these goals and the results were discussed in the following parts.

3.2.1 Ball-Milling Exfoliation

The process was arranged with the break times to prevent the overheating of the jar. Moreover, urea was used to protect h-BN from mechanical damage, and prevent excessive reduction in the lateral dimension of the material in addition to helping the

exfoliation. IPA was also used to increase exfoliation efficiency during the sonication step.

h-BN exfoliation was confirmed by several characterization methods. First, exfoliation was demonstrated by XRD method, results of which are provided in Figure 3.4. The pristine h-BN (p-hBN) has 5 characteristic peaks (002), (004) (in-plane) and (100), (101), (102) (through-plane). As seen in Figure 3.4, XRD measurement was taken immediately after ball-milling (as-milled) and there were urea-related peaks in addition to the h-BN peaks. These peaks were consistent with the literature[75]. After exfoliation, the urea must be completely removed from the h-BN. Moreover, (002) in-plane peak was shifted to the left side. This is due to expansion of layers caused by intercalation of ammonia ions. In the post-centrifugation liquid (supernatant) mentioned in the experimental details section, urea peaks were still present even though they were low in number. Then, the urea was removed through washing with DI water, which was followed by vacuum filtration onto a filter paper. As can be seen, the peaks originating from urea were disappeared. The final XRD (vac-filtered) showed additional PTFE filter peaks beside the h-BN peaks. After the exfoliation step, the in-plane peaks should have remained the same and the others should have disappeared, demonstrating the reduced thickness/size ratio as evidenced by our XRD pattern named as a vac-filtered[93].
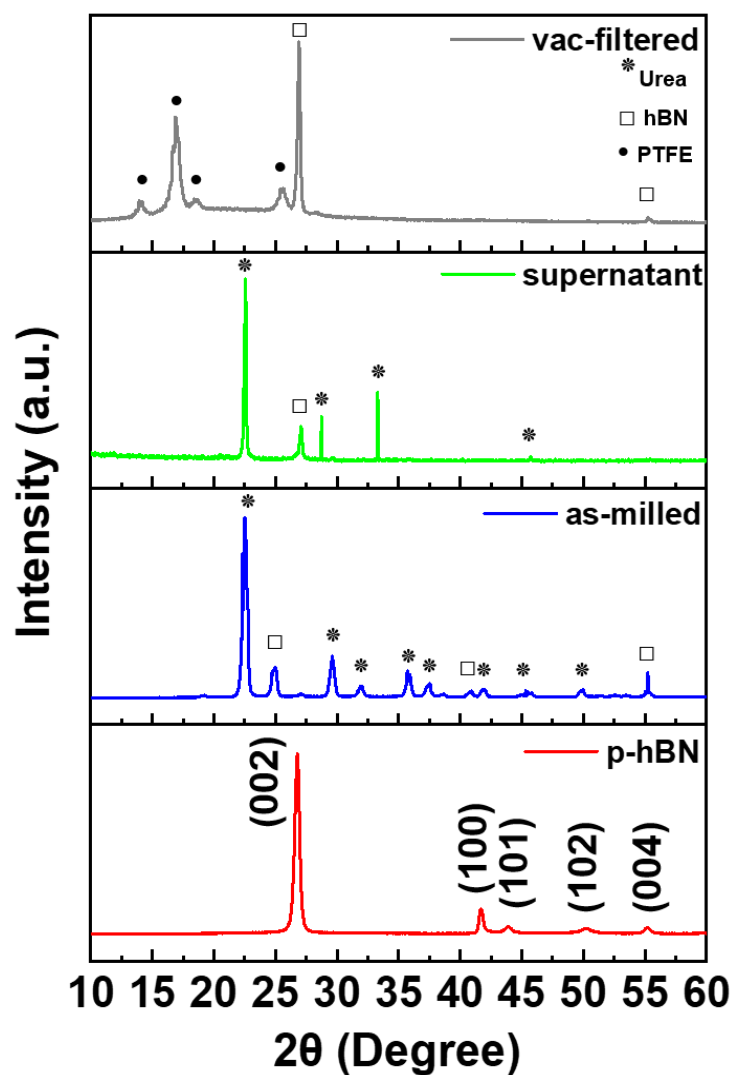
Figure 3.4. XRD patterns of pristine, milled and exfoliated h-BN.

In addition, the removal of urea was also demonstrated by the elemental analysis method, energy-dispersive X-ray spectroscopy (EDS). The equipment in our department can only identify carbon, but it cannot detect boron or nitrogen. Figure 3.5 shows EDS peaks of "Si" and "Au", since the sample was on the silicon wafer and was gold-coated. No carbon was detected as desired.

```
                                    Si
                                  Au




                                         Au
                               Au

    0.50   1.00   1.50   2.00   2.50   3.00   3.50   4.00   4.50   5.00   keV
EDAX ZAF Quantification (Standardless)
Element Normalized
SEC Table : Default

Element   Wt %    At %     Z        A        F
   SiK   87.03   97.92   1.0229   0.9028   1.0000
   AuM   12.97    2.08   0.7261   0.5812   1.0000
 Total  100.00  100.00
```
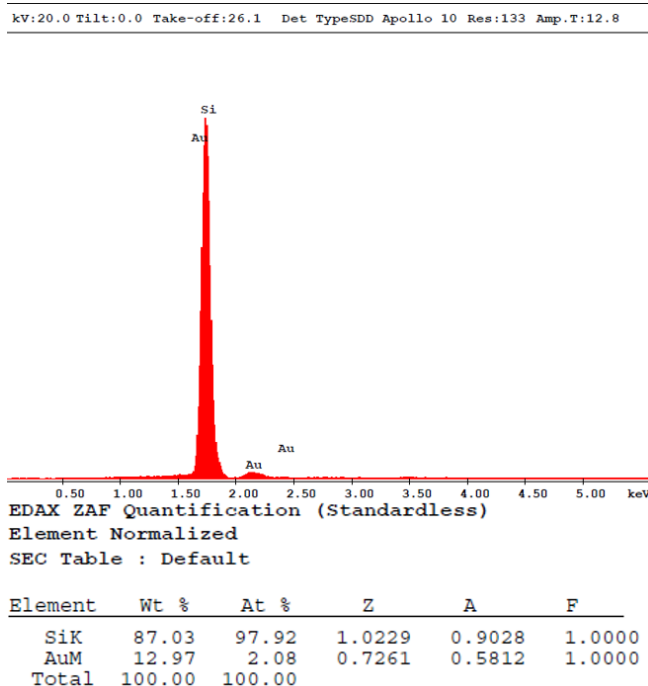
Figure 3.5. EDS analysis results to prove the complete removal of the urea.

SEM analysis was performed to compare the surface morphological structure of h-BN after exfoliation. As seen in Figure 3.6 (a) and (b), the pristine h-BN was in an agglomerated state. In addition, the size distribution in the structure was much wider than desired. h-BN was vacuum filtrated both before and after the exfoliation to analyze the uniformity in distribution and alignment. Agglomeration can be seen in the pristine h-BN as shown in Figure 3.6 (c). However, a uniform and single plane-like view can be seen for the exfoliated h-BN as shown in Figure 3.6 (d).

43
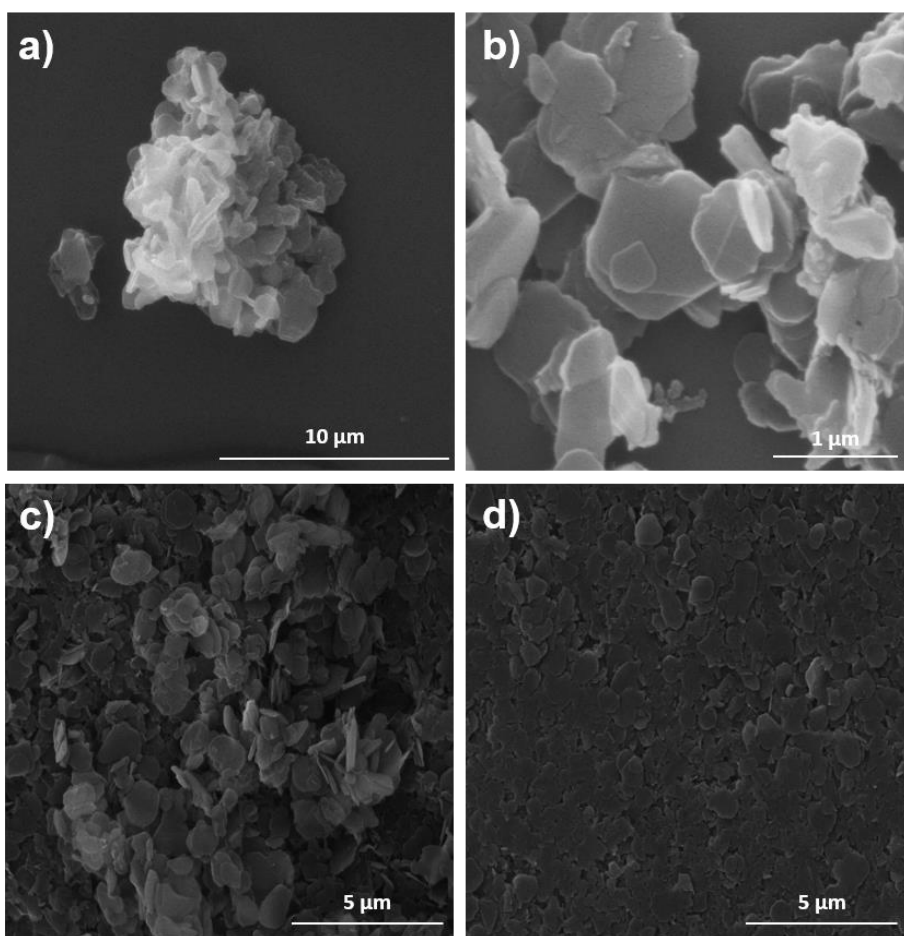
Figure 3.6. SEM images of the a), b) pristine h-BN, vacuum filtrated, c) pristine h-BN and d) exfoliated h-BN.

Tyndall effect can be used to monitor the stability of the h-BN solution with a reduced number of layers since laser beam appears even after 50 days (Figure 3.7 (a) and (b)). Suspended h-BN in the supernatant part can be seen throughout the entire as-exfoliated solution in this figure. This stability indicator proved the success of the exfoliation and the number of layers was greatly reduced.
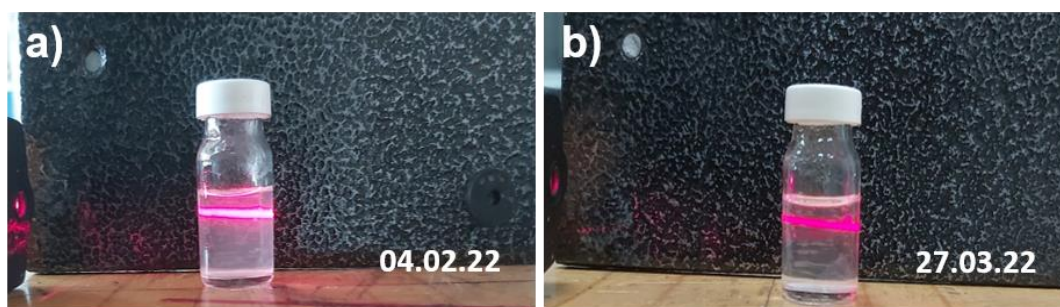
Figure 3.7. Photos showing the Tyndall effect on a) as-exfoliated h-BN and b) 50 days old exfoliated h-BN.

3.2.2 Shear Exfoliation

IPA was used as an exfoliation agent because its surface tension value matches better with h-BN than the other candidates like dimethylformamide (DMF) and N-Methyl-Pyrrolidone (NMP). Higher surface tension damages the h-BN flakes and cause a reduction in lateral size[76]. Therefore, IPA showed a better peeling effect and was preferred for this experiment.

The number of shear exfoliations and the days needed to wait to separate the exfoliated h-BN (supernatant) from the pristine one (precipitated) were decided by several experiments. The samples need to wait for 3 days to obtain the most efficient h-BN nanosheets, which is discussed in this chapter. After the first exfoliation step, the h-BN nanosheets amount in the supernatant that was waited for 3 days calculated by weighing the filter paper before and after the vacuum filtration was 0.010 g. Then, precipitated h-BN was recycled and the weight of exfoliated h-BN nanosheets were found as 0.071 g for this step. After the second recycling of h-BN, this amount was calculated as 0.173 g. After these calculations, it was decided that the h-BN nanosheets amount after the first shear exfoliation was negligible. Therefore, it was completely recycled after the first step. The sample was left to wait for three days following the second exfoliation. Then, the supernatant was collected. Finally, precipitated h-BN was also recycled for the last time and supernatant was collected after 3 days.

The stability test was also performed to compare the effect of the number of exfoliation cycles required to obtain h-BN nanosheets. Samples exfoliated on the same day, exfoliated for once, twice and thrice were poured into the bottles and left to wait for 30 days. A photo of those samples are provided in Figure 3.8. The milky view was found to increase from left to right, thus three times exfoliated h-BN showed the best stability and the best performance in reducing the number of layers.

Figure 3.8. Photo of shear exfoliated samples (sorted from left to right as for once, twice and three times).

After exfoliation, the surface morphologies of the h-BNs were compared using SEM analysis. SEM image of pristine h-BN is also provided (Figure 3.9 (a)) for comparison. Agglomerated, thick, and non-transparent h-BN layers were observed in the SEM image. However, agglomeration was found to decrease as the waiting time increases from 1 to 3 days (from Figure 3.9 (b) to (d)). The samples were taken from the upper part of the beaker to determine how many days to wait to obtain the most efficient h-BN. No significant difference was observed between Figure 3.9 (b) and (c). However, layers that have started to fold can be observed when looking at the sample left for 3 days following the exfoliation in Figure 3.9 (d). Furthermore, transparent layers and h-BN with clear hexagonal morphology can be seen in this image.
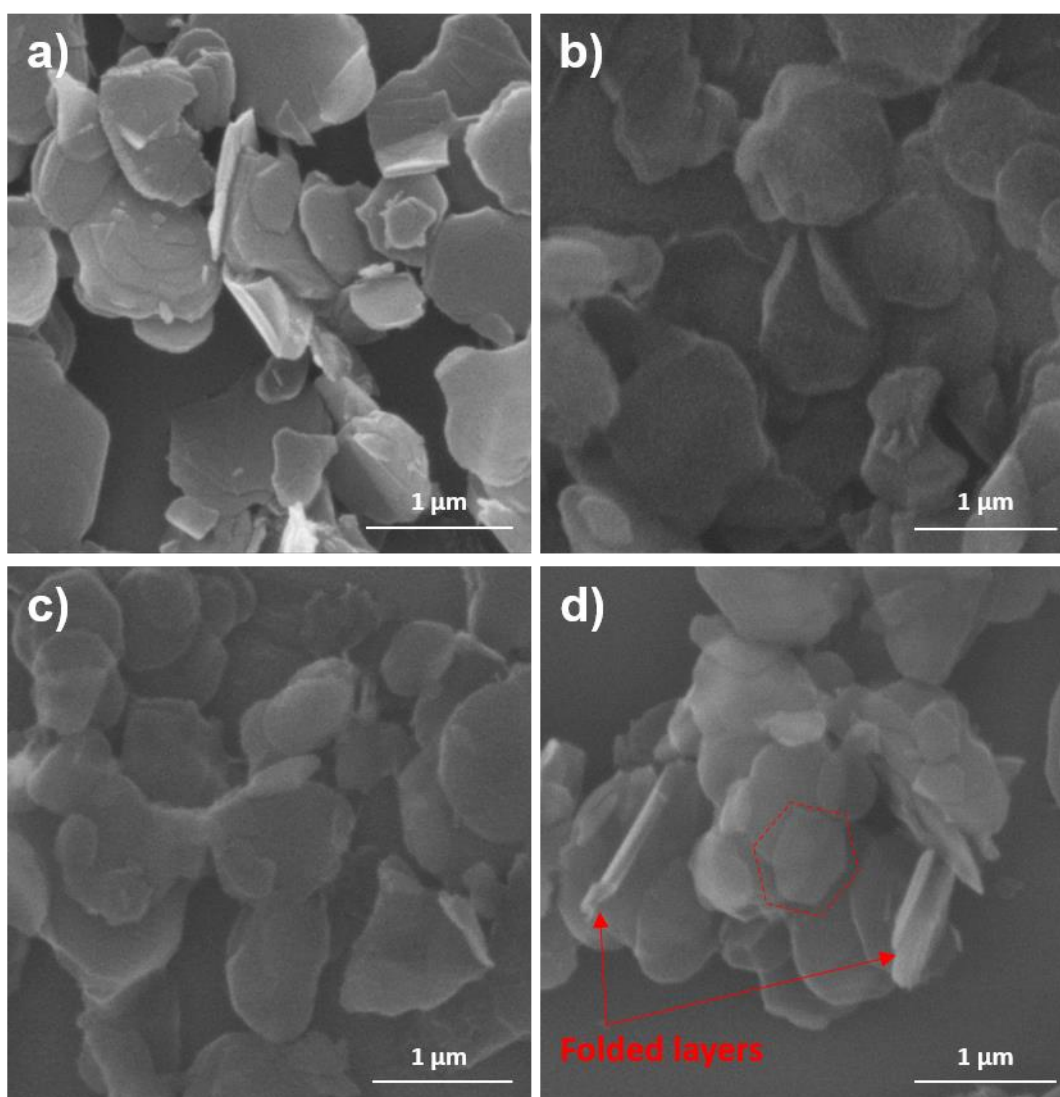
Figure 3.9. SEM images of a) pristine h-BN, b) 1 day waited exfoliated h-BN, c) 2 days waited exfoliated h-BN and d) 3 days waited exfoliated h-BN.

As it can be described in 4.2.1, h-BN has 5 characteristic XRD peaks and exfoliated h-BN nanosheets exhibit a notable decrease in structure pattern, showing thin layers of h-BN in the exfoliated sample and much-reduced structure in the c-direction[93]. Therefore, shear exfoliated h-BN also showed a similar change in the XRD pattern as it was in ball-milled case as can be seen in Figure 3.10 (a). Raman spectra for exfoliated/unexfoliated h-BN exhibit a characteristic peak due to the typical B-N stretching mode (E_{2g}). A shortening of the B-N bond is expected in a few-layer h-BN since the interaction between layers is weaker than its unexfoliated form[94]. A left

47

(red) shift was observed in few-layer h-BN, while a right (blue) shift attributed to the hardening of E_{2g} phonon mode was observed in monolayer due to slightly shorter B-N bonds[95,96]. As seen in Figure 3.10 (b), the E_{2g} peak of exfoliated h-BN showed a red shift confirming the reduction in the number of layers. Following exfoliation, the FWHM value for h-BN was calculated as 19.83 cm^{-1}, while this value was recorded as 19.14 cm^{-1} for the pristine h-BN. This change was mainly attributed to the reduction in the h-BN interlayer interactions.
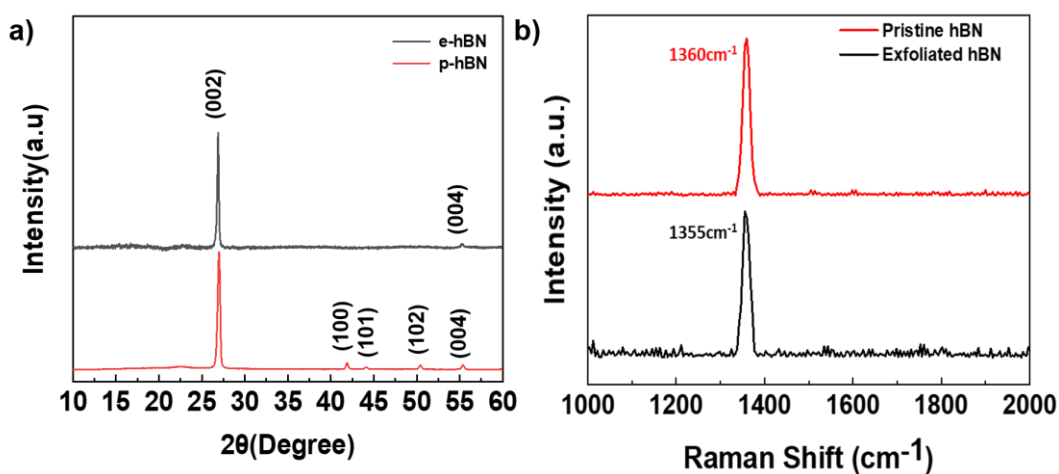
Figure 3.10. a) XRD pattern and b) Raman spectra for pristine and exfoliated h-BN.

TEM analysis was performed to show the reduction in the number of layers due to the exfoliation[97,98]. Electron transparent layers can be easily seen in Figure 3.11 (a) and (b). The dense region in Figure 3.11 (a) shows the fact that, despite agglomeration, each h-BN is aligned in a different direction. They are still exfoliated few layered h-BN nanosheets but are not homogeneously dispersed during sample preparation. Figure 3.11 (b) shows a TEM image of h-BN that can be directly interpreted as a single layer.
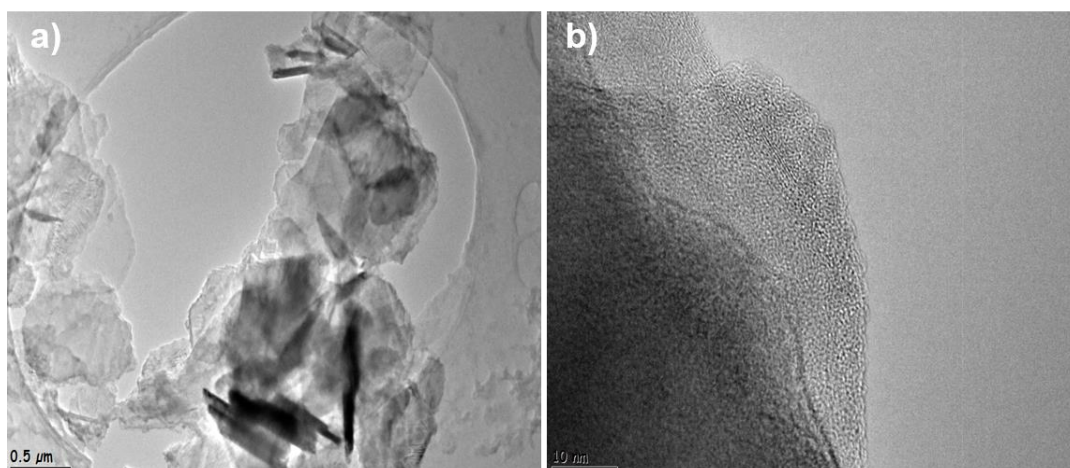
Figure 3.11. TEM images of exfoliated h-BN at a scale of a) 0.5 μm and b) 10 nm.

The interlayer spacing of the h-BN sample was calculated using the GATAN (GMS 3) software used to analyze TEM images. The result of this calculation process is shown step by step in Figure 3.12. It is reported as approximately 3.3 Å in the literature corresponding to (002) plane[99]. A region was selected from the high-resolution TEM (HRTEM) image shown in Figure 3.12 (a), and the IFFT (Inverse Fast Fourier Transform) image of this image, shown in Figure 3.12 (b), was generated. Here, the distance indicated by the blue line was graphed in the live profile of the IFFT shown in Figure 3.12 (c). The interlayer spacing was obtained by dividing the distance between several peaks to the number of peaks in between. The interlayer spacing was calculated as 3.278 Å, which was similar to the literature. This result evidenced the presence of mono/few-layer h-BN with (002) plane[100]. In addition, the zoomed-in HRTEM image provided as an inset in Figure 3.12 (b) also shows a unidirectional alignment of the representation of atoms that proves the presence of mono or few layered h-BN. Since this alignment shows there is just one plane (002) in this part.
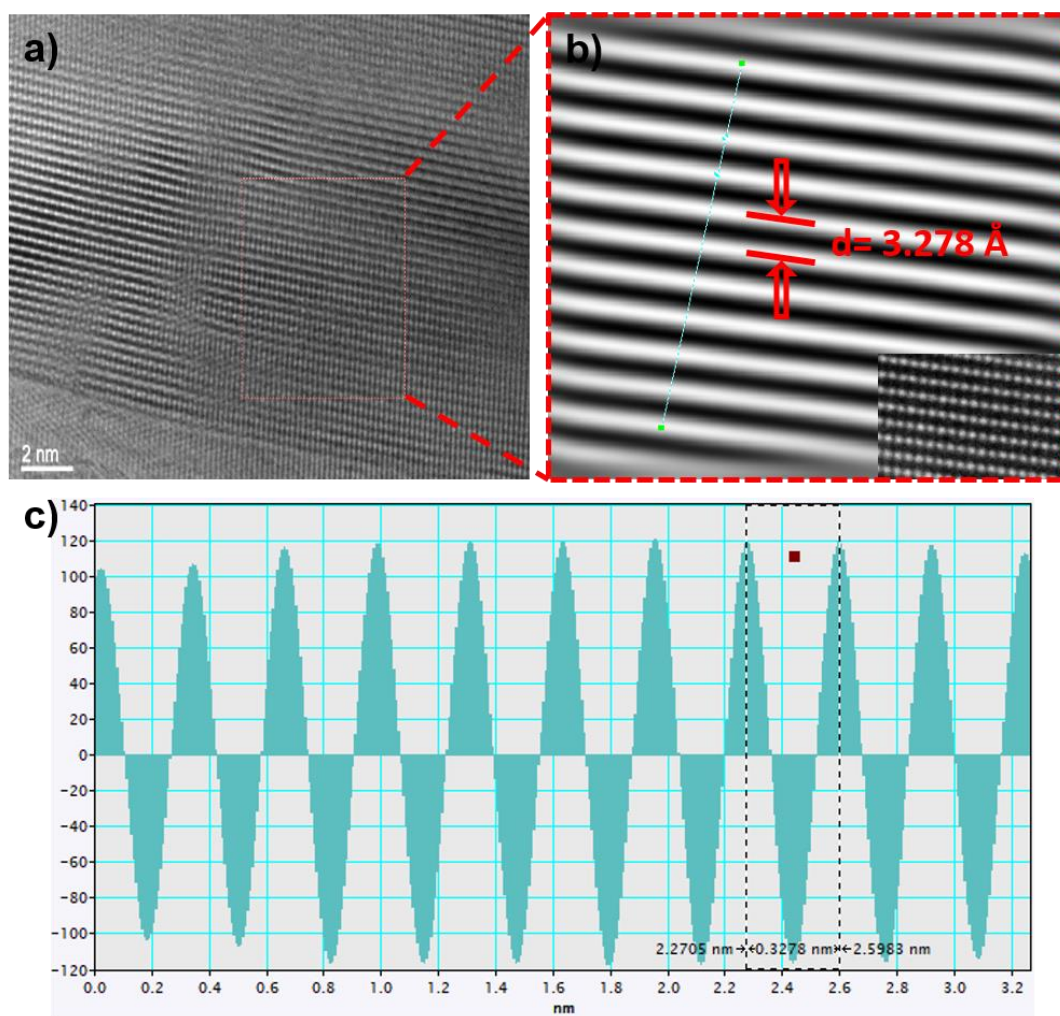
Figure 3.12. Exfoliated h-BN's a) HRTEM, b) interlayer spacing calculation process on HRTEM image, c) graphed version of the drawn line on HRTEM image.

Atomic force microscopy (AFM) with a picometer resolution, based on the interaction between the probe tip and the sample surface, is another preferred characterization method for determining the number of layers[101,102]. The reduction in the number of layers as a result of exfoliation of multi-layered h-BN was also monitored through AFM. As it was mentioned before, the thickness of a monolayer h-BN is 0.33 nm. AFM results from two different regions are shown in Figure 3.13 (a) and (b) and thickness values were extracted from these images using Nanoscope Analysis software. The results were 0.29 nm, 0.65 nm, 1.37 nm, and 1.95 nm which correspond to 1, 2, 4, and 6 layers, respectively. Wang et al. reported thickness values

of 1.8 nm and 2.3 nm corresponding to 6-7 layers of exfoliated h-BN using IPA and Li^{+} ions [76]. In a different study, Liu et al. reduced the thickness of h-BN by ball-milling to 3.5 nm. Although this number equates to about 10 layers, it was claimed that this value corresponds to 3–4 layers[95]. In this study, the thickness values were smaller than most of the values provided in the literature. However, it can be noticed that the lateral size of h-BN nanosheets were smaller than that observed in SEM images. The reason behind this size difference can be explained by the preparation method of AFM samples. The samples should be homogeneous and prepared from a dilute solution. This is required for the probe tip to get close to nanosheets on the surface. It was also possible that the small sized h-BN sheets stuck to the silicon wafer surface during spin coating, while larger sheets spread out of the silicon wafer surface. This situation has also been encountered in the literature[103].
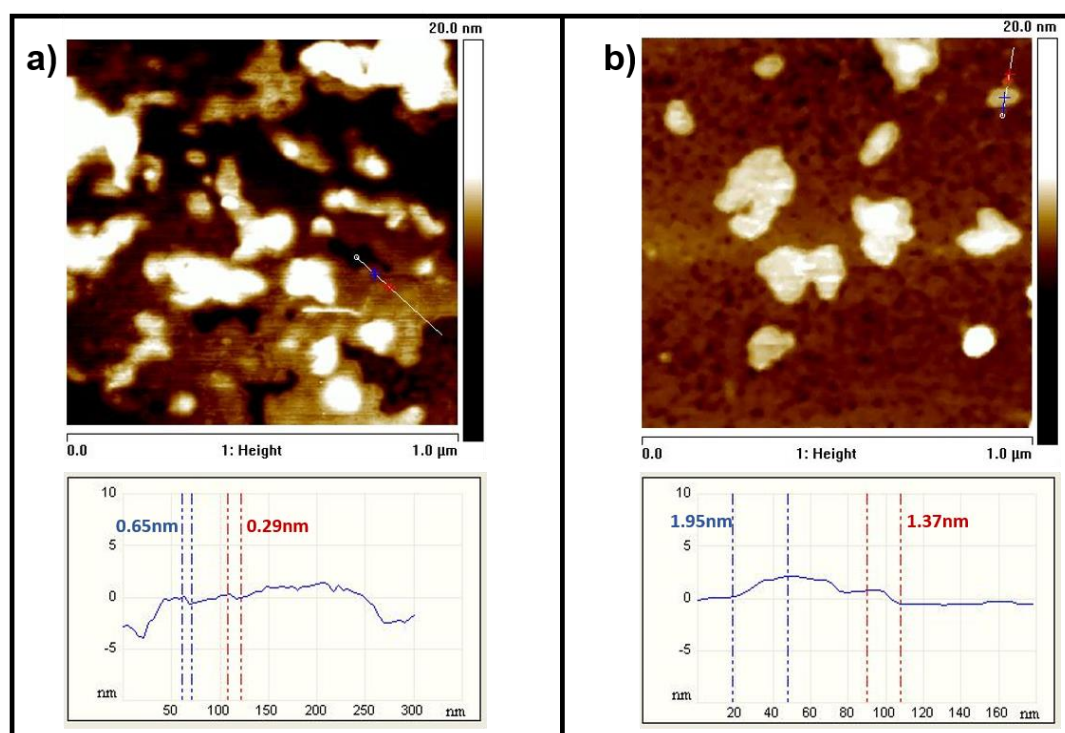
Figure 3.13. a), b) AFM images of exfoliated h-BN.

Exfoliated h-BN was produced with two methods as mentioned in this chapter. The yield of both methods were nearly the same; however, starting pristine h-BN amount for ball-milling was 0.33 g, while it was 2 g for shear exfoliation. Therefore, the

amount of total h-BN nanosheets obtained was much more for the shear exfoliation. The device operating part of this process is 4 hours for shear exfoliation and 20 hours for ball-milling. Shear exfoliation allows for a higher overall production rate of material per unit time. Large amounts of exfoliated h-BN nanosheets are required to produce a long filament. Therefore, production of h-BN nanosheets through shear exfoliation method is more reasonable compared to the ball-milling method.

CHAPTER 4

3D PRINTING OF h-BN/PLA NANOCOMPOSITES

4.1   Introduction

The morphologies and heat dissipation performances of exfoliated and pristine h-BN were compared as the first step in this chapter. Afterwards, the feeding method of the twin-screw extruder was investigated in detail. It was decided that the feed material would be in powder form as seen in Figure 4.1 (a). A filament with a diameter of 1.75 mm was produced and spooled as can be seen in Figure 4.1 (b) and (c) in the second step. The heat dissipation devices were produced in the third step. The heat sink and LED bulb holder devices were compared with the commercial products in the market. The production step and the 3D printed heat sink can be seen in Figure 4.1 (d) and (e).
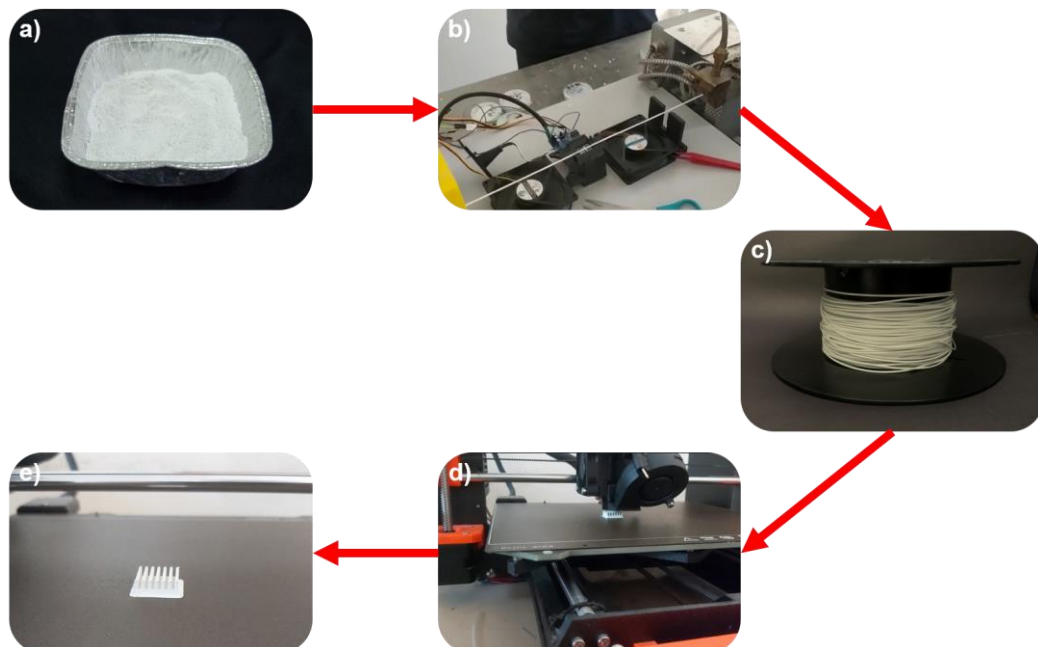
Figure 4.1. Photos of production steps of 3D printed h-BN/PLA as a) powder, b) filament winding, c) spooled-filament, d) 3D printing and e) 3D printed device.

4.2 Uniformity and heat dissipation performance comparison of pristine h-BN/PLA and exfoliated h-BN/PLA film

At the end of the exfoliation process, the exfoliated h-BN were mixed with PLA to compare the effect of this process on the heat dissipation property. Pristine h-BN was also used for comparison. While the mono/few-layered h-BN with the reduced number of layers formed a homogeneous solution in the chloroform medium, the pristine ones could not form a homogeneous mixture despite the use of temperature, high rpm with a magnetic stirrer, or sonication. This was due to the homogeneous size distribution and the difference in the number of layers between the two h-BN types (exfoliated and pristine). Afterwards, these two solutions continued to be mixed until they reach the honey consistency, and the excess chloroform was evaporated. Solutions were drawn on glass using a Dr. Blade and kept in a vacuum oven at 60 °C for one day. The produced films are shown in Figure 4.2. There was a visible homogeneity difference in the films as expected. Larger h-BNs that did not show uniform dispersion in solution did not show the desired distribution in PLA matrix (Figure 4.2 (a)). However, a homogeneous and single-color view can be seen in Figure 4.2 (d) for the exfoliated samples. Samples were prepared from the surface and a cross-section of both films and SEM analysis was performed. In the cross-sectional view of the pristine h-BN (Figure 4.2 (b)), it is clear that the h-BN aggregates stand apart from the surface. Their mixture with PLA was not homogeneous. However, when the exfoliated one is observed (Figure 4.2 (e)), a highly smooth surface image was encountered. In Figure 4.2 (c) and (f), surface images of pristine and exfoliated h-BN/PLA are compared. It is clear to see that there are agglomerated h-BN parts in the pristine one. However, exfoliated h-BN nanosheets were evenly distributed on the surface of the PLA matrix.
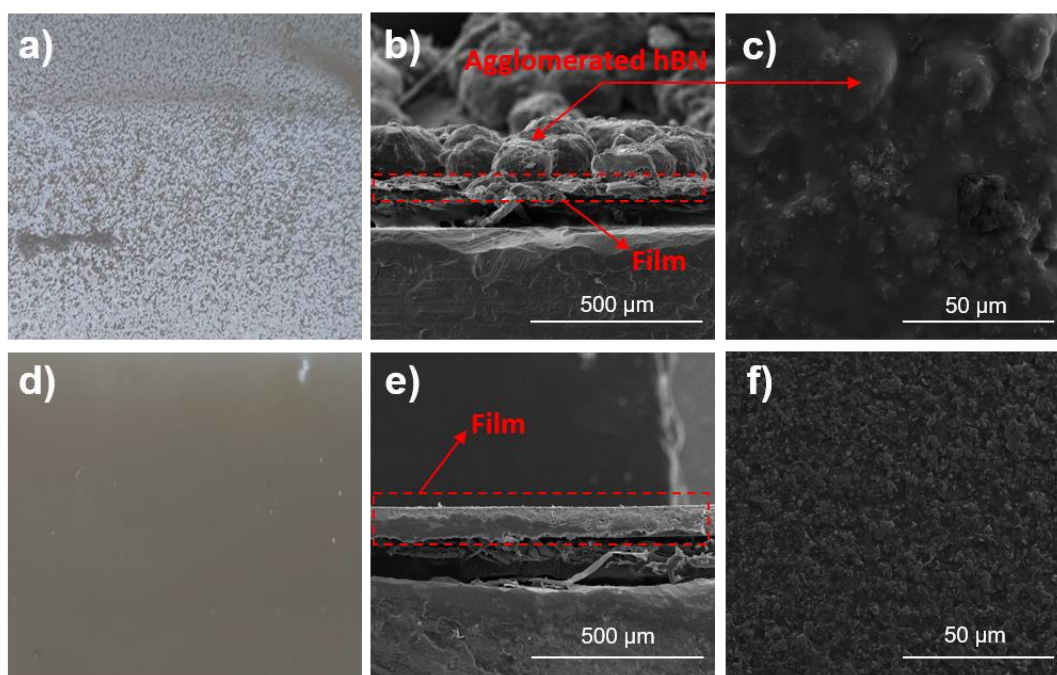
Figure 4.2. a) Photo, b) cross-section SEM image, c) surface SEM image of pristine h-BN/PLA film and d) photo, e) cross-section SEM image, f) surface SEM image of exfoliated h-BN/PLA.

In Figure 4.3 (a) and (b), the cross-sectional images of the exfoliated h-BN/PLA composite are shown. The h-BN nanosheets were evenly distributed over the sample. It was foreseen that the uniform placement in both in-plane and through-plane positions will contribute to the anisotropic heat distribution.
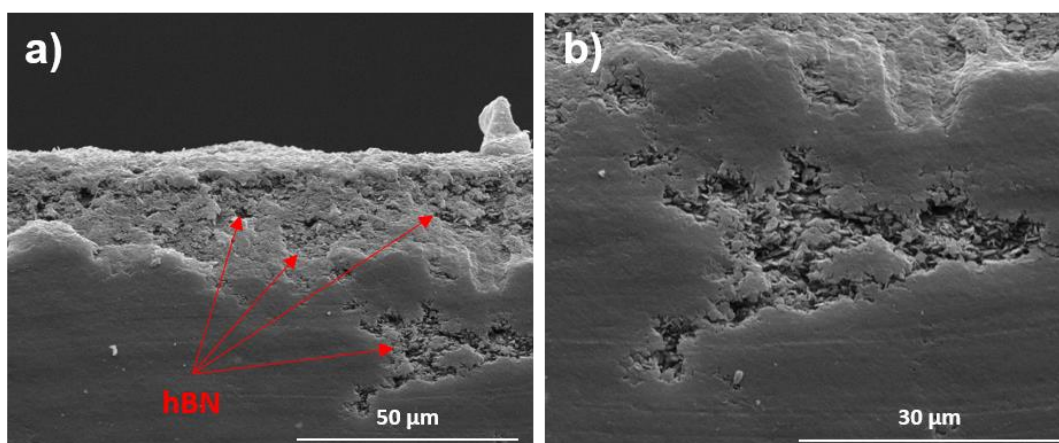
Figure 4.3. Cross-sectional SEM images of exfoliated h-BN/PLA film at scales of a) 50 and b) 30 µm.

The heat dissipation performance of the produced films was measured on the heated ITO-coated glass. The changes in temperature with time is provided in Figure 4.4. In the graph, exfoliated h-BN/PLA (black/the highest) represent the exfoliated, pristine h-BN/PLA (blue/the lowest) represent pristine composites, and the bare PLA (green/the middle) curve represents the bare PLA film. It is clear that the exfoliated composite performs much better than the others, demonstrating the benefits of exfoliation for heat dissipation. Furthermore, it has been found that composites containing pristine h-BN perform even worse than bare PLA although it has a very low heat conductivity. It was found that the homogeneous distribution of the filler material in the matrix is significantly important for heat dissipation performance. Furthermore, it is more critical than the type of the material used for this purpose. In addition, when all three samples reached their maximum temperature, it was observed that the exfoliated h-BN composite had a temperature 5.3 °C higher than PLA and 4.7 °C higher than the pristine h-BN composite. Although the films were very thin, this difference is important in increasing the effective life of the electronic devices.
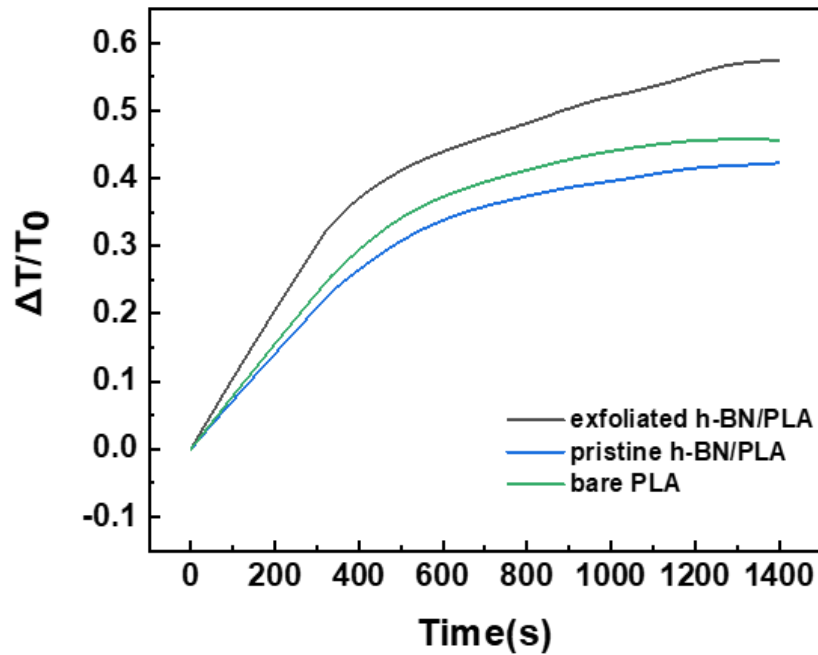
Figure 4.4. Temperature change over the initial temperature with a time graph for exfoliated h-BN/PLA (the highest), pristine h-BN/PLA (the middle), and the bare PLA (the lowest) films.

4.3 Material loss and morphology comparison for concentration, shape, and exfoliation status change of h-BN/PLA composite

4.3.1 Material loss comparison by TGA

It is known that material loss can be seen after the use of the twin-screw extruder[104]. The amount of h-BN was calculated following the filament production step using TGA between 30 – 550 °C (with an increase rate of 10 °C/min). First, pristine-h-BN/PLA composite was produced in powder, sheet, and rod forms as shown in Figure 4.5 (a) respectively. TGA was used to monitor the changes in the weight of filler loss for mentioned morphologies. In this comparison, starting h-BN amount was 55.15 wt.% (40 vol.%) so there was h-BN loss for all forms, as can be seen in Figure 4.5 (b). It was decided to produce it in powder form since the most loss occurs in the form of rods and the least amount of loss occurs in the powder feeding process.
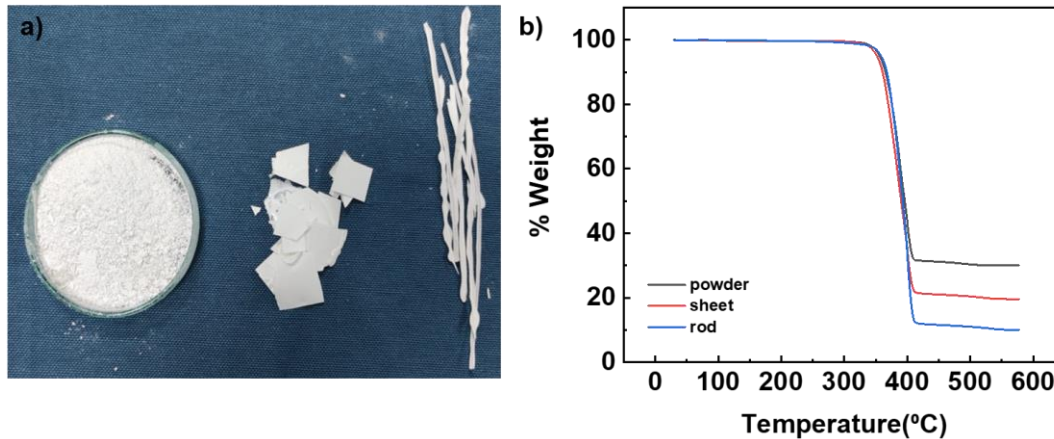
Figure 4.5. a) Photos of h-BN/PLA composite produced in powder, sheet, and rod shape. b) TGA plot showing the material loss in powder (the highest), sheet (the middle) rod (the lowest) form.

After the feeding shape decision as a powder, pristine-hBN/PLA composites containing 20 vol.%, 30 vol.%, and 40 vol.% h-BN were also produced to determine the amount h-BN that was lost and that in the composites. TGA was performed following the samples leave the filament winding device. As can be seen in Figure 4.6 (a), the percentage of loss increases as the amount of h-BN decreases, so the amount was decided as 40 vol. %. h-BN.

A final comparison with TGA was made between the bare PLA, pristine h-BN/PLA, and exfoliated h-BN/PLA to show the exfoliation effect on material loss. As it can be seen in Figure 4.6 (b), a negligible amount of PLA left after the bare PLA sample was heated above 400 °C. It can be stated that the amount of remaining material can be dictated as h-BN amount for composite samples. In the pristine h-BN sample, 44.10 wt.% h-BN was left so there was a loss of 11.05 wt.%. However, there was 54.15 wt.% h-BN left in the exfoliated h-BN sample so the loss amount was just 1 wt.%. This result also supported the observed uniformity differences as discussed in Chapter 5.1 between the exfoliated and pristine samples. It can be said that uniform dispersion of h-BN provides more collapsing of filler material in the matrix. However, agglomerated h-BN was stood apart rather than forming a uniform mixture. Therefore, the amount of stuck material to the inner surface of the twin-screw extruder for exfoliated h-BN was less than that for the pristine one.

58
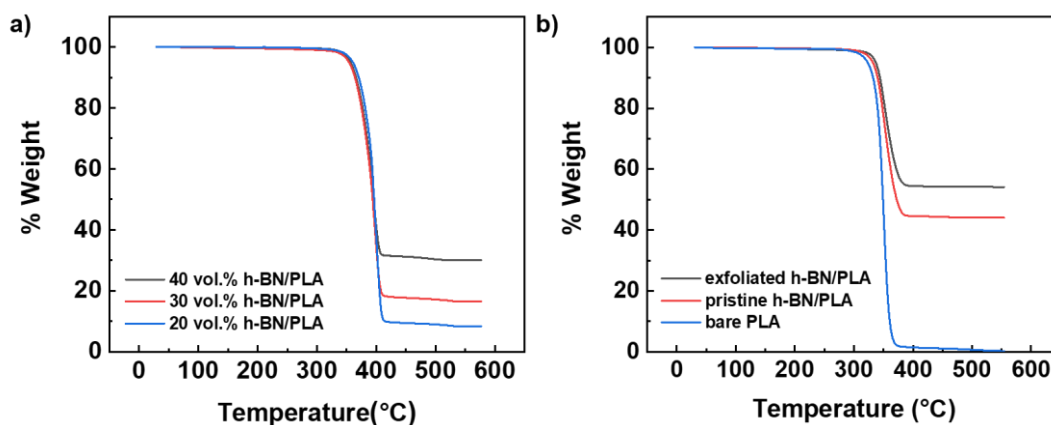
Figure 4.6. TGA plots for a) 20 vol.% (the lowest), 30 vol.% (the middle) and 40 vol.% (the highest) h-BN filled PLA, b) bare PLA (the lowest), pristine h-BN/PLA (the middle), and exfoliated h-BN/PLA (the highest).

4.3.2   Morphology comparison by SEM

Structural uniformity and homogeneous dispersion of filler material within the matrix are very important parameters for composite structures as it was mentioned before. Filaments produced with pristine and exfoliated h-BN fillers were analyzed by SEM to criticize whether exfoliation has an effect on dispersion in filament structure or not. Cross-sectional, surface, and the cleaved part of the filament morphology's SEM images can be seen for pristine-h-BN/PLA in Figure 4.7 (a) - (c), and for exfoliated h-BN/PLA in Figure 4.7 (d)- (f) respectively. First, exfoliated h-BN results in a smoother surface than the pristine one as can be seen clearly from the cross-sectional images. Moreover, the dispersion of exfoliated h-BN within the filament was much better than that of the pristine one. Secondly, the exfoliated h-BN filled filament had a much uniform diameter compared to the pristine h-BN added filament. Finally, when the cleaved parts of the filaments were compared, it was clear that h-BN agglomerated in only one region for the pristine one. However, the distribution of h-BN nanosheets was uniform in all regions for the exfoliated one.

59
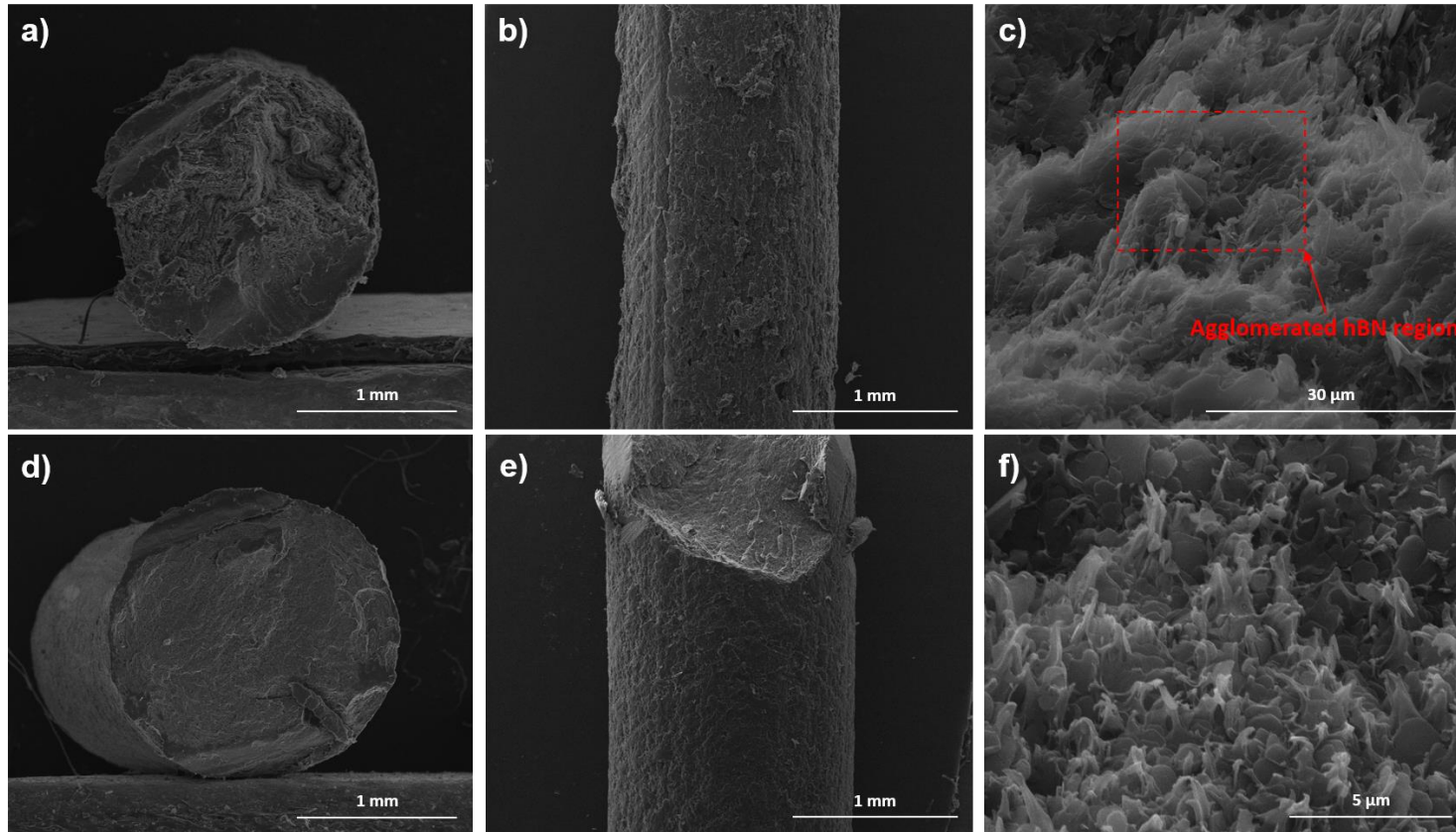
Figure 4.7. SEM images of a) cross-section, b) surface, and c) cleaved part of pristine h-BN/PLA filament. d) Cross-section, e) surface, and f) cleaved part of exfoliated h-BN/PLA filament.

In addition to these images, two more high resolution cross-sectional SEM images are provided below for exfoliated h-BN/PLA nanocomposite filaments (Figure 4.8 (a) and (b)). Lots of uniformly distributed h-BN nanosheets were observed within the PLA matrix. In addition, hexagonal shape of h-BN nanosheets can be seen quite clearly in Figure 4.8 (b).
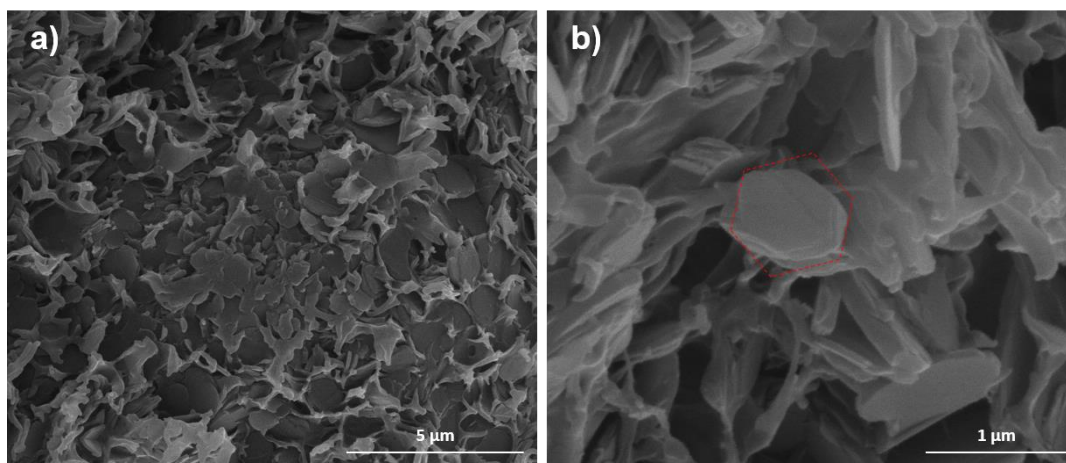
Figure 4.8. High resolution cross-sectional SEM images of exfoliated h-BN/PLA filament at a) 5 and b) 1 μm scale.

4.4   3D Printing of h-BN/PLA nanocomposite

4.4.1   Thermal conductivity measurement

Thermal conductivities of 3D printed bare PLA, 2, 5, 10, 20, 30 and 40 vol. % h-BN/PLA samples were calculated using the following Equation 1.

$$Thermal\ Conductivity\ (W/m.K) = k\ (mm^2/sec)\ x\ C_P\ (J/g.K)\ x\ \rho\ (g/cm^3)\ (Equation\ 1)$$

The results of this measurement were provided in Figure 4.9. The bare PLA had through-plane thermal conductivity value of 0.17 W/m.K. These values are 0.21,

0.24, 0.30, 0.49, 0.59 and 0.85 W/m.K for 2, 5, 10, 20, 30 and 40 vol.% h-BN/PLA samples respectively.
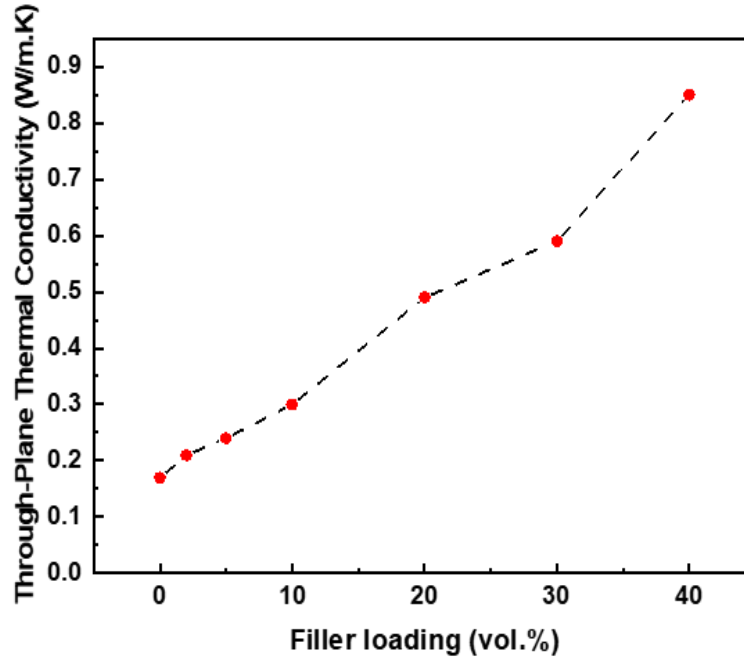
Figure 4.9. Through-plane thermal conductivity results for different loading percentages of h-BN. Dashed line is for visual aid.

The thermal conductivity value of 3D printed PLA was increased by 5 times by adding 40 vol.% of h-BN. The value was increased with the amount of h-BN. The value showed a continuous increase so it can be said that thermal conductivity was not yet saturated. However, the loading cannot be increased more than 40 vol.% to keep the mechanical integrity of the filament structure in the 3D printable range. Therefore, the h-BN amount was kept at 40 vol. % for 3D printing of thermal management devices.

4.4.2   Heat sink application

The integration and downsizing of electronic devices have resulted in heat dissipation issues that have raised the demand for thermal management materials in recent years[72,105]. For example, on some recent processor modules or integrated

circuits, the power required for high-performance computing applications may exceed formation of 200-250 W. The smaller and faster components of electronic devices produce more heat than the older versions. Thermal challenges like hotspot have to be solved to use the effectiveness of miniaturized and faster electronics without limitations (reduce in speed, reliability, and lifetime)[106,107]. Typically, heat removal is accomplished through the use of thermal management devices including heat exchangers, cold plates, heat spreaders, and heat sinks in particular. These thermal management devices are generally produced from metals like aluminum and copper due to their high thermal conductivities, which are around 200 W/m.K and 400 W/m.K, respectively. However, their high electrical conductivity creates safety issues in these areas of use[108]. Moreover, the high cost and weight of these materials limit their effectiveness. PLA, like other polymers, can offer a solution to some of these problems by being light, electrically insulating, and economically viable. However, the thermal conductivity of PLA is not suitable for thermal management of electronic devices as mentioned in the previous chapters. The nanocomposite structure is produced by a 3D printer using h-BN nanosheets as fillers and PLA as a matrix. This structure suggests a thermally conductive yet electrically insulative device for heat sink models. In addition to these properties, the 3D printing as a production method can produce various shapes and designs more easily than the conventional methods.

The heat dissipation performances of 3D printed h-BN/PLA nanocomposites, bare PLA heat sinks, and commercial aluminum heat sink were compared in the setup as shown in experimental details. The aluminum heat sink was chosen as a colorful type to be visible under the thermal camera. The thermally conductive tape was used between the semi-conductor plate and the heat sink to minimize the gap between the surfaces of these two objects. The three heat sinks were analyzed on the same day one after another to minimize the environmental effects such as moisture and temperature. The thermal camera images of the three heat sinks are provided in Figure 4.10. All samples were started at the same temperature and heated for the same duration for comparison. The 3D printed bare PLA sample was clearly visible

63

even at 120 seconds. However, the visibility disappeared slowly for the h-BN/PLA sample. Al heat sink showed the best visual similarity with the heated plate. It means that 3D printed h-BN/PLA and the Al sample could transfer heat from the heater to the top part of the heat sinks more effectively than the bare PLA. Similar colors on the surface of the heat sinks proved similar performance for the h-BN/PLA and Al sample, which was much better than that of bare PLA.
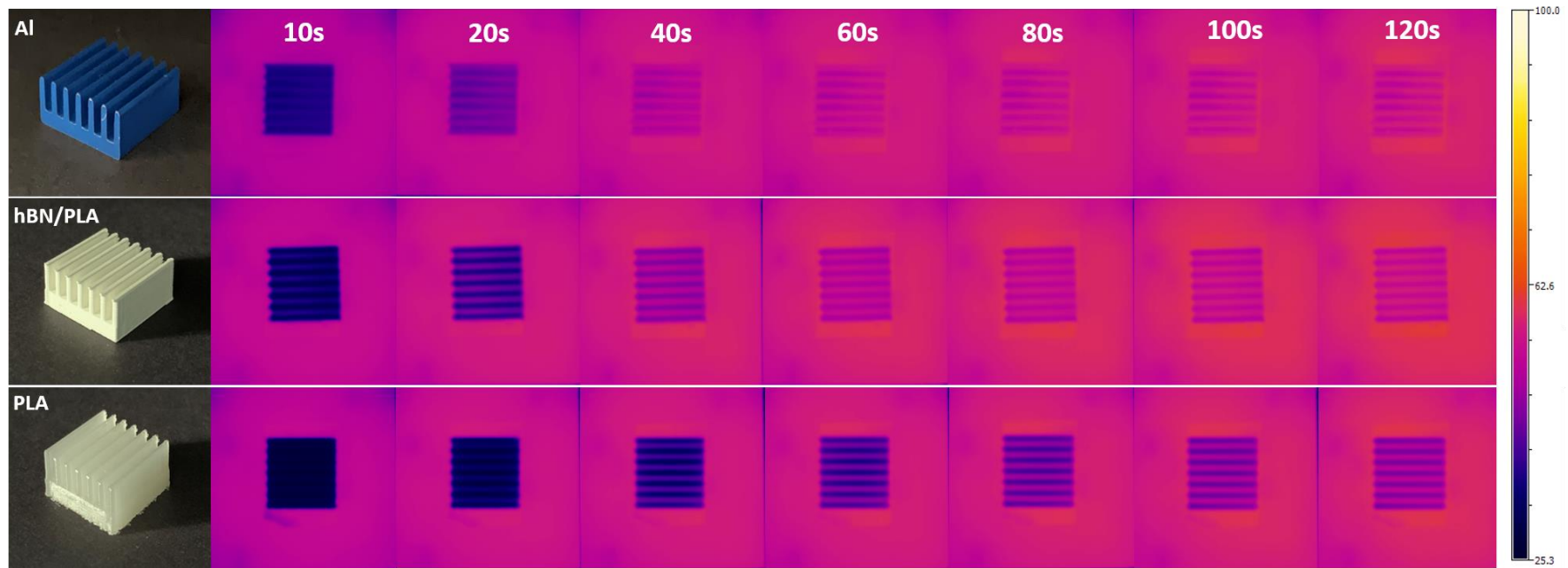
Figure 4.10. Photos and thermal camera images of a commercial Al heat sink and heat sinks fabricated from 3D printed h-BN/PLA and bare PLA.

The changes in temperature with time is plotted and provided in Figure 4.11. The semi-conductor heater plate reached around 60 °C after 120 seconds. The Al, h-BN/PLA, and PLA heat sinks reached 55.2 °C, 53.8 °C, and 47.5 °C, respectively. The h-BN/PLA sample showed a similar performance with Al. This result demonstrated the qualified heat dissipation performance of the fabricated nanocomposite sample. The 3D printed samples had the same size as Al heat sink in every way so that the convection coefficient differences between the materials were minimized. Although Al had a much higher thermal conductivity than the h-BN/PLA sample, the difference between the maximum temperature reached was low, probably due to the fact that the experiment was not conducted in a closed environment.
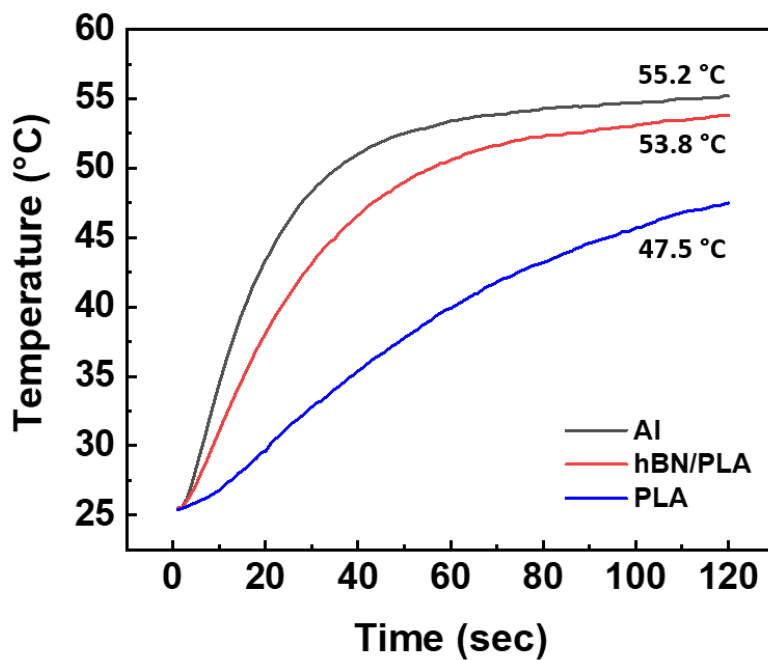
Figure 4.11. Change in temperature with time for Al, h-BN/PLA, and bare PLA heat sinks on the heater.

The first derivative (dT/dt) of Figure 4.11 enables us to determine the rate of temperature increase, which is provided in Figure 4.12. The rates were determined as 1.25, 0.8 and 0.25 (°C/sec) for Al, h-BN/PLA and bare PLA. It can be said that

the rate of temperature increase of PLA was enhanced by 320% by the h-BN addition.
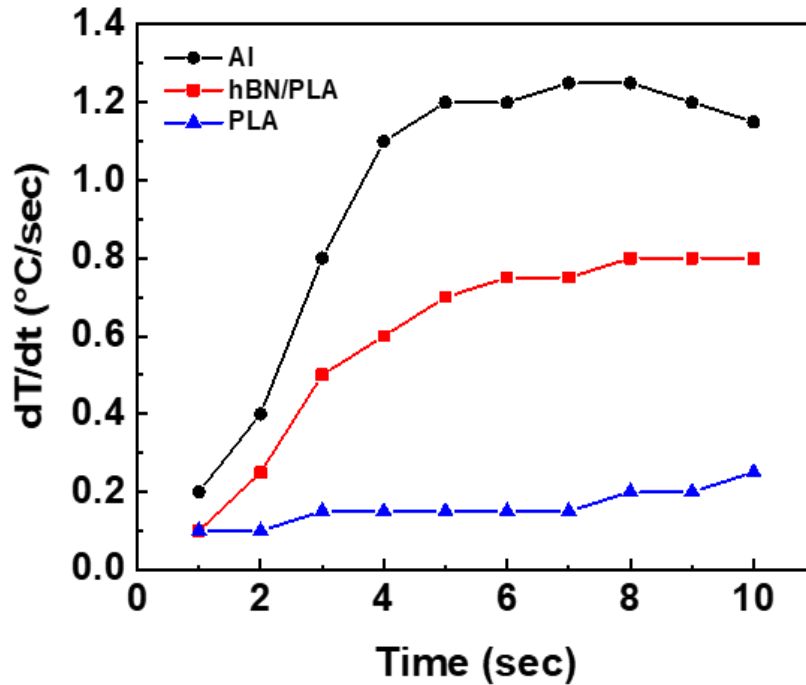
Figure 4.12. The first derivate graph of temperature with respect to time.

The shape uniformity and dissipation performance of the three heat sinks were also compared. Thermal camera images and corresponding line profiles with temperatures are provided in Figure 4.13. The first conclusion from this graph is that the top and bottom height levels of all peaks were almost the same, so the uniformity of all three heat sinks was sufficient. If the distance between the start-end point and the middle part of the lines was small, it can be said that the heat dissipation performance of that heat sink was successful. The difference was smallest for Al heat sink, h-BN/PLA was slightly higher, whereas bare PLA had the largest distance difference between them.
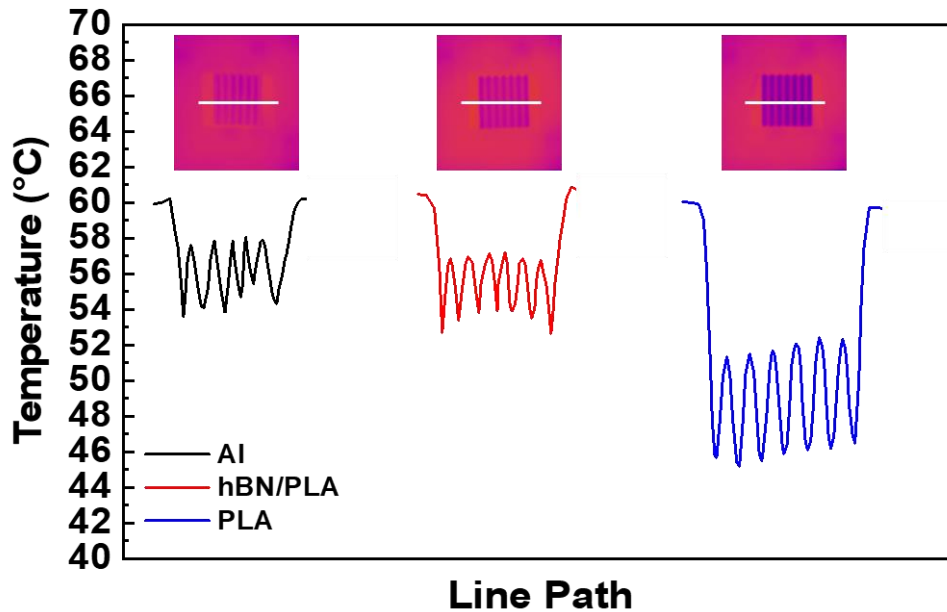
Figure 4.13. The uniformity and heat dissipation performance comparison for Al, h-BN/PLA, and PLA heat sinks.

The temperature distribution of the heat sinks was also investigated from their surface. Temperature uniformity is a crucial parameter for thermal management. Figure 4.14 shows the percentage temperature distribution of Al, h-BN/PLA, and bare PLA heat sinks collected from the marked square area. The temperature variation should be low to prove the best uniformity. In addition, one of the measured values must have a much higher percentage than the others for this purpose. Al heat sink had four different temperature values and the highest percentage was 45.3 % (Figure 4.14 (a)). However, the h-BN/PLA heat sink had three different temperature values and the highest percentage was 49.7 % (Figure 4.14 (b)). The bare PLA heat sink showed five different temperature values and the highest percentage was only 33.3% (Figure 4.14 (c)). These results showed that h-BN/PLA sample had better uniformity than both bare PLA and commercial Al heat sink which is crucial for thermal management applications.

68
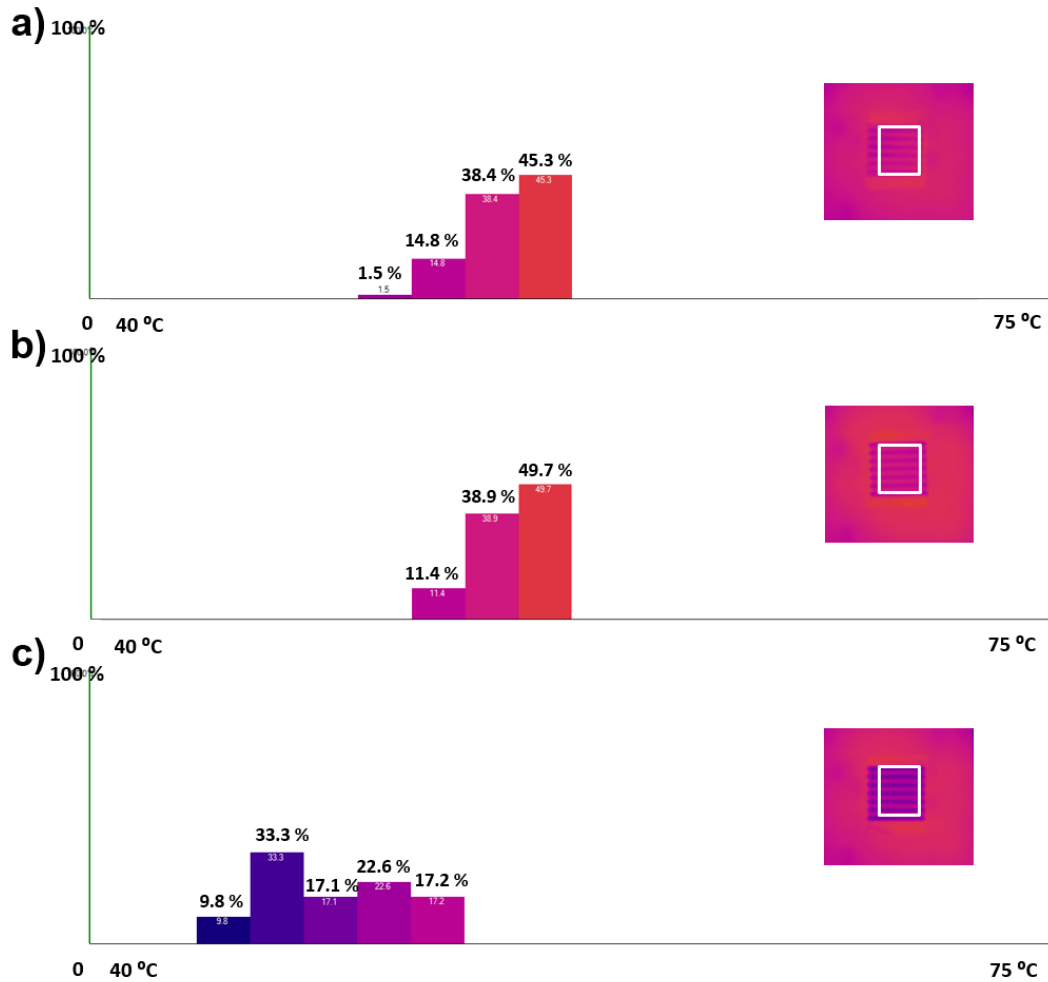
Figure 4.14. Percentage temperature distribution graphs for a) Al, b) h-BN/PLA and c) bare PLA heat sink.

4.4.3 LED Bulb Holder Application

Halogen lamps and incandescent bulbs use tungsten filament wire that must be heated to emit light. In these types of lamps, the wire is heated more to increase the brightness of the light. Unlike these types, LED bulbs produce light with semiconductor diode technology, and the amount of light power is measured in lumens, or luminous flux, rather than in watts, or energy consumption. LED bulbs start losing performance (decreased lumen values) due to increased heat even if they include refrigerant[109]. Wang et al. stated that every 10 °C increase in the internal

temperature of the bulb reduces the reliability of the product in terms of performance by 50%[110]. An experiment carried out at the American Light Research Center was described in another research. In this experiment, it was shown that LEDs have a lifespan of 40000 hours at 40 °C, but when the temperature rises to 50 °C, the lifespan is reduced to 20000 hours[111]. The effect of temperature on LED lifetime and brightness can be seen in the graphics given in Figure 4.15 (a) and (b)[112,113]. Figure 4.15 (a) shows the response of the light output value of the LED to the temperature increase for the lights of green, white, cyan, blue, and royal blue sorting from bottom to up at 120 °C respectively. Figure 4.15 (b) shows the changes in LED lifetime with respect to temperature. The effect of temperature on the effective life of LEDs is clearly visible in both graphs, and this has undeniably increased the demand for innovation in terms of energy consumption, green world goal, and economy.
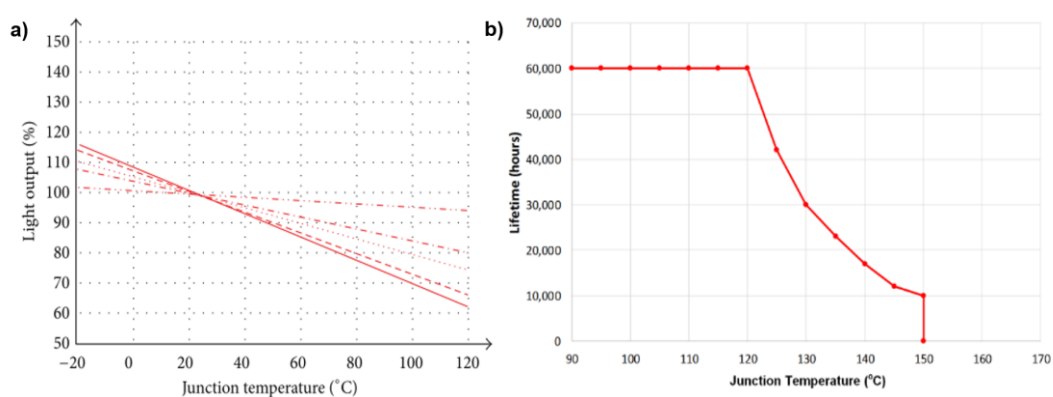
Figure 4.15. a) Light output (%) for green, white, cyan, blue, and royal blue lights from bottom to up at 120 °C respectively[112], b) lifetime (hours)[113] LED bulbs with respect to junction temperature.

The nanocomposite h-BN/PLA filament was used to produce an alternative LED bulb holder. The average LED temperatures of 3D printed bare PLA, h-BN/PLA, and commercial LED bulb holder assembled with the socket and the LED chips using thermal paste are shown via the thermal camera software in Figure 4.16. The lowest temperature of 120.8 °C was observed on the h-BN/PLA sample. The commercial sample showed an average temperature of 122.1 °C, which was slightly higher than that of h-BN/PLA. The bare PLA sample showed the highest average temperature of 136.4 °C.

70
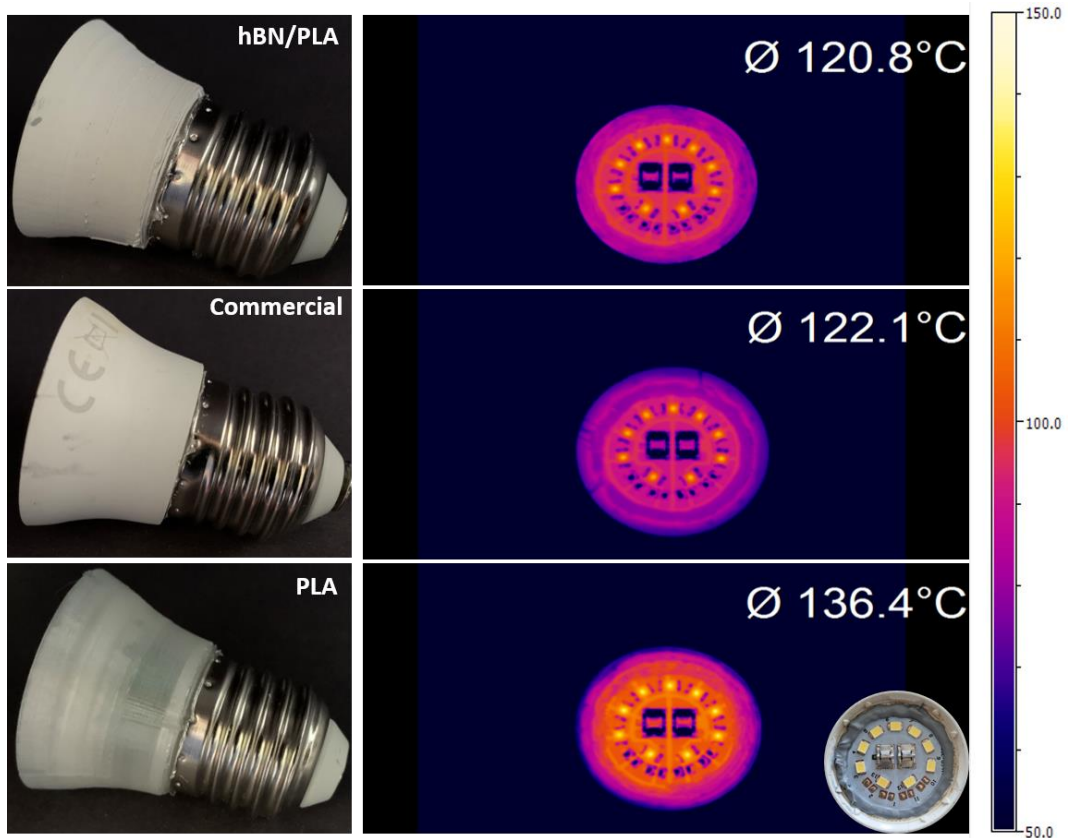
Figure 4.16. LED temperature comparison under thermal camera for 3D printed h-BN/PLA, commercial and 3D printed PLA LED bulb holders.

The 20-minute data was graphically drawn (Figure 4.17) to show the comparison of both the 600 seconds of heating and 600 seconds of cooling performance of LED bulbs with the 3D printed holders. The plug was inserted where the temperature increased. In the part where the temperature dropped, the plug was removed from the socket. The commercial and 3D printed h-BN/PLA samples showed nearly similar performances and are shown as a single line in the figure. However, the 3D printed PLA sample clearly had a different response in both the heating and cooling sections.
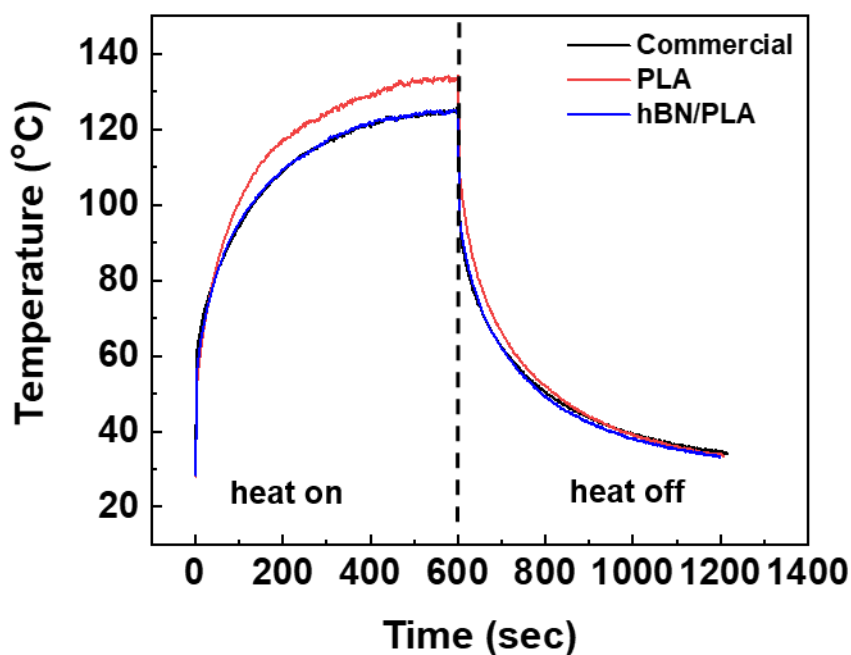
Figure 4.17. Temperature changes of 3D printed h-BN/PLA, commercial, and 3D printed PLA LED bulb holders in place during heating and cooling.

The voids and pores act as an obstacle to the conduction path of heat. 3D printed samples have porous structures due to the layer by layer production. Jia et al. compared the injection molded and 3D printed graphite-filled nanocomposite[114]. The injection molded sample showed a thermal conductivity of more than twice that of 3D printed at all graphite contents. The fabricated products include a lower number of pores than 3D printed samples. In this work, 3D printed h-BN/PLA sample showed slightly better performance than the fabricated sample even under these porosity conditions.

72

CHAPTER 5

CONCLUSIONS AND FURTHER RECOMMENDATIONS

5.1 Conclusions

In this study, pristine h-BN was exfoliated with both ball-milling and shear exfoliation. Although the yields of these two methods were similar, the recycled shear exfoliation method was preferred because it allows processing of higher amounts of material in a much shorter time. Exfoliation conditions were analyzed with SEM and sedimentation test. The optimum number of shear exfoliation cycles, speed, and duration were determined by these analyzes. The waiting time to collect the exfoliated samples was also investigated with layer quality in the manner of transparency and size distribution by SEM. The exfoliation efficiency was analyzed with XRD and Raman spectroscopy. The reduced structure in the c-direction and the weakened interaction between the layers were shown with these characterizations. Moreover, the transparency and the number of layers were investigated with TEM and AFM analysis. The calculated interlayer spacing value indicated that the (002) plane was undamaged for the transparent layers observed in TEM. The existence of a few-layer h-BN was also demonstrated using AFM analysis, and h-BN nanosheets with less than 10 layers were identified.

The pristine and exfoliated h-BN nanosheets were mixed with PLA by solution mixing technique and films-shaped structures were produced using a Dr. Blade. It is the only way to obtain uniform dispersion of h-BN in the PLA matrix. Therefore, it is difficult to use this composite for large-scale production. The effect of exfoliation on uniformity was analyzed through SEM analysis. The results showed agglomerations in pristine h-BN/PLA films; while nanosheets were uniformly distributed within the PLA matrix upon exfoliation. The heat transfer performances were also analyzed by thermocouples. Results showed that pristine h-BN acts as an

obstacle instead of creating heat conduction paths and it showed worse performance than bare PLA. The exfoliated h-BN/PLA film showed much better performance compared to both pristine-h-BN/PLA and bare PLA. The comparison of uniformity was also made between pristine and exfoliated h-BN in terms of filament shape. The results were consistent with the film-shaped case and h-BN agglomerations were observed. Moreover, the filament shape was more uniform when exfoliated h-BN was used compared to use of the pristine one.

A new filament winding machine has been developed that allows filament production with negligible thickness changes, due to the fact that the required filament thickness for 3D printers cannot be produced homogeneously with only twin-screw extruders. The twin-screw extruder was fed with different morphologies. They were powder, sheet, and rod, and results showed that the minimum material loss was obtained with the powder form. The optimization was made by calculating the amount of material loss by TGA. In addition, the material loss comparison was also made for the effect of h-BN loading in the matrix. The results showed that the percentage of loss increases as the amount of added filler material decreases. Besides that, the loss comparison was made between the pristine and the exfoliated one, and it was proved that uniformity affects the material loss. The agglomerated and non-uniform h-BN tends to stick to the inner walls of the twin-screw extruder compared to its uniformly dispersed and exfoliated counterpart. The thermal conductivity measurements were made to show the effect of h-BN addition. Bare PLA's conductivity was enhanced by 500% with the addition of 40 vol. % h-BN. Although the saturation point was not reached, the percentage could not be increased to be able to 3D print the h-BN/PLA composite. Otherwise, the structure of the filament will be brittle and cannot not be reshaped. Moreover, 40 vol. % filler included composites can only be used for 3D printing to produce complex shapes. Therefore, it will not be feasible for large-scale production.

A heat sink model was 3D printed with exfoliated h-BN/PLA filament. Bare PLA filament was also printed for comparison. Printed heat sinks heat dissipation performance and heating uniformity was investigated using a thermal camera and

results were compared to those of a commercial Al heat sink of the same dimensions. The results revealed similar performance for the Al and 3D printed h-BN/PLA heat sink and these heat sinks were significantly more efficient in terms of heat dissipation compared to bare PLA. The rate of temperature increase of PLA was enhanced by 320% in nanocomposite form through the addition of exfoliated h-BN. The uniformity of heat sinks was also examined, and because the h-BN/PLA heat sink has the lowest range in temperature value, it was found to exhibit even greater uniformity than the commercial Al heat sink.

LED bulb holders were also printed as another application to show the heat dissipation performance of the h-BN/PLA nanocomposites. In this experiment h-BN filled 3D printed LED bulb holder showed slightly better performance than the commercial bulb holder and it showed much better performance than the bare PLA sample. Although the temperature difference between the commercial and 3D printed h-BN/PLA sample was only 1.3 °C, this difference would correspond to an increase in the lifetime of the LED bulb by 5000 hours. 3D printed samples had porous structures, especially in the spaces between the layers, due to the layer-by-layer production method. Despite these conditions, 3D printed sample still performed slightly better than the commercial bulb holder.

5.2 Future Recommendations

In this thesis, h-BN was exfoliated using two methods that have a yield between 10-13 %. The shear exfoliation was preferred due to its higher efficiency. Even though the yield of this method is increased by recycling, more efforts must be spent to increase its efficiency. The exfoliation agent beside IPA can be investigated to increase the polarization efficiency between the h-BN layers and surfactants.

The size distribution of h-BN used for filament production was minimized in this work. However, exfoliated large and small lateral sized h-BN mixture can be investigated to create a more anisotropic thermal path. In addition, it was mentioned

that larger-sized (3-20 µm) h-BN was used for thermal applications in the literature as mentioned in the previous chapters. A larger-sized h-BN exfoliated by the method used in this work, could produce longer thermal paths, thus resulting in higher thermal conductivity.

3D Printing makes use of various parameters to optimize the printed object's features. Alignment of the filler materials is one of the most critical issues for anisotropically increasing the thermal conductivity of the printed objects. Printed objects for this purpose can be tried to print in different directions like vertically to obtain the highest through-plane heat dissipation performance. Furthermore, parameters like print speed, nozzle and bed temperatures can affect both the size and number of pores in the printed objects. As mentioned in the previous chapters, the pores prevent the filler material from transferring its thermal conductivity properties to the nanocomposite, thus creating an important barrier for thermal pathways. Therefore, the thermal properties of the printed objects can be dramatically increased by optimizing these settings. The reached temperature of 3D printed h-BN/PLA heat sink was 53.8 °C which is close to T_g of PLA (around 55 °C). Therefore, 3D printable polymers other than PLA can be investigated as a matrix for applications requiring higher temperatures.

In this work, the h-BN filled composites were produced in a filament shape for FDM printers but they can also be produced as inks for different applications. For example, thermal paste products are especially important for computer integrated circuits and motherboards. h-BN can be used in an ink formulation for these areas of application, for example in an epoxy matrix. This ink can be 3D printed using a Direct Ink Writer (DIW) and desired shapes can be produced by configuring the ink viscosity. These complex shapes can be used for different thermal management applications as well as thermal paste.

REFERENCES

1. Wang, X., Jiang, M., Zhou, Z., Gou, J. & Hui, D. 3D printing of polymer matrix composites: A review and prospective. *Compos. Part B Eng.* 110, 442–458 (2017).

2. Levy, G. N. & Schindel, R. MANUFACTURING (LM) TECHNOLOGIES , STATE OF THE ART AND FUTURE. 2,.

3. Prakash, K. S., Nancharaih, T. & Rao, V. V. S. Additive Manufacturing Techniques in Manufacturing -An Overview. *Mater. Today Proc.* 5, 3873–3882 (2018).

4. Kumar, V. & Dutta, D. An assessment of data formats for layered manufacturing. *Adv. Eng. Softw.* 28, 151–164 (1997).

5. Hu, J. Study on STL-based slicing process for 3D printing. *Solid Free. Fabr. 2017 Proc. 28th Annu. Int. Solid Free. Fabr. Symp. - An Addit. Manuf. Conf. SFF 2017* 885–895 (2020).

6. Baumann, F. W., Schuermann, M., Odefey, U. & Pfeil, M. From GCode to STL: Reconstruct Models from 3D Printing as a Service. *IOP Conf. Ser. Mater. Sci. Eng.* 280, (2017).

7. Pérez, M., Carou, D., Rubio, E. M. & Teti, R. Current advances in additive manufacturing. *Procedia CIRP* 88, 439–444 (2020).

8. Boschetto, A. & Bottini, L. Roughness prediction in coupled operations of fused deposition modeling and barrel finishing. *J. Mater. Process. Technol.* 219, 181–192 (2015).

9. Yamazaki, T. Development of A Hybrid Multi-tasking Machine Tool: Integration of Additive Manufacturing Technology with CNC Machining. *Procedia CIRP* 42, 81–86 (2016).

10. Singh, S., Ramakrishna, S. & Singh, R. Material issues in additive manufacturing: A review. *J. Manuf. Process.* 25, 185–200 (2017).

11. Li, H., Wang, T., Sun, J. & Yu, Z. The effect of process parameters in fused deposition modelling on bonding degree and mechanical properties. *Rapid Prototyp. J.* 24, 80–92 (2018).

12. Kumar, P., Ahuja, I. P. S. & Singh, R. Application of fusion deposition modelling for rapid investment casting - A review. *Int. J. Mater. Eng. Innov.* 3, 204–227 (2012).

13. Mohamed, O. A., Masood, S. H. & Bhowmik, J. L. Optimization of fused deposition modeling process parameters: a review of current research and future prospects. *Adv. Manuf.* 3, 42–53 (2015).

14. Abdulhameed, O., Al-Ahmari, A., Ameen, W. & Mian, S. H. Additive manufacturing: Challenges, trends, and applications. *Adv. Mech. Eng.* 11, 1–27 (2019).

15. Rajan, K., Samykano, M., Kadirgama, K., Harun, W. S. W. & Rahman, M. M. *Fused deposition modeling: process, materials, parameters, properties, and applications. International Journal of Advanced Manufacturing Technology* vol. 120 (Springer London, 2022).

16. Solomon, I. J., Sevvel, P. & Gunasekaran, J. A review on the various processing parameters in FDM. *Mater. Today Proc.* 37, 509–514 (2020).

17. Zhang, Y., Jarosinski, W., Jung, Y. G. & Zhang, J. *Additive manufacturing processes and equipment. Additive Manufacturing: Materials, Processes, Quantifications and Applications* (Elsevier Inc., 2018). doi:10.1016/B978-0-12-812155-9.00002-5.

18. Piedra-Cascón, W., Krishnamurthy, V. R., Att, W. & Revilla-León, M. 3D printing parameters, supporting structures, slicing, and post-processing procedures of vat-polymerization additive manufacturing technologies: A

narrative review. *J. Dent.* 109, (2021).

19. Kimura, M., Nakatani, S., Nishida, S. I., Taketoshi, D. & Araki, N. 3D printable dry eeg electrodes with coiled-spring prongs. *Sensors (Switzerland)* 20, 1–14 (2020).

20. Dizon, J. R. C., Gache, C. C. L., Cascolan, H. M. S., Cancino, L. T. & Advincula, R. C. Post-Processing of 3D-Printed Polymers. (2021).

21. Manapat, J. Z., Chen, Q., Ye, P. & Advincula, R. C. 3D Printing of Polymer Nanocomposites via Stereolithography. *Macromol. Mater. Eng.* 302, 1–13 (2017).

22. Yao, H., Wang, J. & Mi, S. Photo processing for biomedical hydrogels design and functionality: A review. *Polymers (Basel).* 10, 1–27 (2018).

23. Karakurt, I. & Lin, L. 3D printing technologies: techniques, materials, and post-processing. *Curr. Opin. Chem. Eng.* 28, 134–143 (2020).

24. Yang, Y., Song, X., Li, X., Chen, Z., Zhou, C., Zhou, Q. & Chen, Y. Recent Progress in Biomimetic Additive Manufacturing Technology: From Materials to Functional Structures. *Adv. Mater.* 30, (2018).

25. Jasiuk, I., Abueidda, D. W., Kozuch, C., Pang, S., Su, F. Y. & McKittrick, J. An Overview on Additive Manufacturing of Polymers. *Jom* 70, 275–283 (2018).

26. Kim, H., Choi, J. W. & Wicker, R. Scheduling and process planning for multiple material stereolithography. *Rapid Prototyp. J.* 16, 232–240 (2010).

27. Wu, X., Lian, Q., Li, D. & Jin, Z. Tilting separation analysis of bottom-up mask projection stereolithography based on cohesive zone model. *J. Mater. Process. Technol.* 243, 184–196 (2017).

28. Dev Singh, D., Mahender, T. & Raji Reddy, A. Powder bed fusion process: A brief review. *Mater. Today Proc.* 46, 350–355 (2021).

29. Moon, J., Grau, J. E., Knezevic, V., Cima, M. J. & Sachs, E. M. Ink-jet printing of binders for ceramic components. *J. Am. Ceram. Soc.* 85, 755–762 (2002).

30. Utela, B., Storti, D., Anderson, R. & Ganter, M. A review of process development steps for new material systems in three dimensional printing (3DP). *J. Manuf. Process.* 10, 96–104 (2008).

31. Zhai, Y., Lados, D. A. & Lagoy, J. L. Additive Manufacturing: Making imagination the major Limitation. *Jom* 66, 808–816 (2014).

32. Stavropoulos, P. & Foteinopoulos, P. Modelling of additive manufacturing processes: A review and classification. *Manuf. Rev.* 5, (2018).

33. Masutani, K. & Kimura, Y. *PLA Synthesis and Polymerization. Poly(lactic acid) Science and Technology : Processing, Properties, Additives and Applications* (2014).

34. Datta, R. & Henry, M. Lactic acid: Recent advances in products, processes and technologies - A review. *Journal of Chemical Technology and Biotechnology* vol. 81 1119–1129 at https://doi.org/10.1002/jctb.1486 (2006).

35. Pang, X., Zhuang, X., Tang, Z. & Chen, X. Polylactic acid (PLA): Research, development and industrialization. *Biotechnology Journal* vol. 5 1125–1136 at https://doi.org/10.1002/biot.201000135 (2010).

36. de Albuquerque, T. L., Marques Júnior, J. E., de Queiroz, L. P., Ricardo, A. D. S. & Rocha, M. V. P. Polylactic acid production from biotechnological routes: A review. *Int. J. Biol. Macromol.* 186, 933–951 (2021).

37. Hu, Y., Daoud, W. A., Cheuk, K. K. L. & Lin, C. S. K. Newly developed techniques on polycondensation, ring-opening polymerization and polymer modification: Focus on poly(lactic acid). *Materials (Basel).* 9, (2016).

38. Achmad, F., Yamane, K., Quan, S. & Kokugan, T. Synthesis of polylactic acid by direct polycondensation under vacuum without catalysts, solvents and

initiators. *Chem. Eng. J.* 151, 342–350 (2009).

39.   Mehta, R., Kumar, V., Bhunia, H. & Upadhyay, S. N. Synthesis of poly(lactic acid): A review. *J. Macromol. Sci. - Polym. Rev.* 45, 325–349 (2005).

40.   Farah, S., Anderson, D. G. & Langer, R. Physical and mechanical properties of PLA, and their functions in widespread applications — A comprehensive review. *Adv. Drug Deliv. Rev.* 107, 367–392 (2016).

41.   Oksiuta, Z., Jalbrzykowski, M., Mystkowska, J., Romanczuk, E. & Osiecki, T. Mechanical and thermal properties of polylactide (PLA) composites modified with Mg, Fe, and polyethylene (PE) additives. *Polymers (Basel).* 12, 1–14 (2020).

42.   Sin, L. T., Rahmat, A. R. & Rahman, W. A. W. A. *Mechanical Properties of Poly(lactic Acid). Polylactic Acid* (2013). doi:10.1016/b978-1-4377-4459-0.00005-6.

43.   Bachchan, A. A., Das, P. P. & Chaudhary, V. Effect of moisture absorption on the properties of natural fiber reinforced polymer composites: A review. *Mater. Today Proc.* 49, 3403–3408 (2020).

44.   Lay, M., Thajudin, N. L. N., Hamid, Z. A. A., Rusli, A., Abdullah, M. K. & Shuib, R. K. Comparison of physical and mechanical properties of PLA, ABS and nylon 6 fabricated using fused deposition modeling and injection molding. *Compos. Part B Eng.* 176, 107341 (2019).

45.   Lim, L. T., Auras, R. & Rubino, M. Processing technologies for poly(lactic acid). *Prog. Polym. Sci.* 33, 820–852 (2008).

46.   Smith, G. D.; Bedrov, D. Relationship Between the a- and b-Relaxation Processes in Amorphous Polymers: Insight From Atomistic Molecular Dynamics Simulations of 1,4-Polybutadiene Melts and Blends. *J. Polym. Sci. Part B Polym. Phys.* 45, 627–643 (2007).

47.   Mortazavi, B., Hassouna, F., Laachachi, A., Rajabpour, A., Ahzi, S., Chapron,

D., Toniazzo, V. & Ruch, D. Experimental and multiscale modeling of thermal conductivity and elastic properties of PLA/expanded graphite polymer nanocomposites. *Thermochim. Acta* 552, 106–113 (2013).

48. Huang, J., Zhu, Y., Xu, L., Chen, J., Jiang, W. & Nie, X. Massive enhancement in the thermal conductivity of polymer composites by trapping graphene at the interface of a polymer blend. *Compos. Sci. Technol.* 129, 160–165 (2016).

49. Takagi, H., Kako, S., Kusano, K. & Ousaka, A. Thermal conductivity of PLA-bamboo fiber composites. *Adv. Compos. Mater. Off. J. Japan Soc. Compos. Mater.* 16, 377–384 (2007).

50. Han, Z. & Fina, A. Thermal conductivity of carbon nanotubes and their polymer nanocomposites: A review. *Prog. Polym. Sci.* 36, 914–944 (2011).

51. Lee, G. H., Cooper, R. C., An, S. J., Lee, S., Van Der Zande, A., Petrone, N., Hammerberg, A. G., Lee, C., Crawford, B., Oliver, W., Kysar, J. W. & Hone, J. High-strength chemical-vapor-deposited graphene and grain boundaries. *Science (80-.).* 340, 1074–1076 (2013).

52. Kim, M., Jeong, J. H., Lee, J. Y., Capasso, A., Bonaccorso, F., Kang, S. H., Lee, Y. K. & Lee, G. H. Electrically Conducting and Mechanically Strong Graphene-Polylactic Acid Composites for 3D Printing. *ACS Appl. Mater. Interfaces* 11, 11841–11848 (2019).

53. Ivanov, E., Kotsilkova, R., Xia, H., Chen, Y., Donato, R. K., Donato, K., Godoy, A. P., Di Maio, R., Silvestre, C., Cimmino, S. & Angelov, V. PLA/Graphene/MWCNT composites with improved electrical and thermal properties suitable for FDM 3D printing applications. *Appl. Sci.* 9, (2019).

54. Pakdel, A., Bando, Y. & Golberg, D. Nano boron nitride flatland. *Chem. Soc. Rev.* 43, 934–959 (2014).

55. Hazzan, K. E., Pacella, M. & See, T. L. Laser processing of hard and ultra-

hard materials for micro-machining and surface engineering applications. *Micromachines* 12, (2021).

56. Bhimanapati, G. R., Lin, Z., Meunier, V., Jung, Y., Cha, J., Das, S., Xiao, D., Son, Y., Strano, M. S., Cooper, V. R., Liang, L., Louie, S. G., Ringe, E., Zhou, W., Kim, S. S., Naik, R. R., Sumpter, B. G., Terrones, H., Xia, F., Wang, Y., Zhu, J., Akinwande, D., Alem, N., Schuller, J. A., Schaak, R. E., Terrones, M. & Robinson, J. A. Recent Advances in Two-Dimensional Materials beyond Graphene. *ACS Nano* 9, 11509–11539 (2015).

57. Bhimanapati, G. R., Glavin, N. R. & Robinson, J. A. *2D Boron Nitride: Synthesis and Applications*. *Semiconductors and Semimetals* vol. 95 (Elsevier Inc., 2016).

58. Jiang, X. F., Weng, Q., Wang, X. Bin, Li, X., Zhang, J., Golberg, D. & Bando, Y. Recent Progress on Fabrications and Applications of Boron Nitride Nanomaterials: A Review. *J. Mater. Sci. Technol.* 31, 589–598 (2015).

59. Liu, Z., Gong, Y., Zhou, W., Ma, L., Yu, J., Idrobo, J. C., Jung, J., Macdonald, A. H., Vajtai, R., Lou, J. & Ajayan, P. M. Ultrathin higherature oxidation-resistant coatings of hexagonal boron nitride. *Nat. Commun.* 4, 1–8 (2013).

60. Kimura, Y., Wakabayashi, T., Okada, K., Wada, T. & Nishikawa, H. Boron nitride as a lubricant additive. *Wear* 232, 199–206 (1999).

61. Shahrzadi, M., Davazdah Emami, M. & Akbarzadeh, A. H. Heat transfer in BCC lattice materials: Conduction, convection, and radiation. *Compos. Struct.* 284, 115159 (2022).

62. Wang, Q., Liu, B. & Wang, Z. Investigation of heat transfer mechanisms among particles in horizontal rotary retorts. *Powder Technol.* 367, 82–96 (2020).

63. Fang, H., Bai, S. L. & Wong, C. P. "White graphene" – hexagonal boron nitride based polymeric composites and their application in thermal

management. *Compos. Commun.* 2, 19–24 (2016).

64.   Belaid, H., Nagarajan, S., Barou, C., Huon, V., Bares, J., Balme, S., Miele, P., Cornu, D., Cavaillès, V., Teyssier, C. & Bechelany, M. Boron Nitride Based Nanobiocomposites: Design by 3D Printing for Bone Tissue Engineering. *ACS Appl. Bio Mater.* 3, 1865–1874 (2020).

65.   Giri, A., Hopkins, P. E., Wessel, J. G. & Duda, J. C. Kapitza resistance and the thermal conductivity of amorphous superlattices. *J. Appl. Phys.* 118, (2015).

66.   Burger, N., Laachachi, A., Ferriol, M., Lutz, M., Toniazzo, V. & Ruch, D. Review of thermal conductivity in composites: Mechanisms, parameters and theory. *Prog. Polym. Sci.* 61, 1–28 (2016).

67.   Lindsay, L. & Broido, D. A. Enhanced thermal conductivity and isotope effect in single-layer hexagonal boron nitride. *Phys. Rev. B - Condens. Matter Mater. Phys.* 84, 1–6 (2011).

68.   Lindsay, L. & Broido, D. A. Theory of thermal transport in multilayer hexagonal boron nitride and nanotubes. *Phys. Rev. B - Condens. Matter Mater. Phys.* 85, 1–8 (2012).

69.   Wang, Z. L., Mu, H. T., Liang, J. G. & Tang, D. W. Thermal boundary resistance and temperature dependent phonon conduction in CNT array multilayer structure. *Int. J. Therm. Sci.* 74, 53–62 (2013).

70.   Pan, C., Zhang, J., Kou, K., Zhang, Y. & Wu, G. Investigation of the through-plane thermal conductivity of polymer composites with in-plane oriented hexagonal boron nitride. *Int. J. Heat Mass Transf.* 120, 1–8 (2018).

71.   Luo, F., Yang, S., Yan, P., Li, H., Huang, B., Qian, Q. & Chen, Q. Orientation behavior and thermal conductivity of liquid crystal polymer composites based on Three-Dimensional printing. *Compos. Part A Appl. Sci. Manuf.* 160, 107059 (2022).

72. Guo, H., Niu, H., Zhao, H., Kang, L., Ren, Y., Lv, R., Ren, L., Maqbool, M., Bashir, A. & Bai, S. Highly Anisotropic Thermal Conductivity of Three-Dimensional Printed Boron Nitride-Filled Thermoplastic Polyurethane Composites: Effects of Size, Orientation, Viscosity, and Voids. *ACS Appl. Mater. Interfaces* 14, 14568–14578 (2022).

73. Bennett, S. Development of the PID Controller. *IEEE Control Syst.* 13, 58–62 (1993).

74. Ranjan, S., Sharma, A. & Chaudhary, P. An effective temperature controller system using PID mechanism. *Proc. Int. Conf. Innov. Appl. Comput. Intell. Power, Energy Control. with Their Impact Humanit. CIPECH 2014* 182–185 (2014) doi:10.1109/CIPECH.2014.7019086.

75. Lei, W., Mochalin, V. N., Liu, D., Qin, S., Gogotsi, Y. & Chen, Y. Boron nitride colloidal solutions, ultralight aerogels and freestanding membranes through one-step exfoliation and functionalization. *Nat. Commun.* 6, 1–8 (2015).

76. Wang, N., Yang, G., Wang, H., Yan, C., Sun, R. & Wong, C. P. A universal method for large-yield and high-concentration exfoliation of two-dimensional hexagonal boron nitride nanosheets. *Mater. Today* 27, 33–42 (2019).

77. Zhu, H., Li, Y., Fang, Z., Xu, J., Cao, F., Wan, J. & Preston, C. High Thermally Conductive Papers with Percolative Layered Boron Nitride. *ACS Nano* 3606–3613 (2014).

78. Kargar, F., Barani, Z., Salgado, R., Debnath, B., Lewis, J. S., Aytan, E., Lake, R. K. & Balandin, A. A. Thermal Percolation Threshold and Thermal Properties of Composites with High Loading of Graphene and Boron Nitride Fillers. *ACS Appl. Mater. Interfaces* 10, 37555–37565 (2018).

79. Li, J., Shi, Q., Shao, Y., Hou, C., Li, Y., Zhang, Q. & Wang, H. Cladding nanostructured AgNWs-MoS2 electrode material for high-rate and long-life transparent in-plane micro-supercapacitor. *Energy Storage Mater.* 16, 212–

219 (2019).

80.   Yang, D. & Frindt, R. F. Li-intercalation and exfoliation of WS2. *J. Phys. Chem. Solids* 57, 1113–1116 (1996).

81.   Cano-Márquez, A. G., Rodríguez-Macías, F. J., Campos-Delgado, J., Espinosa-González, C. G., Tristán-López, F., Ramírez-González, D., Cullen, D. A., Smith, D. J., Terrones, M. & Vega-Cantú, Y. I. Ex-MWNTs: Graphene sheets and ribbons produced by lithium intercalation and exfoliation of carbon nanotubes. *Nano Lett.* 9, 1527–1533 (2009).

82.   Yang, R., Mei, L., Zhang, Q., Fan, Y., Shin, H. S., Voiry, D. & Zeng, Z. High-yield production of mono- or few-layer transition metal dichalcogenide nanosheets by an electrochemical lithium ion intercalation-based exfoliation method. *Nat. Protoc.* 17, 358–377 (2022).

83.   Yang, Y., Hou, H., Zou, G., Shi, W., Shuai, H., Li, J. & Ji, X. Electrochemical exfoliation of graphene-like two-dimensional nanomaterials. *Nanoscale* 11, 16–33 (2019).

84.   Gonzalez Ortiz, D., Pochat-Bohatier, C., Cambedouzou, J., Bechelany, M. & Miele, P. Exfoliation of hexagonal boron nitride (h-BN) in liquide phase by ion intercalation. *Nanomaterials* 8, 1–12 (2018).

85.   Ambrosi, A. & Pumera, M. Electrochemically Exfoliated Graphene and Graphene Oxide for Energy Storage and Electrochemistry Applications. *Chem. - A Eur. J.* 22, 153–159 (2016).

86.   Mayorga-Martinez, C. C., Khezri, B., Eng, A. Y. S., Sofer, Z., Ulbrich, P. & Pumera, M. Bipolar Electrochemical Synthesis of WS2 Nanoparticles and Their Application in Magneto-Immunosandwich Assay. *Adv. Funct. Mater.* 26, 4094–4098 (2016).

87.   Fosdick, S. E., Knust, K. N., Scida, K. & Crooks, R. M. Bipolar electrochemistry. *Angew. Chemie - Int. Ed.* 52, 10438–10456 (2013).

88. Wang, Y., Mayorga-Martinez, C. C., Chia, X., Sofer, Z. & Pumera, M. Nonconductive layered hexagonal boron nitride exfoliation by bipolar electrochemistry. *Nanoscale* 10, 7298–7303 (2018).

89. Yang, J., Du, K., Hu, L. & Wang, D. Scalable Fabrication of Carbon Nanomaterials by Electrochemical Dual-Electrode Exfoliation of Graphite in Hydroxide Molten Salt. *Ind. Eng. Chem. Res.* 59, 10010–10017 (2020).

90. Liang, X., Guo, J., Liang, S., Hong, C. & Zhao, Y. Synthesis of soluble graphene nanosheets from graphite fluoride in low-temperature molten hydroxides. *Mater. Lett.* 135, 92–95 (2014).

91. Golberg, D., Bando, Y., Huang, Y., Terao, T., Mitome, M., Tang, C. & Zhi, C. Boron nitride nanotubes and nanosheets. *ACS Nano* 4, 2979–2993 (2010).

92. Li, X., Hao, X., Zhao, M., Wu, Y., Yang, J., Tian, Y. & Qian, G. Exfoliation of hexagonal boron nitride by molten hydroxides. *Adv. Mater.* 25, 2200–2204 (2013).

93. Deepika, A., Li, L. H., Glushenkov, A. M., Hait, S. K., Hodgson, P. & Chen, Y. High-efficient production of boron nitride nanosheets via an optimized ball milling process for lubrication in oil. *Sci. Rep.* 4, 2–7 (2014).

94. Lee, D. & Song, S. H. Ultra-thin ultraviolet cathodoluminescent device based on exfoliated hexagonal boron nitride. *RSC Adv.* 7, 7831–7835 (2017).

95. Liu, P., Ding, J., Su, S. & Yu, H. A universal strategy for high-yield producing water compatible boron nitride nanosheets. *New J. Chem.* 44, 19812–19819 (2020).

96. Gorbachev, R. V., Riaz, I., Nair, R. R., Jalil, R., Britnell, L., Belle, B. D., Hill, E. W., Novoselov, K. S., Watanabe, K., Taniguchi, T., Geim, A. K. & Blake, P. Hunting for monolayer boron nitride: Optical and raman signatures. *Small* 7, 465–468 (2011).

97. Joni, I. M., Balgis, R., Ogi, T., Iwaki, T. & Okuyama, K. Surface

functionalization for dispersing and stabilizing hexagonal boron nitride nanoparticle by bead milling. *Colloids Surfaces A Physicochem. Eng. Asp.* 388, 49–58 (2011).

98. Kim, N. Y., Jeong, H. Y., Kim, J. H., Kim, G., Shin, H. S. & Lee, Z. Evidence of Local Commensurate State with Lattice Match of Graphene on Hexagonal Boron Nitride. *ACS Nano* 11, 7084–7090 (2017).

99. Saha, S., Rice, A., Ghosh, A., Hasan, S. M. N., You, W., Ma, T., Hunter, A., Bissell, L. J., Bedford, R., Crawford, M. & Arafin, S. Comprehensive characterization and analysis of hexagonal boron nitride on sapphire. *AIP Adv.* 11, (2021).

100. Sahu, J., Panda, K., Gupta, B., Kumar, N., Manojkumar, P. A. & Kamruddin, M. Enhanced tribo-chemical properties of oxygen functionalized mechanically exfoliated hexagonal boron nitride nanolubricant additives. *Mater. Chem. Phys.* 207, 412–422 (2018).

101. Li, L. H., Santos, E. J. G., Xing, T., Cappelluti, E., Roldán, R., Chen, Y., Watanabe, K. & Taniguchi, T. Dielectric screening in atomically thin boron nitride nanosheets. *Nano Lett.* 15, 218–223 (2015).

102. Raza, A., Hassan, J. Z., Ikram, M., Ali, S., Farooq, U., Khan, Q. & Maqbool, M. Advances in Liquid-Phase and Intercalation Exfoliations of Transition Metal Dichalcogenides to Produce 2D Framework. *Adv. Mater. Interfaces* 8, (2021).

103. Gautam, C. & Chelliah, S. Methods of hexagonal boron nitride exfoliation and its functionalization: Covalent and non-covalent approaches. *RSC Adv.* 11, 31284–31327 (2021).

104. Bayraktar, I., Doganay, D., Coskun, S., Kaynak, C., Akca, G. & Unalan, H. E. 3D printed antibacterial silver nanowire/polylactide nanocomposites. *Compos. Part B Eng.* 172, 671–678 (2019).

105. Xu, X., Chen, J., Zhou, J. & Li, B. Thermal Conductivity of Polymers and Their Nanocomposites. *Adv. Mater.* 30, 1–10 (2018).

106. Moore, A. L. & Shi, L. Emerging challenges and materials for thermal management of electronics. *Mater. Today* 17, 163–174 (2014).

107. Shtein, M., Nadiv, R., Buzaglo, M. & Regev, O. Graphene-Based Hybrid Composites for Efficient Thermal Management of Electronic Devices. *ACS Appl. Mater. Interfaces* 7, 23725–23730 (2015).

108. Smith, M., Kim, S., Lambert, A., Walde, M., Lindahl, J., Mungale, K., Bougher, T., Hassen, A. A. & Kunc, V. Maximizing the performance of a 3D printed heat sink by accounting for anisotropic thermal conductivity during filament deposition. *Intersoc. Conf. Therm. Thermomechanical Phenom. Electron. Syst. ITHERM* 2019-May, 626–632 (2019).

109. Pimputkar, S., Speck, J. S., Denbaars, S. P. & Nakamura, S. Prospects for LED lighting. *Nat. Photonics* 3, 180–182 (2009).

110. Wang, R. T. & Wang, J. C. Analyzing the structural designs and thermal performance of nonmetal lighting devices of LED bulbs. *Int. J. Heat Mass Transf.* 99, 750–761 (2016).

111. Wu, S. J., Hsu, H. C., Fu, S. L. & Yeh, J. N. Numerical simulation of high power LED heat-dissipating system. *Electron. Mater. Lett.* 10, 497–502 (2014).

112. Hsieh, C. C. & Li, Y. H. The study for saving energy and optimization of led street light heat sink design. *Adv. Mater. Sci. Eng.* 2015, (2015).

113. Barbosa, J. L. F., Simon, D. & Calixto, W. P. Design optimization of a high power LED matrix luminaire. *Energies* 10, 1–18 (2017).

114. Jia, Y., He, H., Geng, Y., Huang, B. & Peng, X. High through-plane thermal conductivity of polymer based product with vertical alignment of graphite flakes achieved via 3D printing. *Compos. Sci. Technol.* 145, 55–61 (2017).